A STUDY OF THE DEVELOPMENT OF AN ANALYTICAL WALL FUNCTION FOR LARGE EDDY SIMULATION OF TURBULENT CHANNEL AND RECTANGULAR DUCT FLOW

by

Takahiko Hasegawa

A Thesis Submitted in

Partial Fulfillment of the

Requirements for the Degree of

Master of Science

in Engineering

at

The University of Wisconsin-Milwaukee

August 2014

ABSTRACT

A STUDY OF THE DEVELOPMENT OF AN ANALYTICAL WALL FUNCTION FOR LARGE EDDY SIMULATION OF TURBULENT CHANNEL AND RECTANGULAR DUCT FLOW

by

Takahiko Hasegawa

The University of Wisconsin-Milwaukee, 2014
Under the Supervision of Professor Ryo S. Amano

This paper reports computational work of three-dimensional channel turbulent flow and rectangular duct flow with the Analytical Wall Function (AWF). The main purpose of this study is to establish and validate the new modeling of AWF for Large Eddy Simulation (LES-AWF). In order to compare the performance of the new modeling of LES-AWF, the conventional LES-AWF and Wall-resolved LES are applied. The new LES-AWF showed improvements of flow prediction in both of three-dimensional channel flow and rectangular duct flow, although the improvement in rectangular duct is relatively minor.

TABLE OF CONTENTS

LIST OF FIGURES

LIST OF TABLES

LIST OF SYMBOLS

Symbols : Discretion

a_1, a_2 : model coefficients for α and y_v^+ function LES-AWF

A_i : convection term

$A_U, B_U, A_U{}', B_U{}'$: integration constants for AWF model

B_i : diffusion term

$B_{x,i}^-, B_{x,i}^+, B_{y,j}^-, B_{y,j}^+$: coefficients for pressure equation

$B_{i,j}^0$: $= B_{x,i}^- + B_{x,i}^+ + B_{y,j}^- + B_{y,j}^+$

B : model constant for log law $B = 5.5$

C_U : right hand side of boundary layer equation for AWF model

C_v, C_S : model coefficients

c_μ, c_l : model coefficients

D : force imposed on the wall

$G(x)$: filtering function

H : channel height, duct height or duct width

k_{GS}, k_{SGS} : GS turbulence kinetic energy, SGS turbulence kinetic energy

n, m : the number of time step

u_i, u_i^P, u_τ : velocity, predicted velocity, friction velocity

$\overline{u_i' u_j'}$: Reynolds stress

x_i : physical coordinate system

p : pressure

P : $= p/\rho$

q_1, q_2, q_3 : mass flow rates

Q_1, Q_2, Q_3 : momentums

Re_τ : friction Reynolds number $\mathrm{Re}_\tau = u_\tau H/\nu$

$R_{ij}^{'}$: the extra anisotropic term for SGS eddy viscosity ν_{SGS}

S_{ij} : strain rate tensor

S_φ : production term

$\overline{|S|}^+$: normalized strain rate tensor $\overline{|S|}^+ = \overline{|S|}\Delta/\nu$

$u_{rms}^{'}, v_{rms}^{'}, w_{rms}^{'}$: root mean square of Reynolds stresses

y_v, y_n : thickness of viscous sub layer, wall adjacent cell height

y^+, y_v^+, y_1^+ : normalized wall distances $y^+ = u_\tau y/\nu$, $y_v^+ = u_\tau y_v/\nu$, $y_1^+ = u_\tau y_1/\nu$

y_1, y_p : wall distance of first grid point

Y^+ : $= 1 + \alpha(y^* - {y_v}^+)$

$\langle \quad \rangle$: GS components, filtering operator

$\tilde{}$: SGS components

Greek Letters

α	:	slope of the modeled ν_{SGS} in near wall region for AWF model
β	:	over relaxation coefficient, model coefficient for AWF model
γ	:	model coefficient for AWF model
δ_{ij}	:	Kronecker's delta
δ	:	half duct height or half duct width
$\varepsilon^{'}, \varepsilon$	:	residual for SOR method
$\varepsilon_{GS}, \varepsilon_{SGS}$	:	SGS dissipation term, GS dissipation term
Γ	:	coefficient of diffusion term
κ	:	von Karman constant $\kappa = 0.4$
ξ, η, ζ	:	wall coordinate system directions
Δt	:	time step size
ϑ	:	the rotation degree from physical coordinate system to wall coordinate system
Δ	:	filter width $\Delta = \sqrt[3]{\Delta x \Delta y \Delta z}$
$\Delta x, \Delta y, \Delta z$	:	grid sizes
$\Delta x^+, \Delta y^+, \Delta z^+$	:	normalized grid sizes $\Delta x^+ = u_\tau \Delta x/\nu$, $\Delta y^+ = u_\tau \Delta y/\nu$, $\Delta z^+ = u_\tau \Delta z/\nu$
τ_{ij}, τ_{ij}^a	:	SGS stress, anisotropic part of SGS stress
τ_w	:	wall shear stress
μ	:	molecular viscosity
ν, ν_t, ν_{SGS}	:	kinematic viscosity, eddy viscosity, SGS eddy viscosity
ρ	:	density
φ	:	general value, scalar potential
$\psi_{i,j}$	:	right hand side of Poisson's equation

LIST OF ABBREVIATIONS

AWF : Analytical Wall Function

CFD : Computational Fluid Dynamics

CFL : Courant-Friedrichs-Lewy

DNS : Direct Numerical Simulation

FDM : Finite Difference Method

GS : Grid Scale

LES : Large Eddy Simulation

LES-AWF : LES for AWF

LRN : Low-Reynolds-number

RANS : Reynolds Averaged Navier-Stokes simulation

RANS-AWF : AWF for RANS

SGS : Sub-Grid Scale

SMAC : Simplified Marker And Cell

SWF : Standard Wall Function

CHAPTER 1: INTRODUCTION

1.1 Near Wall Treatment:

Turbulent flow is one of the most familiar phenomena which you can encounter in day-to-day life. Hence, many industrial products which are indispensable for our lives are designed by considering the effects of turbulent flow. Cars with improved cross wind stability and reduced aerodynamic drag, aircrafts whose blades have enhanced fuel efficiency and wind turbines which make reduced noise are all typical examples. It is required to run simulations to predict heat and mass transfer of the fluid by utilizing Computational Fluid Dynamics (CFD) and the accurate numerical analysis for turbulence is helpful for designing industrial products.

In all regions of the flow field, a near wall region is especially the most difficult but essential part to obtain the accurate flow parameters from a numerical analysis. Since CFD for industrial applications has to deal with considerably complex geometries of the flow field made by the complex surfaces, near wall treatment becomes harder. It is necessary to employ different specific methods for the near wall treatment because there are significant fluctuations of physical values such as velocity or turbulence variables that are responsible to generate a low Reynolds number effect. There are two different representative methods for near wall treatment; a Low-Reynolds-number (LRN) model and the use of Wall Functions.

LRN model is a turbulence model which is possible to capture the near wall turbulence precisely and makes the high accuracy of this model reliable. However, in order to adopt this model for CFD, an extremely fine computational mesh has to be

employed even in viscous sub-layer, which is very thin layer adjacent to the wall. Therefore, very fine computational mesh causes an extremely expensive computational cost, resulting in the huge computational time. This is why LRN model is not widely used for CFD simulations in industrial applications even though this model has good accuracy.

The other method for near wall treatment is the use of Wall Functions. The standard wall function, which was invented in 1970s [2-5], has been used in industrial applications and it is still the common method instead of the LRN model, although the latter is an accurate turbulence model. This is because the standard wall function requires a much lower computational cost than LRN model, which contributes to the benefits for industrial applications by saving computational time. The standard wall function can be derived by assuming that Log-Law of the wall is applicable in fully developed turbulence boundary layer and simplifies the analysis in near wall region. Hence, the standard wall function is able to reduce the computational cost and does not require extremely fine mesh for LRN models any longer. However, since the standard wall function is applicable only in simple flow fields and based on the log-law of the wall, which cannot be available in complicated flow field such as separation and reattachment flow, it is hard to predict the turbulence correctly in complicated flow field with the standard wall functions. Hence, there is still a serious issue about the deficient accuracy with this wall function in order to apply to the complex turbulence field.

In order to solve this problem, new wall functions have been studied and reported so that they will replace the conventional standard wall function. One of these new wall functions is an Analytical Wall Function (AWF), which was invented by Craft et al. [1]. The AWF defines the boundary condition by means of the analytical integration of the

momentum and energy equation in wall adjacent cells. The AWF has been improved and extended so that it can be applicable in complex turbulent flow field. For instance, Suga et al.[6-10] has extended the AWF model to rough walls by modifying the AWF [6] to a high Prandtl number turbulent field [7], and devised the model for a permeable wall turbulence such as the turbulence around the porous media [8], high Schmidt number turbulence around gas-liquid interface [9], flow separation, reattachment flow, and an impinging jet flow [10]. As seen in these examples, the AWF makes it possible to predict the turbulence correctly even in complicated flow field where it is hard to be analyzed accurately by the standard wall function, and its computational cost is as low as the standard wall function. Therefore, it can be said that AWF has a great advantage over the standard wall function in this point.

The above mentioned improvements or extensions of the AWF have been studied by Suga et al. [6-10] for the Reynolds Averaged Navier-Stokes simulation (RANS). Even though the RANS is done with the AWF, the accuracy of this method is inadequate for many industrial applications, which means that it is necessary to invent a more accurate new method for the AWF. Since the capability of the high-performance computing clusters has recently been dramatically advanced, Large Eddy Simulation (LES), which is more accurate turbulence simulation method than RANS, although its computational cost is from 10 to 100 times higher than that of RANS, attracted more and more attentions. Hence, many researches have been conducting to create new wall functions for LES; thus, new wall functions can potentially reduce the high computational cost required for a LES computation, which has been a major problem with LES. Some studies were also done to apply the AWF to LES[11]. If the AWF will be improved and extended more in

the future, it will provide great benefits to the CFD in industrial applications. It can be expected that the AWF can be a new simulation method with a high accuracy and low computational cost in industrial application, which contributes to effectively designing industrial products with an advanced performance.

1.2 RANS-AWF:

As mentioned in the previous section, the AWF was originally designed for RANS and it has already been shown that it is applicable to RANS and possible to obtain the more accurate results than standard wall function (SWF) especially in complex flow geometries [7-11]. Arakawa et al. [12] reported the RANS-AWF performance in the 180 degree bend square duct and one of its results is shown in Fig. 1.1. Fig. 1.1 shows the large difference between the AWF and the SWF. It is obvious that the AWF showed better agreement especially around bend section than standard wall function. The boundary layer equation, from which AWF derives the boundary condition on the wall, includes the pressure gradient term, time transient term, convection term and diffusion term, while the SWF includes the pressure gradient term only. In complex geometries, these terms become more predominant because of the geometry effects caused by the complex surfaces. Hence, the AWF is sensible from an adverse pressure gradient and separation and reattachment turbulence flow, which makes the AWF becomes a more advanced and encouraging wall function comparing with the SWF.

RANS-AWF has been extended to complex geometries and improved by the modification of the modeling. Suga et al. [10] changed the way of eddy viscosity profile

modeling, which has a great influence on the accurate prediction for near wall turbulence. They also modified the wall normal components of velocity gradient and introduced a correction term. In addition, the laminarization effect was proposed by Gerasimov [13].

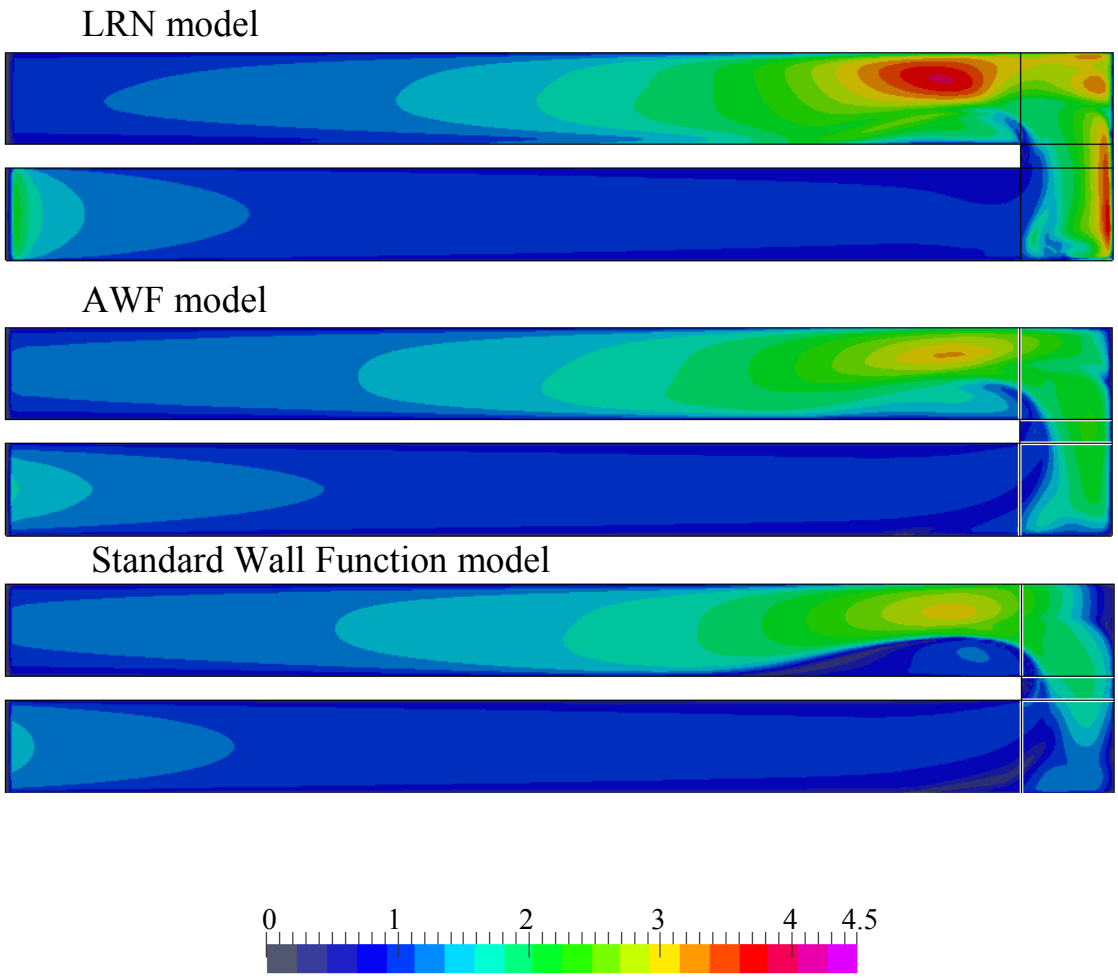

Show flow direction in the fig.

Figure 1.1: AWF performance (Normalized Nusselt number distribution comparison between AWF model and standard wall function model on the bottom wall).

As mentioned above, many studies [6-13] have been done for the improvement and extension of RANS-AWF so far and they proved that AWF is applicable in complex geometries.

1.3 Wall Functions for LES:

Some new wall functions were also proposed for LES[14-28]. Some are based on power-law [14,15] and others are originated from momentum equations[24,28]. Since LES needs an unsteady state simulation, the parameters employed by these wall functions should be instantaneous so that the modeling of these wall functions can be adjusted to a different turbulence field in every iteration. For example, friction velocity, wall shear stress or velocity gradient on the wall are modeled as instantaneous parameters. Deardorff [29] adopted off-wall grid and defined the velocity gradient at the first off-wall grid point by using a filtered velocity and the distance from the wall. Schumann [30] made the instantaneous wall shear stress by assuming that there is a correlation between the wall shear stress and the instantaneous velocity in core region. Piomelli [31] improved Schumann's model [30] by referring to the instantaneous velocity in the downstream from the point where the wall shear stress is required. Balaras and Benocci [32,33] proposed a zonal approach which employs two different meshes: the outer mesh and the inner mesh. The inner mesh is refined in the wall normal direction only and embedded in the first layer of outer mesh, which enables LES to use a coarser outer mesh. The filtered Navier-Stokes equations are solved in the outer mesh, while the simplified set of equations are solved in the inner mesh. In this way, they reduced computational cost and avoid deteriorating the accuracy. Balaras et al. [32,33] adopted an algebraic eddy viscosity model so that parameters strongly related to the characteristic of turbulence can be approximated by using the distance from the wall.

However, there is still a concern with these new wall functions. Most of them are based on log-law of the wall from which standard wall function is derived. In addition, some of them utilize boundary layer equation, which is simplified momentum equation applicable in wall adjacent cells, but they assume that most of the terms such as convection term and unsteady term are negligible.

From this point of view, AWF for LES (LES-AWF) can be a promising method which can replace these wall functions for LES. This is because LES-AWF is based on the boundary layer theory instead of log-law of the wall and most of the terms in boundary layer equation are remained and solved.

1.4 Conventional LES-AWF and problems:

Suga and Kiriishi [34] applied the AWF to LES and validated its accuracy in square duct flow. In their study the same constant parameters as those employed in the RANS-AWF were used for the modeling of sub-grid scale (SGS) [35] eddy viscosity in the wall adjacent cells, even though these constant values are originally defined as parameters for RANS simulation not for LES. The original RANS-AWF refers to the idea of one-equation model of RANS simulation to approximate the eddy viscosity profile. Hence, it is not clear if it is possible to employ the same constant values for the LES instead of the RANS.

In addition, the SGS eddy viscosity for LES is different from eddy viscosity for RANS. While the Eddy viscosity for RANS has not remarkably been affected by a grid resolution, the SGS eddy viscosity significantly depends on the grid resolution.

Therefore, it is not desirable to apply the same constant values to all different computational grids in various geometries.

Hence, making summary of these problems, there are two problems which should be verified about the modeling of SGS eddy viscosity.

1. Instantaneous parameters for the modeling of the SGS eddy viscosity should be employed so that the LES-AWF can be a dynamic wall function which changes depending on the turbulence field on each iteration
2. The parameters for the modeling of the SGS eddy viscosity should take the grid dependency into consideration and be changed by the grid resolution

1.5 Objectives of this study:

As summarized in the previous section, there are two problems with the conventional LES-AWF. The objectives of this study are to solve these problems and to evaluate the performance of the LES-AWF computations.

1. Proposing a new dynamic LES-AWF which changes at every time step depending on the turbulence velocity profile
2. Proposing a new SGS eddy viscosity modeling which is adjustable to the grid resolution in near wall regions

These two improvements have not been done before, which makes this study unique and meaningful. In this study, two different simple geometries, which are three-dimensional channel and three-dimensional square duct, are adopted as computational

geometries. This is because this is the first test for making a new dynamic and instantaneous LES-AWF and that should start with the validation in simple geometries.

CHAPTER 2: COMPUTATIONAL WORK

2.1 **Computational Procedure:**

The CFD code employed in this study is developed by Kajishima [36]. This CFD code is a finite difference solver of three-dimensional incompressible filtered Navier-Stokes equations.

In this study, it is assumed that the fluid is Newtonian fluid and material properties of the fluid are constant.

2.2 **Governing equations:**

In this computational work, the equations which should be solved are the steady state three-dimensional continuity equation for incompressible fluid and the Navier-Stokes equation. These equations are expressed as the following;

Continuity Equation

$$\frac{\partial u_i}{\partial x_i} = 0 \tag{2.1}$$

Navier-Stokes Equation

$$\rho \frac{Du_i}{Dt} = -\frac{\partial p}{\partial x_i} + \frac{\partial}{\partial x_j}\left(\mu \frac{\partial u_i}{\partial x_j}\right) \tag{2.2}$$

where, subscripts i and j denote Cartesian coordinate system and follow Einstein summation convention.

2.3 **Finite Difference Method (FDM):**

The discretization method employed in this study is Finite Difference Method, which treats the governing equations expressed in derivative forms and get solutions on grid points. The derivative terms included in the governing equations such as velocity gradients or pressure gradients are approximated as difference quotients. Space derivative terms can be converted to difference quotients by using the values on grid points, while time derivative terms by using the values at every time step. The derivative terms at east surface and west surface of the control volume of the grid point i, $\left(\frac{\partial \varphi}{\partial x}\right)_e$ and $\left(\frac{\partial \varphi}{\partial x}\right)_w$, are approximated by difference quotients and written as this;

$$\left(\frac{\partial \varphi}{\partial x}\right)_e = \frac{\varphi_{i+1} - \varphi_i}{\Delta x}, \qquad \left(\frac{\partial \varphi}{\partial x}\right)_w = \frac{\varphi_i - \varphi_{i-1}}{\Delta x} \tag{2.3}$$

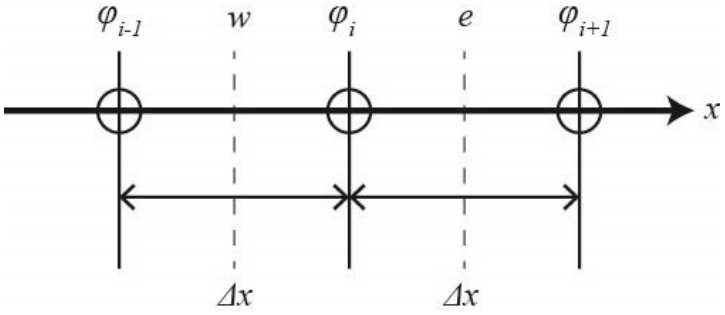

Figure 2.1: Finite Difference Method (FDM).

2.4 **Staggered Grid:**

It is not necessary to place all physical values on the same grid points. It is possible to arrange different meshes for each physical value. If there are no benefits from using different meshes, it is not desirable because program codes will become confusing and less concise. However, arranging different meshes for velocities provides a great

benefit. That avoids “Pressure Checkerboard Problem” [37] , which is a serious problem about the continuity equation and causes numerical instability. That problem is mentioned in detail in section 2.8.

The shifted mesh for velocities, which is called “Staggered Grid”, has been applied by Harlow and Welch [38] for the first time. In staggered grid, the velocity u, the velocity component in x-direction, is solved on the surface normal to the x-direction, because velocity components are solved on the surfaces of control volumes. The locations of the velocity components u are illustrated as allows, while the original grid points circles in *Fig.* 2.2. Dashed lines show surfaces of control volumes. As it can be seen in *Fig.* 2.2, the placement of u is shifted from the original grid points in x-direction. In other words, the placement of u is located on the line connecting two adjacent original grid points.

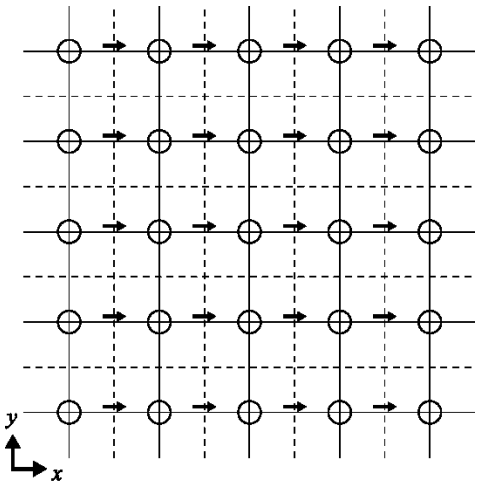

Figure 2.2: Shifted placement for u velocity ($\rightarrow = u$).

The placement of the other velocity components v and w complies with the same rule as the velocity component u. Fig. 2.3 illustrates the two-dimensional staggered grid

arrangement. u and v are both placed on the surfaces of control volumes. Three-dimensional staggered grid arrangement can be described in the same way as two-dimensional staggered grid.

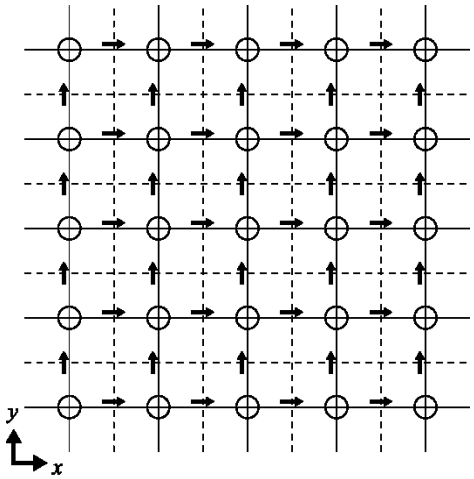

Figure 2.3: Staggered grid (two-dimensional) ($\rightarrow = u,\ \uparrow = v$).

2.5 **Time marching method:**

From Eqs.(2.1) and (2.2), the conservations of mass and momentum are written as this respectively;

Continuity equation (Mass conservation)

$$\frac{\partial u_i}{\partial x_i} = 0 \tag{2.4}$$

Navier-Stokes equation (Momentum conservation)

$$\rho \frac{Du_i}{Dt} = -\frac{\partial p}{\partial x_i} + \frac{\partial}{\partial x_j}\left(\mu \frac{\partial u_i}{\partial x_j}\right) \tag{2.5}$$

Mass conservation (eq.(2.4)) imposes divergence free on velocity field and does not determine the time variation of pressure. Momentum conservation imposes time variation of velocity field, but velocity field has to meet mass conservation as well. Pressure can be determined so that velocity field can meet both of these two conservations every time step.

Imposing finite difference method on eq.(2.5) about time by using Euler explicit method, it can be rewritten as this;

$$u_i{}^{n+1} = u_i{}^n + \Delta t \left[A_i{}^n - \frac{\partial P}{\partial x_i}^n + B_i{}^n \right] \tag{2.6}$$

where, $t_n = n\Delta t$, Δt denotes time step size, $P = p/\rho$, $\nu = \mu/\rho$ and

$$A_i = -u_j \frac{\partial u_i}{\partial x_j}, \qquad B_i = \frac{\partial}{\partial x_j}\left(\nu \frac{\partial u_i}{\partial x_j} \right) \tag{2.7}$$

A and B denotes convection term and diffusion term, respectively. Known velocity field $u_i{}^n$ fulfill the continuity equation (eq.(2.4)) or not, the velocity $u_i{}^{n+1}$ predicted by eq.(2.6) breaks the continuity equation to some extent because of the rounding error or discretization error. If these errors are accumulated as time steps pass, there will be a divergence. In order to avoid breaking down simulations, pressure should be determined so that the continuity equation at the following time step $\frac{\partial u_i{}^{n+1}}{\partial x_i} = 0$ can be fulfilled. In the following section, the procedure of solving pressure field which avoids breaking continuity equation at every time step is explained in detail.

2.6 **Simplified Marker And Cell (SMAC) method:**

Simplified Marker And Cell (SMAC) [39] method is one of the methods correlate continuity equation and pressure field. SMAC method is based on eq.(2.6) and separates it into these two equations.

$$u_i{}^P = u_i{}^n + \Delta t \left[A_i{}^n - \frac{\partial P^n}{\partial x_i} + B_i{}^n \right] \tag{2.8}$$

$$u_i{}^{n+1} = u_i{}^P - \Delta t \frac{\partial \varphi}{\partial x_i} \tag{2.9}$$

Solving the Poisson equation of φ instead of pressure P^{n+1},

$$\frac{\partial^2 \varphi}{\partial x_i{}^2} = \frac{1}{\Delta t} \frac{\partial u_i{}^P}{\partial x_i} \tag{2.10}$$

The pressure at the next time step can be given, which is expressed as $P^{n+1} = P^n + \varphi$. Where φ denotes scalar potential about the time variation of pressure and $u_i{}^P$ prediction of the velocity. Scalar potential φ correct the predicted velocity $u_i{}^P$ so that $u_i{}^P$ can meet the continuity equation, resulting in avoiding the breakdown of the simulation caused by the accumulated rounding and descritization error.

2.7 **Pressure equation:**

In staggered grids, scalar values such as pressure are located in the original grid points at the center of the control volumes, while velocities in the middle of two adjacent original grid points in each direction.

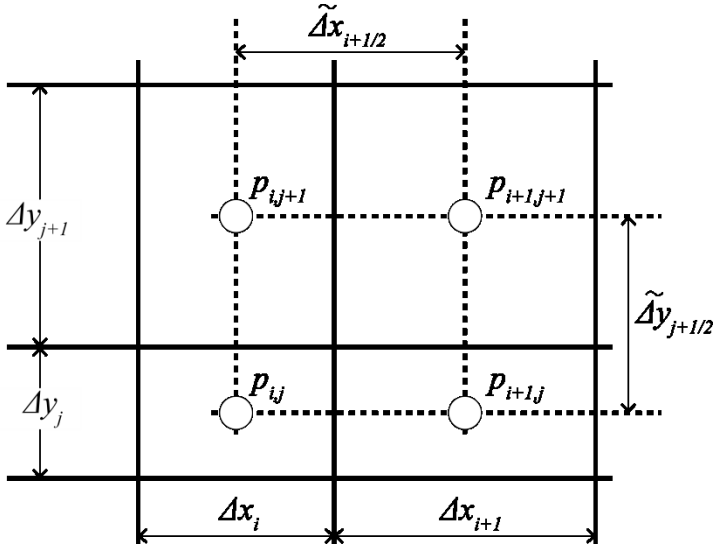

Figure 2.4 Non-uniform staggered mesh.

Fig. 2.4 illustrates an example of non-uniform grid for considering pressure equation. Assuming the grid width of the grid point (i, j) to be Δx_i, Δy_j, the correction step of SMAC method (eq.(2.9)) is expressed in staggered grid as this;

$$
\begin{aligned}
u^{n+1}_{i-\frac{1}{2},j} &= u^{P}_{i-\frac{1}{2},j} - \Delta t \frac{-\varphi_{i-1,j} + \varphi_{i,j}}{\tilde{\Delta}x_{i-\frac{1}{2}}} \\
u^{n+1}_{i+\frac{1}{2},j} &= u^{P}_{i+\frac{1}{2},j} - \Delta t \frac{-\varphi_{i,j} + \varphi_{i+1,j}}{\tilde{\Delta}x_{i+\frac{1}{2}}} \\
v^{n+1}_{i,j-\frac{1}{2}} &= u^{P}_{i,j-\frac{1}{2}} - \Delta t \frac{-\varphi_{i,j-1} + \varphi_{i,j}}{\tilde{\Delta}y_{i-\frac{1}{2}}} \\
v^{n+1}_{i,j+\frac{1}{2}} &= u^{P}_{i,j+\frac{1}{2}} - \Delta t \frac{-\varphi_{i,j} + \varphi_{i,j+1}}{\tilde{\Delta}y_{i+\frac{1}{2}}}
\end{aligned}
\tag{2.11}
$$

where,

$$
\tilde{\Delta}x_{i+\frac{1}{2}} = \frac{\Delta x_i + \Delta x_{i+1}}{2}, \qquad \tilde{\Delta}y_{j+\frac{1}{2}} = \frac{\Delta y_j + \Delta y_{j+1}}{2} \tag{2.12}
$$

$\tilde{\Delta}x_{i+\frac{1}{2}}$ and $\tilde{\Delta}y_{j+\frac{1}{2}}$ are the distance between central points of the grids (the points where pressure placed). Substituting eq.(2.11) for the discretized continuity equation,

$$\frac{-u^{n+1}_{i-\frac{1}{2},j} + u^{n+1}_{i+\frac{1}{2},j}}{\Delta x_i} + \frac{-v^{n+1}_{i,j-\frac{1}{2}} + v^{n+1}_{i,j+\frac{1}{2}}}{\Delta y_j} = 0 \tag{2.13}$$

eq.(2.13) can be rewritten as this;

$$\begin{aligned} -\frac{-\varphi_{i-1,j} + \varphi_{i,j}}{\Delta x_i \tilde{\Delta} x_{i-\frac{1}{2}}} + \frac{-\varphi_{i,j} + \varphi_{i+1,j}}{\Delta x_i \tilde{\Delta} x_{i+\frac{1}{2}}} - \frac{-\varphi_{i,j-1} + \varphi_{i,j}}{\Delta y_j \tilde{\Delta} y_{j-\frac{1}{2}}} \\ + \frac{-\varphi_{i,j} + \varphi_{i,j+1}}{\Delta y_j \tilde{\Delta} y_{j+\frac{1}{2}}} \\ = \frac{1}{\Delta t}\left(\frac{-u^{P}_{i-\frac{1}{2},j} + u^{P}_{i+\frac{1}{2},j}}{\Delta x_i} + \frac{-v^{P}_{i,j-\frac{1}{2}} + v^{P}_{i,j+\frac{1}{2}}}{\Delta y_j}\right) \end{aligned} \tag{2.14}$$

This equation proves that the staggered grid is required and helpful even though it makes program coding more complicated. In order to explain this fact in detail, the discretized pressure equation for regular grid is considered. In *Fig.* 2.5, the continuity equation at the grid point (x_i, y_j) is discretized as this;

$$\frac{-u^{n+1}_{i-1,j} + u^{n+1}_{i+1,j}}{2\Delta x} + \frac{-v^{n+1}_{i,j-1} + v^{n+1}_{i,j+1}}{2\Delta y} = 0 \tag{2.15}$$

In the final step of SMAC method, the gradient of φ is given to the velocity components $u_{i\pm1,j}, v_{i,j\pm1}$ in this way.

$$
\begin{aligned}
u_{i-1,j}^{n+1} &= u_{i-1,j}^{P} - \Delta t \frac{-\varphi_{i-2,j} + \varphi_{i,j}}{2\Delta x} \\
u_{i+1,j}^{n+1} &= u_{i+1,j}^{P} - \Delta t \frac{-\varphi_{i,j} + \varphi_{i+2,j}}{2\Delta x} \\
v_{i,j-1}^{n+1} &= u_{i,j-1}^{P} - \Delta t \frac{-\varphi_{i,j-2} + \varphi_{i,j}}{2\Delta y} \\
v_{i,j+1}^{n+1} &= u_{i,j+1}^{P} - \Delta t \frac{-\varphi_{i,j} + \varphi_{i,j+2}}{2\Delta y}
\end{aligned}
\tag{2.16}
$$

Substituting these equations for eq.(2.15) so that φ can meet eq.(2.16), the following equation can be derived.

$$
\begin{aligned}
&\frac{\varphi_{i-2,j} - 2\varphi_{i,j} + \varphi_{i+2,j}}{(2\Delta x)^2} + \frac{\varphi_{i,j-2} - 2\varphi_{i,j} + \varphi_{i,j+2}}{(2\Delta y)^2} \\
&= \frac{1}{\Delta t}\left(\frac{-u_{i-\frac{1}{2},j}^{P} + u_{i+\frac{1}{2},j}^{P}}{\Delta x_i} + \frac{-v_{i,j-\frac{1}{2}}^{P} + v_{i,j+\frac{1}{2}}^{P}}{\Delta y_j} \right)
\end{aligned}
\tag{2.17}
$$

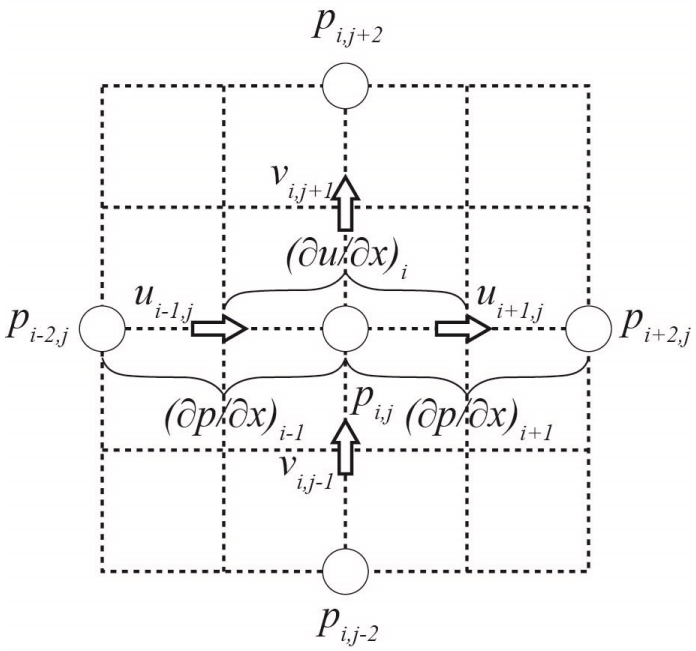

Figure 2.5: Pressure equation on regular grid.

The discretized equation (eq.(2.17)) correlates $\varphi_{i,j}$ and $\varphi_{i\pm2,j}$, $\varphi_{i,j\pm2}$ for the second order derivative terms $\partial^2\varphi/\partial x^2$, $\partial^2\varphi/\partial y^2$. To provide details, the discretized continuity equation of $\varphi_{i,j}$ (eq.(2.17)) skip the adjacent grid points' values $\varphi_{i\pm1,j}, \varphi_{i,j\pm1}$ and refer to the values $\varphi_{i\pm2,j}, \varphi_{i,j\pm2}$, which are located two points away from the original point (i,j); that is, alternating points are correlated. Therefore, the scalar potential $\varphi_{i,j}$ at the even number grid points do not refer to that at odd number grid points and vice versa. The lack of correlation between adjacent grid points causes serious problem that unrealistic pressure filed such as the one shown as an example in *Fig.* 2.6 can be accepted because that pressure field can meet the deficient continuity equation (eq.(2.17)). As seen in *Fig.* 2.6, the alternating points have the same value of pressure. Then the deficient continuity equation (eq.(2.17)) mistakenly regard this pressure field as uniform pressure field although this is obviously not uniform in reality. Eventually this results in the pressure oscillation and numerical instability. This problem is called checkerboard pressure [37]

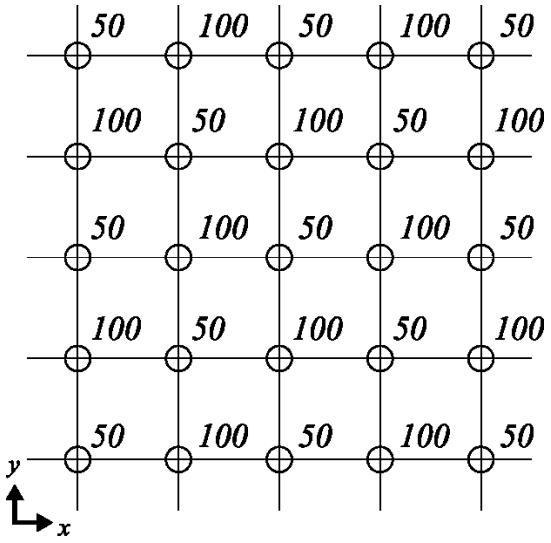

Figure 2.6: Checker board pressure distribution.

2.8 **Successive Over Relaxation (SOR) method:**

There are various ways for solving elliptic partial differential equations. Those solution methods for elliptic partial differential equations are themselves important research projects and there are so many solution methods proposed. It is impossible to define which solution method is the optimal one because it depends on the computational condition or super computers which are utilized for CFD applications. In this section, the basic iteration methods are mentioned. First, eq.(2.14) is rewritten in following manner.

$$B^{-}_{y,j}\varphi_{i,j-1} + B^{-}_{x,i}\varphi_{i-1,j} - B^{0}_{i,j}\varphi_{i,j} + B^{+}_{x,i}\varphi_{i+1,j} + B^{+}_{y,j}\varphi_{i,j+1} = \psi_{i,j} \tag{2.18}$$

where the coefficients of each term are expressed as this;

$$B^{-}_{x,i} = 1/\left(\Delta x_i \tilde{\Delta} x_{i-\frac{1}{2}}\right), \quad B^{+}_{x,i} = 1/\left(\Delta x_i \tilde{\Delta} x_{i+\frac{1}{2}}\right)$$

$$B^{-}_{y,j} = 1/\left(\Delta y_j \tilde{\Delta} y_{j-\frac{1}{2}}\right), \quad B^{+}_{y,j} = 1/\left(\Delta y_j \tilde{\Delta} y_{j+\frac{1}{2}}\right) \tag{2.19}$$

$$B^{0}_{i,j} = B^{-}_{x,i} + B^{+}_{x,i} + B^{-}_{y,j} + B^{+}_{y,j}$$

and where, $\psi_{i,j}$ denotes the right hand side of Poisson's equation.

The number of iteration is shown as m. When $\varphi^{\langle 0 \rangle}_{i,j} = 0$ is given to every grid point as an initial value, eq.(2.18) has an error. Then φ is corrected in accordance with the error. Repeating $\varphi^{\langle 1 \rangle}_{i,j}, \varphi^{\langle 2 \rangle}_{i,j}, \varphi^{\langle 3 \rangle}_{i,j}, \ldots$, it can be said that the solution for eq.(2.18) is obtained when this iteration converges. This is how an iteration method solves elliptic partial difference equations.

Jacobi method solves eq.(2.18) for $\varphi_{i,j}$ and the right hand side is given by the data of previous iteration.

$$\varphi_{i,j}^{\langle m+1\rangle} = \frac{1}{B_{i,j}^{0}}\{B_{y,j}^{-}\varphi_{i,j-1} + B_{x,i}^{-}\varphi_{i-1,j} + B_{x,i}^{+}\varphi_{i+1,j} + B_{y,j}^{+}\varphi_{i,j+1}\}^{\langle m\rangle} \tag{2.20}$$

eq.(2.20) is the step for updating $\varphi_{i\pm1,j}^{\langle m\rangle}, \varphi_{i,j\pm1}^{\langle m\rangle}$ to $\varphi_{i,j}^{\langle m\rangle}$. This is rewritten as the following.

$$\varphi_{i,j}^{\langle m+1\rangle} = \varphi_{i,j}^{\langle m\rangle} + \frac{1}{B_{i,j}^{0}}\{B_{y,j}^{-}\varphi_{i,j-1} + B_{x,i}^{-}\varphi_{i-1,j} - B_{i,j}^{0}\varphi_{i,j} + B_{x,i}^{+}\varphi_{i+1,j} + B_{y,j}^{+}\varphi_{i,j+1} - \psi_{i,j}\}^{\langle m\rangle} \tag{2.21}$$

Hence, this is the discretized equation by FDM of this following equation.

$$\varphi_{i,j}^{\langle m+1\rangle} = \varphi_{i,j}^{\langle m\rangle} + \frac{1}{B_{i,j}^{0}}\left(\frac{\partial^2\varphi_{i,j}}{\partial {x_k}^2} - \psi_{i,j}\right)^{\langle m\rangle} \tag{2.22}$$

When the program code simulate the value of $\varphi_{i,j}$, the value of $\varphi_{i-1,j}$ and $\varphi_{i,j-1}$ are already updated. Then using the updated value of $\varphi_{i-1,j}$ and $\varphi_{i,j-1}$ makes the simulation converges more quickly and the programming becomes easier. Moreover, this saves memory required for simulations. This is called Gauss-Seidel method or successive relaxation (SOR) method. The discretized equation is shown as follows.

$$\varphi_{i,j}^{\langle m+1\rangle} = \varphi_{i,j}^{\langle m\rangle} + \frac{1}{B_{i,j}^{0}}\left\{B_{y,j}^{-}\varphi_{i,j-1}^{\langle m+1\rangle} + B_{x,i}^{-}\varphi_{i-1,j}^{\langle m+1\rangle} - B_{i,j}^{0}\varphi_{i,j}^{\langle m\rangle} + B_{x,i}^{+}\varphi_{i+1,j}^{\langle m\rangle} + B_{y,j}^{+}\varphi_{i,j+1}^{\langle m\rangle} - \psi_{i,j}\right\} \tag{2.23}$$

The SOR method employs over relaxation coefficient $\beta(1 < \beta < 2)$.

$$\varphi_{i,j}^{\langle m+1\rangle} = \varphi_{i,j}^{\langle m\rangle} + \frac{\beta}{B_{i,j}^{0}}\Big\{B_{y,j}^{-}\varphi_{i,j-1}^{\langle m+1\rangle} + B_{x,i}^{-}\varphi_{i-1,j}^{\langle m+1\rangle} - B_{i,j}^{0}\varphi_{i,j}^{\langle m\rangle} + B_{x,i}^{+}\varphi_{i+1,j}^{\langle m\rangle} + B_{y,j}^{+}\varphi_{i,j+1}^{\langle m\rangle} - \psi_{i,j}\Big\} \tag{2.24}$$

In this case, the solution can be obtained when the norm of the residual becomes much smaller than that of ψ. The optimal value of β depends on the computational condition but it is normally in the range of 1.5 to 1.7.

The criterion for the convergence

When the variant of $\left\|\varphi^{\langle m+1\rangle} - \varphi^{\langle m\rangle}\right\|$ smaller than $\left\|\varphi^{\langle m+1\rangle}\right\|$, eq.(2.24) can be considered to be converged and iteration should be stopped. That is

$$\frac{\left\|\varphi^{\langle m+1\rangle} - \varphi^{\langle m\rangle}\right\|}{\left\|\varphi^{\langle m+1\rangle}\right\|} < \varepsilon' \tag{2.25}$$

can become the criterion for convergence. Where

$$\|f\| = \left[\frac{1}{N}\sum_{i=1}^{N} f_i^2\right]^{1/2} \tag{2.26}$$

is norm. ε' should be set to be depending on the accuracy required. A typical value is 10^{-5}. However, eq.(2.25) makes it hard to realize how much error eq.(2.24) and eventually the continuity equation has. Hence, the criterion can be changed as this following equation so that the residual $\left\|\frac{\partial^2\varphi}{\partial x^2} - \psi\right\|$ smaller than the value of $\|\psi\|$.

$$\frac{\left\|\frac{\partial^2\varphi^{\langle m+1\rangle}}{\partial {x_k}^2} - \psi\right\|}{\|\psi\|} < \varepsilon \tag{2.27}$$

ε should be defined so that $\frac{\partial u_i}{\partial x_i}$ corrected by φ from Poisson's is smaller than $|u_i|/\Delta$, although ε does not have normal optimal value. However, it is necessary to define the limitation of the number of iterations because it sometimes takes much time under some grid arrangements or boundary conditions.

In section 2.5, the time discretization is based on the first order Euler's method because of its simplicity. However, the first order Euler's method is not stable or not accurate when dealing with unsteady state phenomena. Hence, the first order Euler's method cannot be applicable unless it improves its accuracy or stability. There are some ways for enhancing stability and accuracy of time discretization such as the Adams-Bashforth method, Crank-Nicolson method or Runge-Kutta method. In this study, the second order Adams-Bashforth method is applied to convective term and diffusion term because of its stability, accuracy and simplicity features. Furthermore, the Adams-Bashforth method is relatively simpler than Runge-Kutta method because the former requires only one step for the time discretization of momentum equation (eq.(2.28)). However, the Adams-Bashdorth method becomes less stable as its order becomes higher. Therefore, this study employed the second order Adams-Bashforth method for a time discretization of the momentum equation. Convective term and diffusion term in the prediction step of SOR method (eq.(2.8)) can be rewritten by the second order Adams-Bashforth method as follows.

$$u_i^{n+1} = u_i^n + \Delta t \left[-\frac{\partial P^n}{\partial x_i} + \frac{3(A_i^n + B_i^n) - \left(A_i^{n-1} + B_i^{n-1}\right)}{2} \right] \tag{2.28}$$

2.9 **Large Eddy Simulation (LES):**

There are various eddies in the range of large scale to small scale in a turbulence field. Turbulence can be considered to be the flow which consists of large scale eddies and small scale eddies. In order to simulate turbulence directly, it is necessary to arrange a computational mesh which is able to resolve all kinds of scales of eddies. In the case where the computational mesh is prepared for numerical analysis for turbulence field, eddies which are larger than a mesh size can be treated by the discrete value on grid points, while eddies which are smaller than a mesh size cannot. Therefore, the mesh size should be smaller than the smallest scale of turbulent eddies, that is Kolmogorov scale. This is why the number of the required grid points should be at least more than $\mathrm{Re}^{9/4}$. Moreover, a time step size must be smaller as the mesh size becomes smaller in order to make the simulation stable and meet the Courant-Friedrichs-Lewy (CFL) requirement, resulting in the extremely high computational cost. Hence, it is not applicable for industrial applications and not suitable for a practical use of simulating turbulence.

Eddies can be classified into Grid Scale (GS) eddies which is larger than the grid size and Sub-Grid Scale (SGS) which is smaller than the grid size by enlarging grid size and applying coarse graining to the turbulence field so that the computational time can be reduced and it can become a more practical method. It will become possible to simulate

turbulence precisely with a coarse mesh by applying a turbulence model to SGS eddies which cannot be resolved by a computational mesh. This method is called the Large Eddy Simulation (LES).

Three different common CFD methods for turbulence are compared in Table 2.1. As shown in Fig. 2.7, the Direct Numerical Simulation (DNS) shows small fluctuations and most accurate velocity profiles. However, the computational grid for the DNS is extremely dense, which is not practical for industrial applications. On the contrary, the LES employs less dense mesh but can show fluctuations, although the scale of fluctuations is not as small as that of the DNS. In addition, as shown in Fig.2.7 about the relationship between turbulence energy spectrum $E(k)$ and the turbulence wave number κ, the RANS are able to model all scales of eddies, while the LES models small scale eddies only and can directly resolve large fluctuations without modeling. Hence, it is clear that the LES can provide more accurate predictions than the RANS.

Fig. 2.8 illustrates the applicable range of comparison of DNS, LES and RANS. The LES shows larger applicable range than RANS, which is an advantage of the LES over RANS.

Considering the computational cost, accuracy and the applicable range, LES is more promising to provide more benefits than RANS when used in predictions of industrial applications. Therefore, it is meaningful to reduce the computational cost of LES by employing the analytical wall function (AWF) so that the LES can be a more practical CFD method for turbulence predictions.

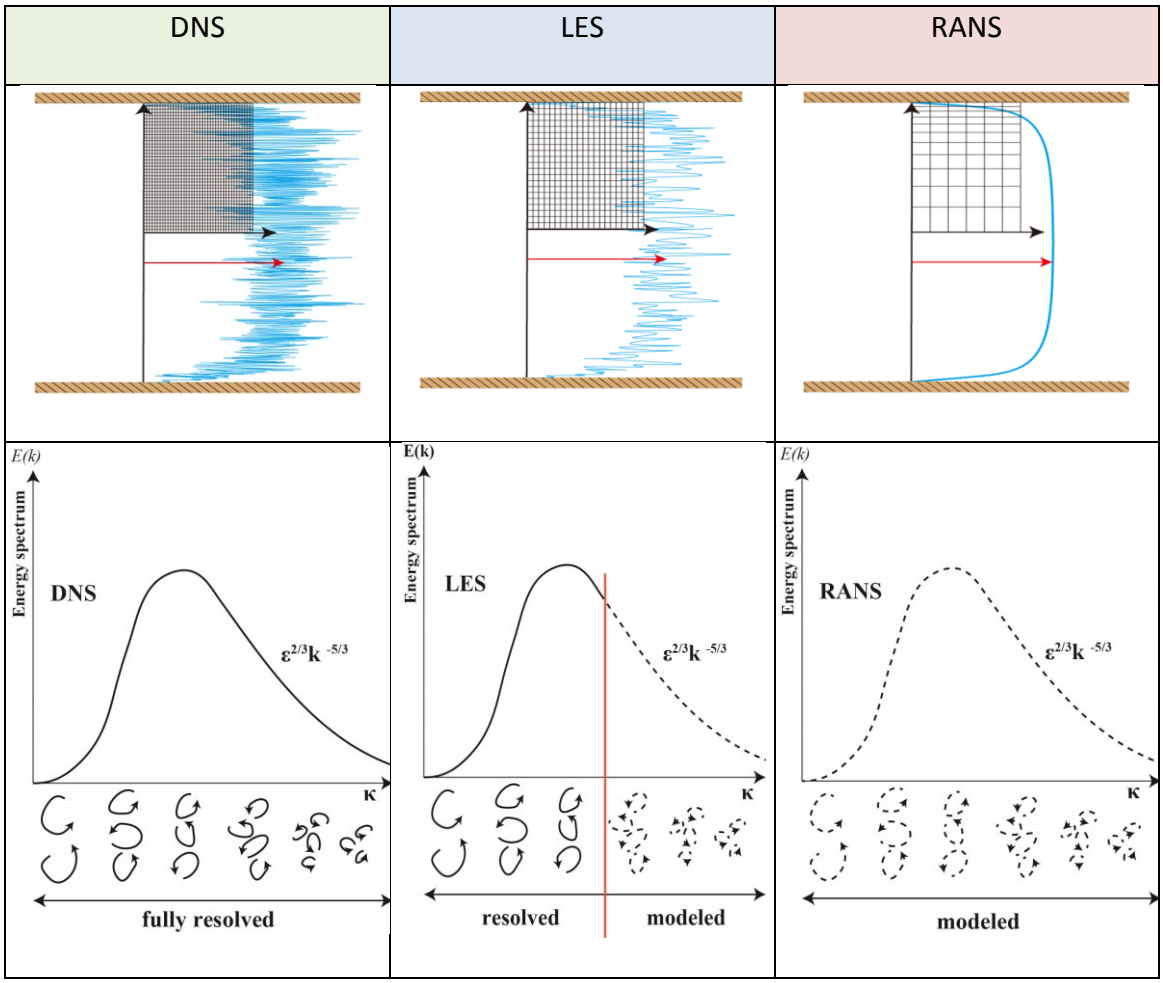

Figure 2.7: Illustrative comparison of DNS, LES and RANS simulations of a fully developed, steady turbulent flow in a plane channel.

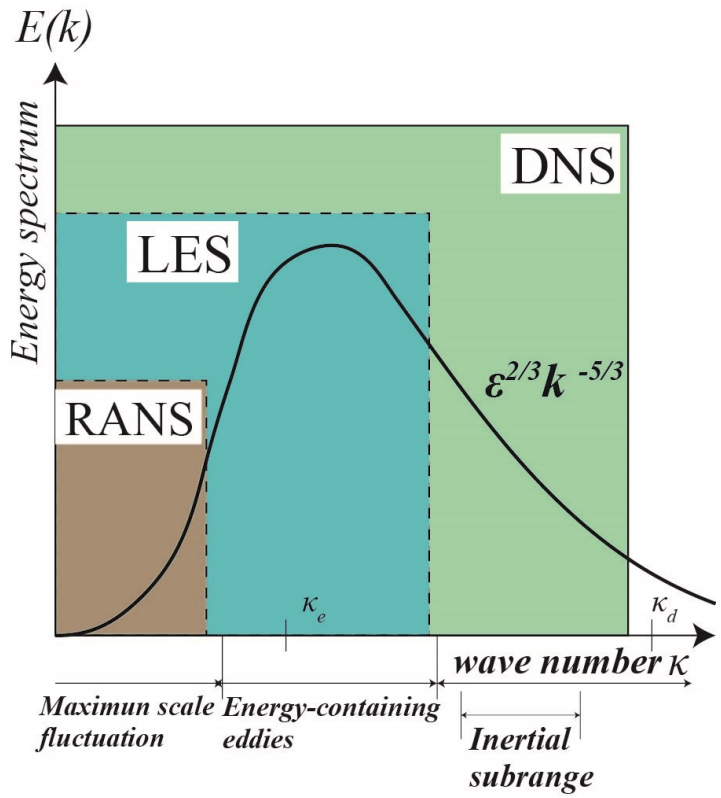

Figure 2.8: Applicable range comparison of DNS,LES and RANS.

2.10 **Filtering operation:**

The LES needs to classify eddies into GS eddies and SGS eddies as shown in *Fig.* 2.9. This sifting operation is called a filtering operation. The velocity u is separated in this way by employing the filtering operator $\langle \quad \rangle$.

$$u(x) = \langle u(x) \rangle + \widetilde{u(x)} \tag{2.29}$$

Moreover, filtering operation is expressed as follows:

$$\langle u(x) \rangle = \int_{-\infty}^{\infty} G(x)u(x)dx \tag{2.30}$$

where $G(x)$ denotes filtering function and there are various kinds of filtering functions. Filtering functions have to be positive around $x = 0$, have this limiting value $\lim_{x\to\pm\infty} G(x) = 0$ and meet this condition;

$$\int_{-\infty}^{\infty} G(x)dx = 1 \tag{2.31}$$

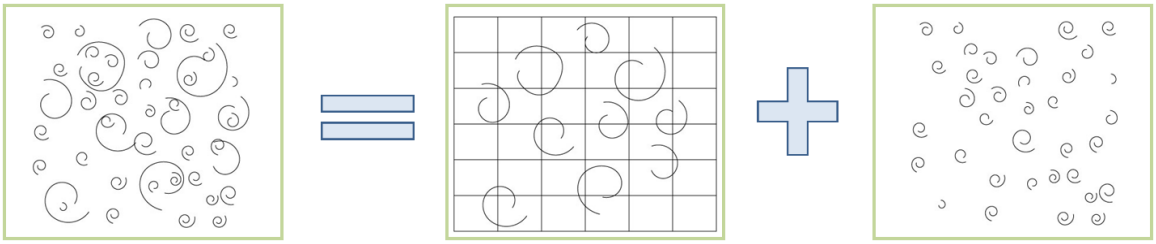

Turbulence Field u_i, p | Grid Scale (GS) Field $\langle u_i \rangle, \langle p \rangle$ | Sub-Grid Scale (SGS) Field $\widetilde{u_i}, \tilde{p}$

Figure 2.9: Decomposition of turbulence field.

Then $\langle u(x) \rangle$ becomes weighted mean value by $G(x)$ around x. In this study, box filter (the filter width is Δ) is applied to filter function as shown in *Fig.* 2.10. The filter function $G(x)$ is expressed as this;

$$G(x) = \begin{cases} \frac{1}{\Delta} & \left(|x| < \frac{\Delta}{2}\right) \\ 0 & \left(|x| > \frac{\Delta}{2}\right) \end{cases} \tag{2.32}$$

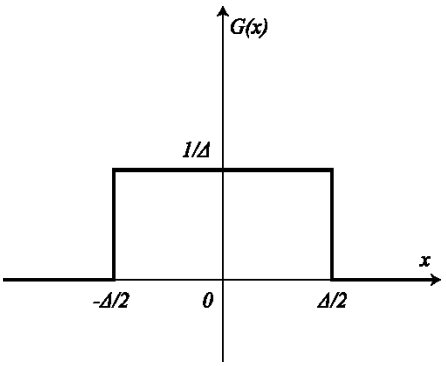

Figure 2.10: Box Filter.

The filter size which classifies eddies into large scale eddies and small scale eddies has to be defined. When the filter size is defined as mesh size, it can make the most of the resolution of numerical analysis. This is the reason why the scale extracted by the filter is Grid Scale. On the other hand, the fluctuation from $\langle u(x) \rangle$ is SGS part.

$$\widetilde{u(x)} = u(x) - \langle u(x) \rangle \tag{2.33}$$

Generally, filtering operation meets these conditions.

$$\begin{gathered} \langle \tilde{f} \rangle = 0, \quad \langle \langle f \rangle \rangle = \langle f \rangle \\ \langle \langle f \rangle \cdot \tilde{g} \rangle \neq 0, \quad \langle \tilde{f} \cdot \langle g \rangle \rangle \neq 0 \\ \langle \frac{\partial f}{\partial x} \rangle = \frac{\partial \langle f \rangle}{\partial x} \end{gathered} \tag{2.34}$$

However, in the case of box filtering, there is no weight imposed inside the filter width Δ. The following equations are applied in the present study, although they are different from eq.(2.34).

$$\langle \langle f \rangle \cdot \tilde{g} \rangle = 0, \quad \langle \tilde{f} \cdot \langle g \rangle \rangle = 0 \tag{2.35}$$

Eq.(2.35) is applicable only when filter function on which no weight is imposed such as box filter is adopted as a filter function $G(x)$. This can be explained in detail by

the definition of filtering operation (eq.(2.30)). Taking the first equation of eq.(2.35) as an example , it is rewritten as this;

$$\begin{aligned}\langle\langle f(x)\rangle \cdot \tilde{g}(x)\rangle &= \int_{-\infty}^{\infty} G(x)\{\langle f(x)\rangle \cdot \tilde{g}(x)\}dx \\ &= \int_{-\infty}^{\infty} G(x)\left\{\int_{-\infty}^{\infty} G(x)f(x)dx\right\}\tilde{g}(x)dx\end{aligned} \tag{2.36}$$

where, $\int_{-\infty}^{\infty} G(x)f(x)dx$ is the constant value regardless of the value x because of the box filter, which does not include weight inside the filter width Δ (see Fig. 2.10 and eq.(2.32)). Hence, $\int_{-\infty}^{\infty} G(x)f(x)dx$ can be put outside of the integration and rewritten as this;

$$\begin{aligned}\langle\langle f(x)\rangle \cdot \tilde{g}(x)\rangle &= \int_{-\infty}^{\infty} G(x)\left\{\int_{-\infty}^{\infty} G(x)f(x)dx\right\}\tilde{g}(x)dx \\ &= \left\{\int_{-\infty}^{\infty} G(x)f(x)dx\right\} \cdot \int_{-\infty}^{\infty} G(x)\tilde{g}(x)dx \qquad (2.37) \\ &= 0 \quad \left(\because \langle\tilde{g}\rangle = \int_{-\infty}^{\infty} G(x)\tilde{g}(x)dx = 0 \ \text{(eq. (2.34)}\right)\end{aligned}$$

Therefore, eq.(2.35) is applicable with box filter.

2.11 **The governing equations for LES:**

The governing equations for LES can be derived by applying filtering operation to the continuity equation and Navier-Stokes equations.

Filtered continuity equation

$$\frac{\partial \langle u_i \rangle}{\partial x_i} = 0 \tag{2.38}$$

Filtered Navier-Stokes equation

$$\frac{\partial \langle u_i \rangle}{\partial t} + \langle u_j \rangle \frac{\partial \langle u_i \rangle}{\partial x_j} = -\frac{1}{\rho}\frac{\partial \langle p \rangle}{\partial x_i} + \nu \frac{\partial^2 \langle u_i \rangle}{\partial {x_j}^2} - \frac{\partial \tau_{ij}}{\partial x_j} \tag{2.39}$$

These equations include filtering averaged value $\langle \quad \rangle$ and the unknown third term in the right hand side of eq.(2.39), that is gradient of SGS stress term $\tau_{ij} = \langle u_i u_j \rangle - \langle u_i \rangle \langle u_j \rangle$. Hence, this equation is not closed. The physical model for SGS stress, that is SGS model, is needed to be introduced in order to resolve GS fields.

SGS stress is separated in the following way. Substituting GS part $\langle u_i \rangle$ and SGS part $\widetilde{u_i}$, which are separated from the velocity u_i, for the definition of SGS stress, SGS stress can be written as this.

$$\begin{aligned} \tau_{ij} &= \langle u_i u_j \rangle - \langle u_i \rangle \langle u_j \rangle \\ &= \langle (\langle u_i \rangle + \widetilde{u_i})\big(\langle u_j \rangle + \widetilde{u_j}\big) \rangle - \langle u_i \rangle \langle u_j \rangle \\ &= \langle \langle u_i \rangle \langle u_j \rangle \rangle - \langle u_i \rangle \langle u_j \rangle + \langle \langle u_i \rangle \widetilde{u_j} \rangle + \langle \widetilde{u_i} \langle u_j \rangle \rangle + \langle \widetilde{u_i} \widetilde{u_j} \rangle \end{aligned} \tag{2.40}$$

where,

- L_{ij} : Leonard term

  This term expresses a part of stress given to GS eddies because of the interaction with SGS eddies. This controls a part of energy dissipation of GS eddies.

- C_{ij} : Cross term

  C_{ij} also controls a large part of energy dissipation of GS eddies with L_{ij}. In the case where box filter is applied, $\langle u_i u_j \rangle - \langle u_i \rangle \langle u_j \rangle$ is directly modeled because C_{ij}

becomes zero from eq.(2.36). C_{ij} and L_{ij} both have almost the same values and the effect of these two terms' are normally neglected because they cancel out each other.

- R_{ij} : SGS Reynolds stress term

  Generally, SGS modelling refers to the modeling for SGS Reynolds stress term R_{ij}. This term controls a large part of the effect on GS eddies by SGS eddies and have to include the effect of the energy dissipation.

  The eddy viscosity model, which defines the stress caused by turbulence eddies from the analogy of molecular viscous stress, is widely used for RANS and Reynolds stress is defined as this;

$$\overline{u_i' u_j'} = \frac{2}{3}\delta_{ij}k - 2\nu_t\left(\frac{\partial \overline{u}_i}{\partial x_j} + \frac{\partial \overline{u}_j}{\partial x_i}\right) \tag{2.41}$$

  The model which applied the same idea as that of eddy viscosity model for RANS to LES is called SGS eddy viscosity model. Since the parameter which has to be modeled is SGS Reynolds stress, this is modeled by SGS turbulence kinetic energy k_{SGS} and SGS eddy kinematic viscosity ν_{SGS}.

$$\tau_{ij} = \langle \widetilde{u}_i \widetilde{u}_j \rangle = \frac{2}{3}\delta_{ij}k_{SGS} - 2\nu_{SGS}\left(\frac{\partial \langle u_i \rangle}{\partial x_j} + \frac{\partial \langle u_j \rangle}{\partial x_i}\right) \tag{2.42}$$

  SGS eddy viscosity models are different from each other in the way of modeling ν_{SGS}.

2.12 **Smagorinsky model [40]:**

Sifting turbulence fields by filtering operation, kinetic energy $k = u_k u_k/2$ is separated into GS part $k_{GS} = \langle u_k \rangle \langle u_k \rangle/2$ and SGS part $k_{SGS} = (u_k u_k - \langle u_k \rangle \langle u_k \rangle)/2$.

The transport equation of GS energy k_{GS}

$$\frac{\partial k_{GS}}{\partial t} + \langle u_j \rangle \frac{\partial k_{GS}}{\partial x_j} = \tau_{ij} \langle S_{ij} \rangle - \varepsilon_{GS} + \frac{\partial}{\partial x_j} \left[-\langle u_i \rangle \tau_{ij} - \frac{\langle p \rangle \langle u_j \rangle}{\rho} + \nu \frac{\partial k_{GS}}{\partial x_j} \right] \tag{2.43}$$

includes $\tau_{ij} \langle S_{ij} \rangle$ as trasport efficiency to SGS turbulence kinetic energy k_{SGS}. On the other hand, the transport equation of SGS turbulence kinetic energy k_{SGS}

$$\frac{\partial k_{SGS}}{\partial t} + \langle u_j \rangle \frac{\partial k_{SGS}}{\partial x_j} = \tau_{ij} \langle S_{ij} \rangle - \varepsilon_{SGS} + \frac{\partial}{\partial x_j} \left[-\langle u_i \rangle \tau_{ij} - \frac{1}{2} \left(\langle u_i u_i u_j \rangle + \langle u_j \rangle \langle u_i u_i \rangle \right) - \frac{\langle p u_j \rangle - \langle p \rangle \langle u_j \rangle}{\rho} + \nu \frac{\partial k_{SGS}}{\partial x_j} \right] \tag{2.44}$$

includes $-\tau_{ij} \langle S_{ij} \rangle$ as the production rate. Assuming the local equiribrium that this production rate is balanced with SGS energy dissipation ε_{SGS},

$$\varepsilon_{SGS} (= \varepsilon - \varepsilon_{GS}) = \nu \left\langle \frac{\partial u_i}{\partial x_j} \frac{\partial u_i}{\partial x_j} \right\rangle - \nu \frac{\partial \langle u_i \rangle}{\partial x_j} \frac{\partial \langle u_i \rangle}{\partial x_j} \tag{2.45}$$

ε_{SGS} is expressed as follows:

$$\varepsilon_{SGS} = -\tau_{ij} \langle S_{ij} \rangle \tag{2.46}$$

The Boussinesq eddy viscosity approximation is applied to SGS stress τ_{ij} from the analogy of a molecular viscosity or an eddy viscosity for the Reynolds stress mentioned in the previous section.

$$\tau_{ij}^{a} = -2\nu_{SGS}\langle S_{ij}\rangle \tag{2.47}$$

In this section, an anisotropic part is expressed by the super script a such as $\tau_{ij}^{a} = \tau_{ij} - \delta_{ij}\tau_{kk}/3$. Since $\tau_{ij}^{a}\langle S_{ij}\rangle = \tau_{ij}\langle S_{ij}\rangle$ from the traceless condition ($\langle S_{ii}\rangle = 0$), it is allowed for only the anisotropic part τ_{ij}^{a} to be multiplied to $\langle S_{ij}\rangle$, resulting in the same product of the whole part τ_{ij} and $\langle S_{ij}\rangle$.

Since the SGS eddy viscosity has the scale of the product of a velocity scale q and a length scale l, the SGS eddy viscosity is written as follows.

$$\nu_{SGS} = C_v q l \tag{2.48}$$

Substituting SGS eddy viscosity (eq.(2.48)) to the assumption of local equilibrium (eq.(2.46)), ε_{SGS} can be obtained as $\varepsilon_{SGS} = 2\nu_{SGS}\langle S_{ij}\rangle\langle S_{ij}\rangle$. Considering the scale of dissipation rate,

$$\nu_{SGS}\langle S_{ij}\rangle\langle S_{ij}\rangle = C_v\, q^3/l \tag{2.49}$$

This scale is defined by q and l. Eliminating q from eq.(2.48) and eq.(2.49) and employing filter width Δ for l, SGS eddy viscosity can be obtained as this.

$$\nu_{SGS} = (C_S\Delta)^2\left|S_{ij}\right| \tag{2.50}$$

This is the Smagorinsky model [40]. $\left|S_{ij}\right|$ is a GS strain rate tensor give as:

$$|S_{ij}| = \sqrt{2\langle S_{ij}\rangle\langle S_{ij}\rangle} \tag{2.51}$$

C_S is the only one no dimensional constant for this model and it is called the Smagorinsky constant.

From the assumption of local equilibrium, ε_{SGS} is given as follows:

$$\varepsilon_{SGS} = (C_S\Delta)^2|S_{ij}|^3 \tag{2.52}$$

From the Lilly's turbulence statistic theory [41], it is assumed as follows:

$$\frac{1}{2}|S_{ij}|^2 = \int_0^{\pi/\Delta} k^2 E(k)dk = \frac{3}{4}\alpha\varepsilon^{2/3}\left(\frac{\pi}{\Delta}\right)^{4/3} \tag{2.53}$$

The Kolmogorov spectrum $E(k) = \alpha\varepsilon^{2/3}k^{-5/3}$ is applied to $E(k)$ in eq.(2.53). Moreover, if Δ is in the range of inertial sub-range, there is not a large error even though it is assumed that viscous dissipation is as large as SGS dissipation ($\varepsilon = \varepsilon_{SGS}$). Hence,

$$C_S = \frac{1}{\pi}\left(\frac{3\alpha}{2}\right)^{-3/4} = 0.235\alpha^{-3/4} \tag{2.54}$$

$and\ C_S$ can be obtained. Substituting the Kolmogorov constant $\alpha = 1.5$, C_S becomes 0.173, which is assumed to be the theoretical value. In this study C_S is set to 0.1.

The Smagorinsky model is derived from the assumption of a local equilibrium and the eddy viscosity and from the length scale Δ. Moreover, the only one no dimensional constant C_S is derived from the assumption of the Kolmogorov spectrum.

2.13 **Analytical Wall Function (AWF):**

A near wall treatment is significantly important for a numerical analysis of turbulence. The specific method for accurately analyzing near wall turbulence is mandatory for realistic simulations because there is a large variant such as the velocity in a near wall region. There are two common methods for this purpose. One is the use of a Low Reynolds Number model. This model requires a great deal of computational time because of the requirement of a fine computational mesh in wall vicinity, although this method considers a low Reynolds number effect in the near wall region. The other is the use of a wall function, which can substantially reduce a computational time because it does not need to arrange a fine mesh in the near wall region due to the employment of the log law of the wall for a fully developed turbulent boundary layer and by simplifying the governing equations in the near wall region. However, this method is based on the assumption of the semi empirical log law. Hence, it has a problem that there is a large error in complex geometry flows that accompany stagnation or separation points. The new wall function AWF is invented and it was successfully applied to RANS [1,6-10,12,13]. The AWF is applicable for those flows in complex geometries because it defines boundary conditions as a turbulence wall function model by integrating the boundary layer equation in wall adjacent cells. For this reason, the AWF has an advantage over a standard wall function.

However, the AWF needs some modifications so that it can be applied to the LES but not RANS; this is because the AWF is a wall function used for a steady state simulation such as RANS. Conventional AWF for LES (LES-AWF) [11,34] adopted the same way as original AWF for RANS (RANS-AWF), although LES is an unsteady state

simulation. In this study, LES is modified to be an instantaneous wall function applicable for a LES.

In order to introduce the AWF, the basic theory and processes for deriving the AWF are mentioned in this section.

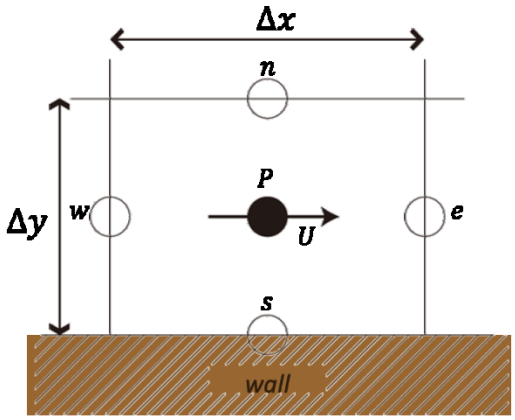

Figure 2.11: Near wall grid arrangement.

When wall adjacent cells as shown in *Fig.* 2.11 are analyzed by FDM, the steady state transport equation of physical value φ is expressed as eq.(2.55) from the assumption that $v \cong 0$ because of wall vicinity condition and the cells being inside the boundary layer.

$$\frac{\partial}{\partial x}(\rho u \varphi) = \frac{\partial}{\partial y}\left(\mu \frac{\partial \varphi}{\partial y}\right) - \frac{\partial S_{\varphi}}{\partial x} \qquad (2.55)$$

where, S_{φ} is the production term which shows pressure gradient. The discretized equation of eq.(2.55) by FDM is written as follows:

$$\frac{(\rho u\varphi)_e - (\rho u\varphi)_w}{\Delta x} = \frac{\left(\Gamma \frac{\partial \varphi}{\partial y}\right)_n - \left(\Gamma \frac{\partial \varphi}{\partial y}\right)_s}{\Delta y} + \frac{(S_\varphi)_e - (S_\varphi)_w}{\Delta x} \quad (2.56)$$

In the case of momentum equation, φ corresponds to u and Γ to μ, respectively. Therefore, in wall adjacent cells, $(\Gamma\, \partial\varphi/\partial y)_s$ corresponds to wall shear stress $\tau_w = \mu(\partial u/\partial y)|_{wall}$, and the discretized equation of eq.(2.56) can be solved by obtaining τ_w. The AWF is a method for defining τ_w, and the way how AWF is applied to LES is mentioned in the next section.

2.14 **The conventional AWF for LES (LES-AWF):**

One of the most important elements for the AWF is the modeling of the SGS eddy viscosity. In this section, the modeling of SGS eddy viscosity by a conventional LES-AWF is mentioned. Originally, the SGS eddy viscosity is instantaneous parameter which changes in every iteration. Hence, the modeling of the SGS eddy viscosity should be instantaneous. However, since the conventional LES-AWF refers to the idea of one-equation model for RANS, which is a steady state simulation, it models the SGS eddy viscosity by using constant parameters. Then, the modeling of the SGS eddy viscosity is not instantaneous even for unsteady state simulations of the LES. This is the purpose of the study.

The SGS eddy viscosity modeling of the conventional LES-AWF adopts the idea of one-equation model for RANS. The first grid point closest to the wall employs the AWF. The SGS eddy viscosity is modeled in the fllowing manner:

$$\begin{aligned} \nu_{SGS} &= c_\mu \sqrt{k_{SGS}} \Delta \\ &= c_\mu \sqrt{k_{SGS}} c_l y \\ &\cong \alpha \nu y^+ \end{aligned} \tag{2.57}$$

where $\alpha = c_\mu c_l = 2.55 \times 0.09$ and y^+ is non-dimensional length scale normalized by the wall friction velocity. Moreover, the viscous sub-layer is assumed to be shown in *Fig.* 2.12 and expressed as follows.

$$\nu_{SGS} = \max[0, \alpha \nu (y^+ - y_v^+)] \tag{2.58}$$

where, y_v denotes the thickness of viscous sub-layer and determined as $y_v^+ = 5.86$ by the numerical experiment.

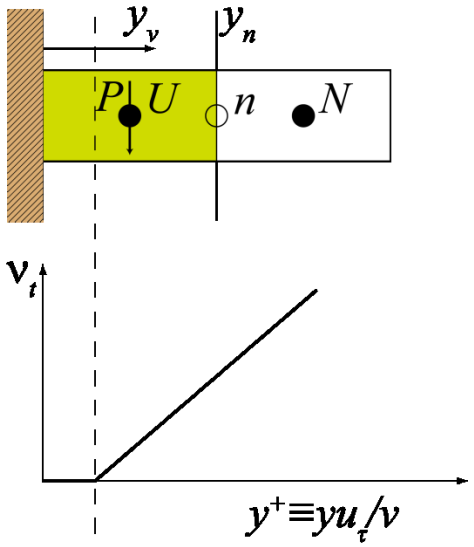

Figure 2.12: SGS eddy viscosity profile in near wall region.

The transport equation in the wall tangential direction simplified by the boundary layer approximation is expressed by eq.(2.59) and applied to the wall adjacent cells shown in *Fig.* 2.12.

$$\frac{\partial}{\partial y^+}\left[(\nu+\nu_{SGS})\frac{\partial\langle u\rangle}{\partial y^+}\right]=\frac{\nu^2}{{u_\tau}^2}\left[\frac{\partial\langle u\rangle}{\partial t}+\langle u\rangle\frac{\partial\langle u\rangle}{\partial x}+\frac{1}{\rho}\frac{\partial\langle p\rangle}{\partial x}\right] \qquad (2.59)$$

(i) In the case where $y^+ \le y_v^+$,

From the eq.(2.57) and eq.(2.58), the transport equation (eq.(2.59)) is rewritten as follows;

$$\frac{\partial}{\partial y^+}\left[\nu\frac{\partial u}{\partial y^+}\right]=C_U \qquad (2.60)$$

where C_U is assumed to be a constant in a wall adjacent cell P and eq.(2.60) can be analytically integrated in this way.

$$\frac{\partial\langle u\rangle}{\partial y^+}=\frac{C_U y^+ + A_U}{\nu}$$

and (2.61)

$$\langle u\rangle=\frac{1}{2\nu}C_U{y^+}^2+\frac{1}{\nu}C_U y^+ + B_U$$

Integration constants A_U and B_U are determined from the boundary conditions written as follows.

$$\langle u\rangle|_{y^+=0}=0 \ \ (no$$

and $$-\ slip\ boundary\ condition\ on\ the\ wall) \qquad (2.62)$$

$$\langle u\rangle|_{y^+=y_n{}^+}=\langle u_n\rangle \ \ (the\ velocity\ at\ the\ node\ n)$$

From the assumption that the velocity at the node n is $\langle u_n\rangle$ $\left(\langle u\rangle|_{y^+=y_n{}^+}=\langle u_n\rangle\right)$, the integration constant A_U is determined as this

$$A_U = \frac{\nu\langle u_n\rangle - \frac{1}{2}C_U {y_n}^{+^2}}{{y_n}^{+^2}} \tag{2.63}$$

From the assumption of no-slip boundary condition on the wall $\left(\langle u\rangle|_{y^+=0} = 0\right)$ and eq. (2.62), the constant of integration B_U is determined as follows:

$$B_U = 0 \tag{2.64}$$

(ii) In the case where $y^+ \geq {y_v}^+$, from

from eq.(2.57) and eq.(2.58), the transport equation (eq.(2.59)) is rewritten as follows:

$$\frac{\partial}{\partial y^+}\left[(\nu + \nu_{SGS})\frac{\partial\langle u\rangle}{\partial y^+}\right] = C_U \tag{2.65}$$

Assuming that C_U is constant in the wall adjacent cell P, the eq.(2.65) can be integrated analytically as follows:

$$\frac{\partial\langle u\rangle}{\partial y^+} = \frac{C_U y^+ + {A_U}'}{\nu\{1 + \alpha(y^+ - {y_v}^+)\}} \tag{2.66}$$

and

$$\langle u\rangle = \frac{C_U}{\alpha\nu}y^+ + \left\{\frac{{A_U}'}{\alpha\nu} - \frac{C_U}{\alpha^2\nu}(1 - \alpha {y_v}^+)\right\} \times \ln[1 + \alpha(y^+ - {y_v}^+)] + {B_U}' \tag{2.67}$$

The integration constants ${A_U}'$, ${B_U}'$ can be derived from the condition of continuity which can be applied to Eq.(2.66) and Eq.(2.67).

From the condition of continuity of $\frac{\partial\langle u\rangle}{\partial y^+}$ at $y^+ = {y_v}^+$, the constant of integration ${A_U}'$ can be determined as follows:

$$A_U{}' = \frac{\alpha\nu\langle u_n\rangle - C_U({y_n}^+ - {y_v}^+) + \frac{C_U(1-\alpha {y_v}^+)}{\alpha}\ln Y^+ - \frac{\alpha}{2}C_U {{y_v}^+}^2}{\alpha {y_v}^+ + \ln Y^+} \quad (2.68)$$

and $$Y^+ = 1 + \alpha(y^* - {y_v}^+) \quad (2.69)$$

In addition, from the condition of continuity of $\langle u\rangle$ at ${y^+ = y_v}^+$, the constant of integration $B_U{}'$ can be determined as:

$$B_U{}' = \frac{C_U}{2\nu}{{y_v}^+}^2 + \left(\frac{A_U}{\nu} - \frac{C_U}{\alpha\nu}\right){y_v}^+ \quad (2.70)$$

Therefore, the wall shear stress τ_w can be determined as this.

$$\frac{\tau_w}{\rho} = \nu\left.\frac{\partial\langle u\rangle}{\partial y}\right|_{y=0} = \nu\frac{u_\tau}{\nu}\left.\frac{\partial\langle u\rangle}{\partial y^+}\right|_{y^+=0} = \frac{u_\tau A_U}{\nu} \quad (2.71)$$

2.15 **The modification for three-dimensional computation:**

Since the AWF employs the coordinate system along the instantaneous flow direction, it requires the coordinate transformation so that it can be applicable to three-dimensional computations. In section 2.14, x direction and y direction refers the wall tangential direction and the wall normal direction of instantaneous flow direction, respectively, but they do not necessarily correspond to x, y and z directions of the three-dimensional physical coordinate system. As shown in *Fig.* 2.15, the mean flow direction, normal direction and spanwise directions in the three-dimensional physical coordinate based on the structure of computational geometry system are defined as (x, y, z) directions, respectively. On the other hand, the wall tangential and normal directions of the instantaneous velocities and another wall tangential direction which is normal to the

other wall tangential directions of instantaneous velocities in wall coordinate system for the AWF are defined as (ξ, η, ζ). Then it is obvious that the physical coordinate system does not always correspond to the wall coordinate system as shown in *Fig.* 2.15 (For example, the wall normal directions y and η correspond to each other in both coordinate systems). Since the AWF is proposed that it is applicable to the wall coordinate system, the transport equation written in the previous section should be rewritten for the wall coordinate system. That is expressed as follows:

$$\frac{\partial}{\partial \eta^+}\left[(\nu + \nu_{SGS})\frac{\partial \langle u_\xi \rangle}{\partial \eta^+}\right] = \frac{\nu^2}{{u_\tau}^2}\left[\frac{\partial \langle u_\xi \rangle}{\partial t} + \rho \langle u_\xi \rangle \frac{\partial \langle u_\xi \rangle}{\partial \xi} + \frac{1}{\rho}\frac{\partial \langle p \rangle}{\partial \xi}\right] \tag{2.72}$$

The coordinate transformation between two different coordinate systems is required so that the AWF can be applied to the computation in the wall adjacent cell P.

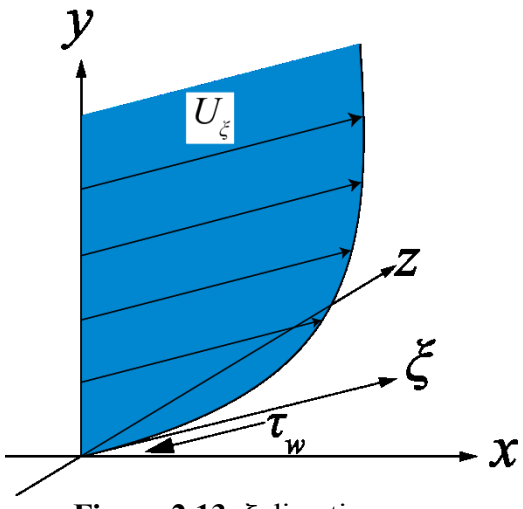

Figure 2.13: ξ direction.

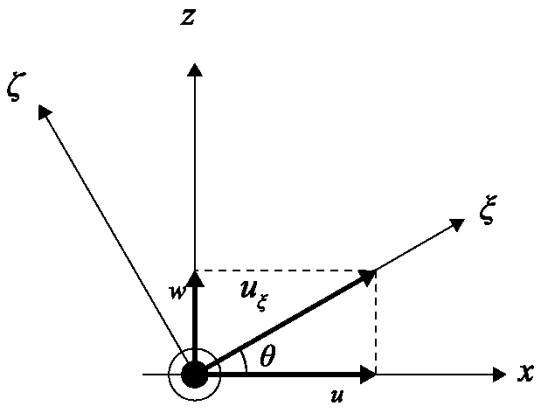

Figure 2.14: velocity ξ direction.

First, since the wall normal direction (y direction and η direction) of both coordinate systems correspond to each other, the coordinate transformation from physical

coordinate system to the wall coordinate system can be considered to be the rotation by ϑ degree along the y axis. Hence, the wall tangential component of instantaneous velocity u_ξ is expressed as follows:

$$u_\xi = \sqrt{u^2 + w^2} \tag{2.73}$$

Moreover, $\sin\vartheta$ and $\cos\vartheta$ can be expressed by u_ξ, u, w as follows (see *Fig.* 2.14);

$$\sin\vartheta = \frac{w}{u_\xi}, \quad \cos\vartheta = \frac{u}{u_\xi} \tag{2.74}$$

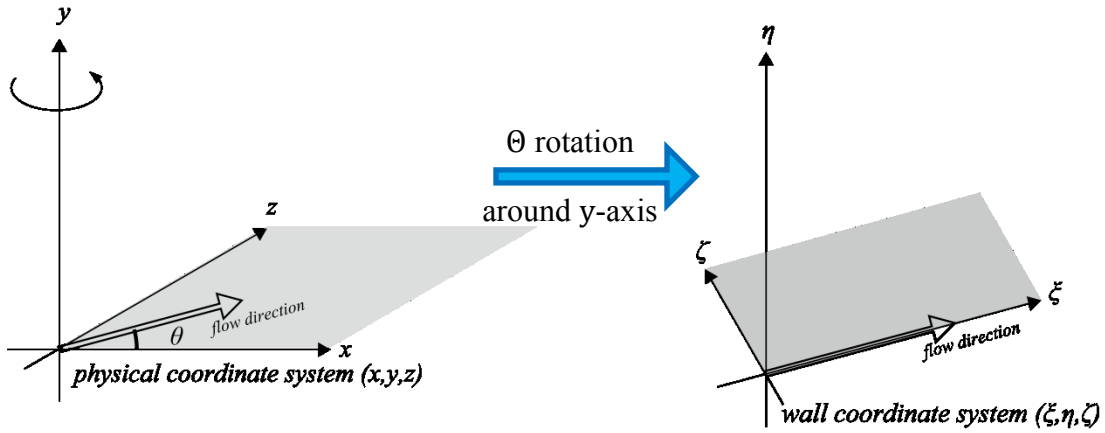

Figure 2.15: physical coordinate system and wall coordinate system.

Second, the derivatives in the wall coordinate system $\left(\frac{\partial}{\partial\xi}, \frac{\partial}{\partial\eta}, \frac{\partial}{\partial\zeta}\right)$ are expressed as follows:

$$\begin{aligned}
\frac{\partial\varphi}{\partial\xi} &= \frac{\partial\varphi}{\partial x}\frac{\partial x}{\partial\xi} + \frac{\partial\varphi}{\partial y}\frac{\partial y}{\partial\xi} + \frac{\partial\varphi}{\partial z}\frac{\partial z}{\partial\xi} \\
\frac{\partial\varphi}{\partial\eta} &= \frac{\partial\varphi}{\partial x}\frac{\partial x}{\partial\eta} + \frac{\partial\varphi}{\partial y}\frac{\partial y}{\partial\eta} + \frac{\partial\varphi}{\partial z}\frac{\partial z}{\partial\eta} \\
\frac{\partial\varphi}{\partial\zeta} &= \frac{\partial\varphi}{\partial x}\frac{\partial x}{\partial\zeta} + \frac{\partial\varphi}{\partial y}\frac{\partial y}{\partial\zeta} + \frac{\partial\varphi}{\partial z}\frac{\partial z}{\partial\zeta}
\end{aligned} \tag{2.75}$$

In this way, the values and C_U in the wall coordinate system are able to be computed. Since τ_w from eq.(2.71) is in the $-\xi$ direction in wall coordinate system, τ_w should be separated into x direction component and z direction component so that it can be applied to the boundary condition of the momentum equation in physical coordinate system as follows:

$$\tau_{wx} = \mu \frac{\partial u}{\partial y}\bigg|_{y=0} = \mu \frac{\partial u_\xi \cos\vartheta}{\partial y}\bigg|_{y=0} = \tau_w \cos\vartheta$$
$$\tau_{wz} = \mu \frac{\partial w}{\partial y}\bigg|_{y=0} = \mu \frac{\partial w_\xi \sin\vartheta}{\partial y}\bigg|_{y=0} = \tau_w \sin\vartheta \tag{2.76}$$

In this way, the coordinate transformation between physical coordinate system and the wall coordinate system enables the AWF to be applicable to the three-dimensional computation.

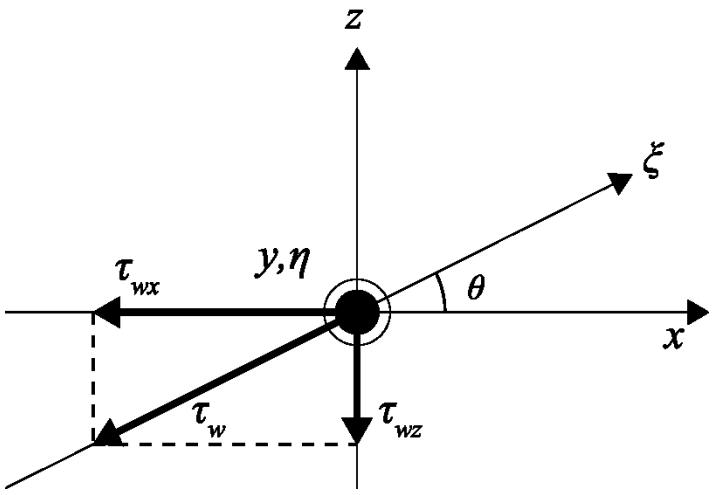

Figure 2.16: Decomposition of wall shear stress τ_w

2.16: Summary (Computational procedure):

The computational schemes employed in this study are mentioned in this chapter. Discretization for the governing equations, LES and AWF, which is the main part of this study, are explained in its detail. Considering the computational geometries, the performance of the LES, computational cost and the required accuracy, the computational schemes are summarized in Table 2.1.

Table 2.1: CFD scheme employed in this study.

CFD scheme	CFD Scheme employed in this study
Space discretization method	Finite Difference Method (FDM)
Time discretization method	Second order Adams-Bashforth method
Pressure solution	Successive-Over Relaxation (SOR) method [39]
Numerical analysis for turbulence	Large Eddy Simulation (LES)
Sub-Grid Scale (SGS) model	Smagorinsky model [40]
Wall model	Analytical Wall Function (AWF) [1]

Chapter 3: The new modeling for LES-AWF

3.1 The importance for deriving the new modeling for LES-AWF

One of the most important elements of LES-AWF (RANS-AWF) is the modeling of the SGS eddy viscosity ν_{SGS} (eddy viscosity ν_t). This is because the SGS eddy viscosity is the only one modeled variable for the LES-AWF, that is the LES-AWF does not apply any major approximations to other variables. Therefore, the performance of the LES-AWF depends mostly on the consistency of the SGS eddy viscosity modeling.

However, there is an inconsistency with the conventional LES-AWF about the SGS eddy viscosity modeling. The new LES-AWF adopts the same way for the SGS eddy viscosity modeling ν_{SGS} as that for the eddy viscosity modeling ν_t regardless of the difference between ν_{SGS} and ν_t. Eddy viscosity ν_t modeling for RANS employs two constant parameters α and y_v^+. Modeling the eddy viscosity ν_t as a fixed linear function is reasonable because the parameters for the RANS simulation are not affected by time step. Since the LES-AWF is an unsteady state simulation, parameters should be also instantaneous parameters so that they can be changed at each time step. As long as using the same constant parameters for the SGS eddy viscosity modeling, the SGS eddy viscosity modeled by the LES-AWF cannot be an instantaneous parameter. This inconsistency should be made clear. Therefore, in this chapter, the new instantaneous modeling for LES-AWF is proposed.

In addition, the SGS eddy viscosity has a great dependence on the grid size, because the SGS models define their length scale by the grid sizes. Hence, a new grid dependent SGS eddy viscosity modeling is also proposed in this study. This new modeling is invented so that the new model can optimize the two parameters α and y_v^+ as a function of the grid size.

3.2 **The model coefficient α and y_v^+:**

As mentioned in Chapter 2, from eq. (2.57), the SGS eddy viscosity in the wall adjacent cell P is modeled for the AWF as follows:

$$\begin{aligned} \nu_{SGS} &= c_\mu \sqrt{k_{SGS}} \Delta \\ &= c_\mu \sqrt{k_{SGS}} c_l y \\ &\cong \alpha \nu y^+ \end{aligned} \tag{3.1}$$

Considering the thickness of a viscous sub-layer as the offset length from the wall, ν_{SGS} is eventually modeled as follows.

$$\nu_{SGS} = \max[0, \alpha\nu(y^+ - y_v^+)] \tag{3.2}$$

The conventional LES-AWF defines the coefficients α and y_v^+ as 0.2295 and 5.86, respectively [11,34]. However, these coefficients are originally determined for the eddy viscosity ν_t in RANS simulation. Since the LES is an unsteady state simulation, ν_{SGS} is instantaneous parameter which is able to be changed at every iteration. Hence, it can be considered that instantaneous parameters should be used for the modeling of ν_{SGS} in order to enhance the accuracy of the conventional LES-AWF. Moreover, ν_t does not have a strong grid dependency, while ν_{SGS} greatly depends on the grid size because ν_{SGS} regards a grid size Δ as its length scale. Therefore, ν_{SGS} modeling for the LES-AWF should be grid dependent, although ν_t modeling for the RANS-AWF is not supposed to be grid dependent.

3.3 **Main points of modification for SGS eddy viscosity modeling**

In summarizing what this study intends to improve the conventional LES-AWF, there are two main points for the modification of SGS eddy viscosity modeling:

1. Grid dependent SGS eddy viscosity modeling (Section 3.5)

   The SGS eddy viscosity is strongly affected by a grid size because of its length scale Δ, which is the grid size. Therefore, the modeling is altered so that it can be different depending on the grid size.

2. Instantaneous SGS eddy viscosity modeling (Section 3.6)

   Since LES is an unsteady state simulation, the SGS eddy viscosity profile changes at every iteration. Hence, the modeling is modified to be instantaneous one in this study so that it can be changed according to the velocity profile at every iteration.

3.4 **The new definition for the model coefficient α**

As mentioned in section 2.14, the conventional LES-AWF is based on the idea of one-equation model for RANS in order to model the SGS eddy viscosity. However, this study employs the Smagorinsky model, which is one of the most common SGS models for the LES. This is because the Smagorinsky model is sensitive to the grid size because it is a turbulence model for the LES and refers to the grid size as its length scale.

As a result, the new modeling of the SGS eddy viscosity is expressed as follows:

$$
\begin{aligned}
\nu_{SGS} &= (C_S\Delta)^2|S| \\
&= C_S\Delta \cdot C_S\Delta|S| \\
&= \beta y \cdot \gamma u_\tau \\
&= \beta\gamma \cdot u_\tau y \\
&= \alpha \cdot \nu \cdot \frac{u_\tau y}{\nu} \\
&= \alpha\nu y^+
\end{aligned}
\tag{3.3}
$$

where the coefficients α, β and γ are defined as:

$$
\begin{aligned}
\alpha &= \beta \cdot \gamma \\
\beta &= \frac{C_S\Delta}{y_p} \\
\gamma &= \frac{C_S\Delta|S|}{u_\tau}
\end{aligned}
\tag{3.4}
$$

and y_p^+ denotes the normalized wall distance of the grid point P (see Fig. 2.12).

In order to fulfill the two main points of modification mentioned in section 3.3, it is necessary to simulate the correlation between grid size, instantaneous velocity profile and the coefficients α, β and γ. In section 3.5, the modification for the grid dependency is explained. In section 3.5, the other modification for dynamic modeling is mentioned.

3.5 **A priori test for deriving grid dependent coefficient $\overline{\alpha}$ and $\overline{y_v^+}$**

A priori tests are required to correlate the coefficients α, β and γ to a grid size. In this case, many different grid sizes must be adopted because these coefficients should be expressed as functions of grid size. From eq.(3.4) the coefficient γ includes the unknown value the GS strain

rate tensor $|S|$, which is the only one unknown value for those coefficients. Hence, a priori test for $|S|$ is needed to make it a function of the grid size.

It is hard to estimate an exactly value of $|S|$ before starting a simulation. Hence a priori test is meaningful for revealing the correlation between $|S|$ and a grid size.

3.5.1 **Computational condition**

A three-dimensional channel is employed for this a priori test because this is one of the simplest geometry and does not have a great effect by the complicated geometry. The details of the computational conditions are shown in Table 3.1. The friction Reynolds number is 790 which is defined by the channel height as the characteristic length and the friction velocity as the characteristic velocity.

$$\mathrm{Re}_\tau = \frac{u_\tau H}{\nu} = 790 \tag{3.5}$$

The domain size is $3H(x) \times H(y) \times 0.75H(z)$. The number of the grid point in the wall normal direction y is 40. The number in the streamwise direction x and the spanwise direction z are dependent on the different grid sizes. The Adams-Bashforth method is adopted for the time marching method. The Adams-Bashforth method is helpful for making the computation more stable by referring to the data at previous time step as well as the time step before the previous time step. The governing equations were discretized by the second order central difference method for the space discretization in order to maintaining the method accurate and yet to make a CFD code simpler.

Table 3.1: Computational condition for the a priori test.

Friction Reynolds number Re_τ	$\mathrm{Re}_\tau = \frac{u_\tau H}{\nu} = 790$
Computational domain	$3H(x) \times H(y) \times 0.75(z)$
Time marching method	2nd order Adams-Bashforth method
Discretization method	2nd order central difference method

3.5.2 **Grid size in near wall region:**

This a priori test intends to reveal the correlation between the grid size and the GS strain tensor $|S|$. Hence, the grid size must be changed and the size has better to be relatively large so that the AWF can use a large grid size in order to avoid an extremely high computational cost caused by a fine mesh in near wall regions. This a priori test treated the grid size in the wall tangential directions (x and z directions) and the wall normal direction (y direction) individually. This is because it can be assumed that the effect of a grid size in the wall normal direction is different from that of the grid size in the wall tangential direction. Therefore, this a priori test tried introducing two different grid size parameters $\left(y_1^+, \sqrt{\Delta x^+ \Delta z^+}\right)$ and making the GS strain tensor $|S|$ profile as a function of these parameters, where y_1^+ is normalized by the first cell height from the wall and $\sqrt{\Delta x^+ \Delta z^+}$ is the geometric mean of the grid width in the wall tangential directions. The range of y_1^+ is $10 \sim 50$ and that of $\sqrt{\Delta x^+ \Delta z^+}$ is $20 \sim 50$ as shown in Table 3.2. In Table 3.2, the case numbers denote the normalized wall distance y_1^+ between the wall and the first grid point. As y_1^+ becomes large, the grid size increases and the mesh becomes coarser which is applicable to the LES-AWF as shown in Fig. 3.1. On the other hand, the case code is correlated to the other grid size parameter, that is grid size in wall tangential direction $\sqrt{\Delta x^+ \Delta z^+}$. As $\sqrt{\Delta x^+ \Delta z^+}$ increases, the mesh is made to be coarser in the wall tangential directions as shown in

Fig. 3.1. Hence, the case 1A represents the finest grid in all the cases, although the mesh is still too coarse to be applied without wall functions. Accordingly, the case 9E is the coarsest one.

Table 3.2: Computational grid for a priori test.

case No.	First grid point normalized wall distance y_1^+	case Code	grid size in wall tangential direction $\sqrt{\Delta x^+ \Delta z^+}$
1	10	A	10
2	15	B	15
3	20	C	20
4	25	D	30
5	30	E	40
6	35		
7	40		
8	45		
9	50		

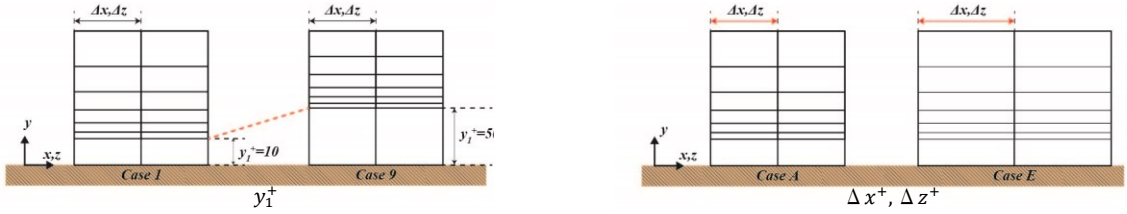

Case 1 $<$ *Case* 2 $<$ …… $<$ *Case* 9 Case A $<$ *Case* B $<$ …… $<$ *Case* E

Figure 3.1: The differences between case numbers and case codes.

3.5.3 **Shumann's boundary condition [30]:**

As mentioned in section 3.5.2, a relatively large grid size is employed. Therefore, a wall function should be adopted for this computation. Shumann's boundary conditions [30] are applied in this a priori test. This boundary conditions directly correlate wall shear stress as the boundary conditions to the velocity in the core region. These boundary conditions are written as follows:

$$\tau_{w,x}(x,z) = \frac{u(x,y_1,z)}{\langle \bar{u}(x,y_1,z) \rangle} \langle \tau_w \rangle \qquad (3.6)$$

$$v_w(x,z) = 0$$

$$\tau_{w,z}(x,z) = \frac{2}{\mathrm{Re}_\tau}\left[\frac{w(x,y_1,z)}{y_1}\right]$$

where, y_1 denotes the first grid point from the wall, $\langle\tau_w\rangle$ mean wall shear stress and $\langle\bar{u}(x,y_1,z)\rangle$ long time averaged value of the mean flow velocity. Whereas the long time averaged value $\langle\bar{u}(x,y_1,z)\rangle$ can be determined by the log law of the wall, and the mean wall shear stress $\langle\tau_w\rangle$ can be obtained from a priori test. For a channel flow, it has the same value as the driving pressure gradient. In this a priori test, the driving pressure gradient is set to 2. Hence, the mean wall shear stress $\langle\tau_w\rangle$ is set to 1 for each wall.

In addition, the Spalding's law of the wall is employed to give the long time averaged value $\langle\bar{u}(x,y_1,z)\rangle$ as the known value before the simulation. Normally, the log law is utilized more often because the first grid point is not inside the buffer layer or viscous sub-layer. Proposing that the velocity u_p is the velocity at first grid point from the wall y_p, the log law is shown as these equations.

$$\begin{aligned} \overline{u_p^+} &= y_p^+ \qquad\qquad \left(y_p^+ < 11.635\right) \\ \overline{u_p^+} &= \frac{1}{\kappa}\ln y_p^+ + B \quad \left(y_p^+ > 11.635\right) \end{aligned} \tag{3.7}$$

where $\kappa = 0.4$ and $B = 5.5$. However, the log law cannot evaluate the velocity profies precisely in a buffer layer. In this a priori test, y_1^+ starts with 10, which is in the range of buffer layer. Hence, the log law is not applicable for this case. Instead, the Spalding's law, which is another wall function and also applicable for buffer layer, is employed. The definition of that wall function is expressed as follows.

$$y_p^+ = \overline{u_p^+} + e^{-\kappa B}\left[exp\left(\kappa\overline{u_p^+}\right) - 1 - \kappa\overline{u_p^+} - \frac{\left(\kappa\overline{u_p^+}\right)^2}{2} - \frac{\left(\kappa\overline{u_p^+}\right)^3}{6}\right] \tag{3.8}$$

The log law and the Spalding's law are compared with each other in Fig. 3.2. As it can be seen in Fig. 3.2, the Spalding's law shows a better agreement in the buffer layer with the result from the

Direct Numerical Simulation (DNS), which is the most accurate CFD method for turbulence predictions. Therefore, it is reasonable to use the Spalding's law in this a priori test.

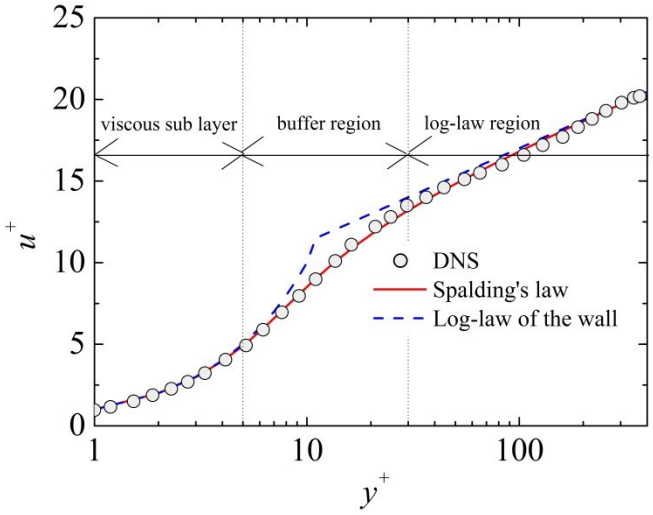

Figure 3.2: Spalding's law

3.5.4 γ profile:

From the a priori test, the relationship between $\overline{|S|}^+$ and grid size y_1^+ and $\sqrt{\Delta x^+ \Delta z^+}$ was revealed. Where $\overline{|S|}^+$ is normalized GS strain rate tensor and it can be normalized by the grid size and the friction velocity;

$$\overline{|S|}^+ = \frac{\overline{|S|}\Delta}{u_\tau} \tag{3.9}$$

Hence, the coefficient γ can be derived as following equation:

$$\gamma = \frac{C_S \Delta |S|}{u_\tau} = C_S \overline{|S|}^+$$

First, the coefficient γ profile is represented in Fig. 3.3.

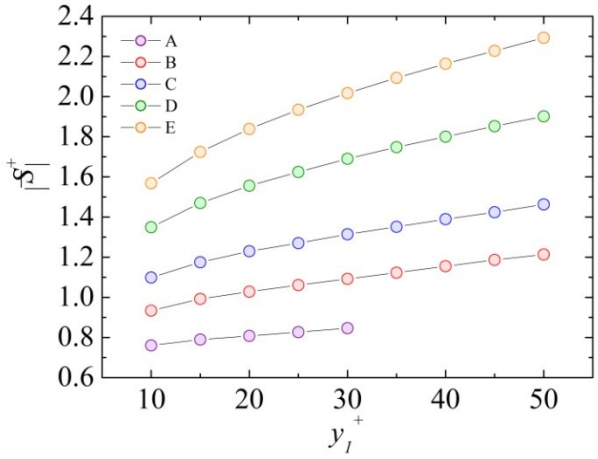

Figure 3.3: γ profile.

In the computations of a priori test for γ profile, cases 6-E to 9-E caused numerical instability because of extremely high aspect ratio. Hence it was concluded from those cases that it is impossible to obtain a priori data. In order to derive the function $\gamma(y_1^+)$, three trend lines are described for each case. After different types of trend lines were obtained it was found that the power law is the most accurate option. Thus, the function $\gamma(y_1^+)$ for all the cases are obtained as follows:

$$\begin{aligned} case\ A: \ \gamma &= 0.610 {y_1^+}^{0.0951} \\ case\ B: \ \gamma &= 0.640 {y_1^+}^{0.160} \\ case\ C: \ \gamma &= 0.730 {y_1^+}^{0.175} \\ case\ D: \ \gamma &= 0.828 {y_1^+}^{0.211} \\ case\ E: \ \gamma &= 0.913 {y_1^+}^{0.234} \end{aligned} \tag{3.10}$$

Second, as seen in Fig. 3.3, γ profile also depends on the grid size in the wall tangential directions $\sqrt{\Delta x^+ \Delta z^+}$. A general equation for eq. (3.10) is given by using two coefficients a_1 and a_2 as:

$$\gamma = a_1 {y_1^+}^{a_2} \tag{3.11}$$

Fig.s 3.4 and 3.5 show the correlation between the two coefficients a_1, a_2 and the grid size in the wall tangential directions $\sqrt{\Delta x^+ \Delta z^+}$. The coefficient a_1 employed power law as its trend line, while a_2 logarithmic function. Both functions of the trend lines are expressed as follows:

$$a_1 = 0.293\sqrt{\Delta x^+ \Delta z^+}^{0.305} \tag{3.12}$$

$$a_2 = 0.0956 \ln \sqrt{\Delta x^+ \Delta z^+} - 0.114 \tag{3.13}$$

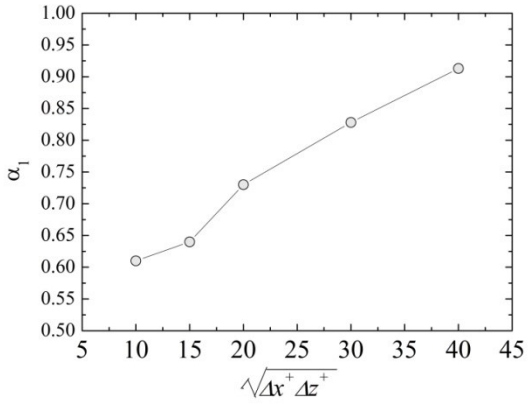

Figure 3.4: a_1 profile.

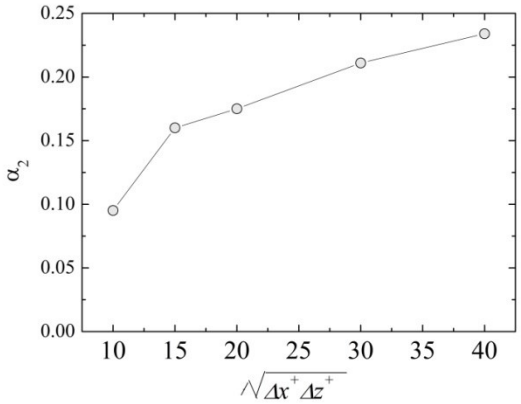

Figure 3.5: a_2 profile.

Finally γ was expressed as the function of the grid sizes y_1^+ and $\sqrt{\Delta x^+ \Delta z^+}$ as follows:

$$\gamma\left(y_1^+, \sqrt{\Delta x^+ \Delta z^+}\right) = 0.293\sqrt{\Delta x^+ \Delta z^+}^{0.305} {y_1^+}^{0.0956 \ln \sqrt{\Delta x^+ \Delta z^+} - 0.114} \tag{3.14}$$

3.5.5 $\boldsymbol{\beta}$ **function:**

From eq. (3.4), the coefficient β is defined as follows:

$$\beta(\Delta, y_p) = \frac{C_S \Delta}{y_p} \tag{3.15}$$

eq. (3.15) includes only known values such as the grid size parameters, Δ, y_p and constant C_S. Hence, it is possible to obtain β before the simulation. In this study, β profiles are shown in Fig. 3.6.

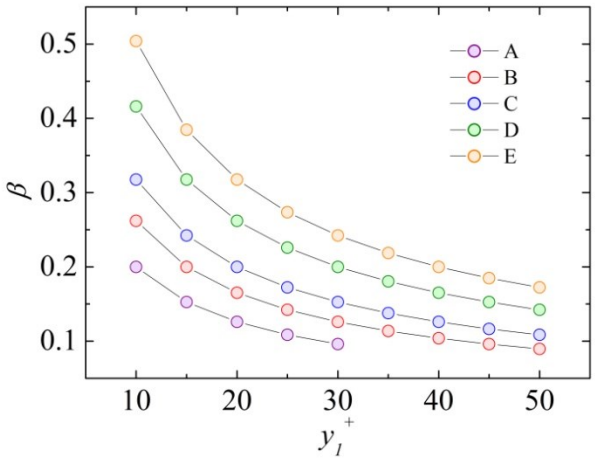

Figure 3.6 β profile.

3.5.6 **Grid dependent $\bar{\alpha}$ function:**

The coefficient α can be defined as the grid dependent function $\bar{\alpha}(\beta,\gamma)$ as (see eq.(3.4)):

$$\begin{aligned}\bar{\alpha}(\beta,\gamma) &= \beta(\Delta, y_p)\cdot\gamma\left(y_1^+, \sqrt{\Delta x^+\Delta z^+}\right)\\ &= \frac{C_S\Delta}{y_p}\cdot a_1 {y_1^+}^{a_2}\\ &= \frac{C_S\sqrt[3]{\Delta x\Delta y\Delta z}}{y_p}\\ &\quad\cdot 0.293\sqrt{\Delta x^+\Delta z^+}^{0.305} {y_1^+}^{0.0956\ln\sqrt{\Delta x^+\Delta z^+}-0.114}\end{aligned} \tag{3.16}$$

3.5.7 **Grid dependent $\overline{y_v^+}$ function:**

The grid dependent normalized thickness of the viscous sub-layer $\overline{y_v^+}$ also should be grid dependent. This is because the slope $\bar{\alpha}$ of the SGS eddy viscosity ν_{SGS} changes depending on the grid size. In this study, $\overline{y_v^+}$ is assumed to be the function of the grid size in the wall tangential directions $\sqrt{\Delta x^+ \Delta z^+}$ as:

$$\overline{y_v^+}\left(\sqrt{\Delta x^+ \Delta z^+}\right) = 0.182\sqrt{\Delta x^+ \Delta z^+} + 1.75 \tag{3.17}$$

3.6 **Instantaneous SGS eddy viscosity modeling:**

In section 3.5, the coefficients α and y_v^+ are made to be grid dependent function $\bar{\alpha}$ and $\overline{y_v^+}$. In this section, the coefficients α and y_v^+ are made to be instantaneous functions so that the SGS eddy viscosity modeling can adjust the different velocity profiles of each iteration.

3.6.1 **Instantaneous coefficient α modelling:**

As mentioned in subsection 3.5.3, Shumann [30] defined the instantaneous wall shear stress τ_w as follows:

$$\tau_{w,x}(x,z) = \frac{u(x,y_1,z)}{\langle \bar{u}(x,y_1,z)\rangle}\langle \tau_w \rangle \tag{3.18}$$

The wall shear stress τ_w became an instantaneous parameter by the ratio of the instantaneous velocity at the first grid point and the mean velocity as the same point. In this study this idea is adopted as an analogy. The coefficient α is assumed that it can be correlated with the GS strain tensor $|S|^+{}_1$ at the first grid point form the wall. From section 3.5, the mean values of the grid dependent $\bar{\alpha}$ and $\overline{y_v^+}$ are obtained. In addition, the mean value of grid dependent $\overline{|S|}^+$ is also determined by a priori test for γ function. Therefore, the ratio of instantaneous α and averaged $\bar{\alpha}$

can be correlated to the ratio of instantaneous $|S|^+_1$ and $\overline{|S|}^+$. The instantaneous α can be derived as follows:

$$\alpha = \frac{|S|^+_1}{\overline{|S|}^+}\bar{\alpha} \tag{3.19}$$

3.6.2 **Instantaneous coefficient y_v^+ modelling:**

In the same way as the case of the instantaneous coefficient α modeling, y_v^+ also made to be the instantaneous parameter by the ratio of the instantaneous friction velocity $\widetilde{u_\tau}$ and the averaged wall shear stress $\overline{u_\tau}$.

$$y_v^+ = \sqrt{\frac{\overline{u_\tau}}{\widetilde{u_\tau}}}\overline{y_v} \tag{3.20}$$

where, $\overline{\tau_w}$ is the mean wall shear stress. In this a priori test, $\overline{\tau_w}$ can be determined by the driving pressure gradient. The mean driving pressure gradient is set to 2 in this study. Hence, the top wall and bottom wall has the same mean wall shear stress 1 so that they both can be in balance.

The instantaneous friction velocity is determined by the instantaneous wall shear stress $\widetilde{\tau_w}$. From the definition of the wall shear stress, the instantaneous wall shear stress $\widetilde{\tau_w}$ is expressed as follows:

$$\widetilde{\tau_w} = \rho\widetilde{u_\tau}^2 \tag{3.21}$$

In order to obtain the instantaneous wall shear stress $\widetilde{\tau_w}$, the mass and momentum conservation in wall adjacent cells are referred. Fig. 3.6 shows a wall adjacent cell where it is possible to consider the mass and momentum conservations.

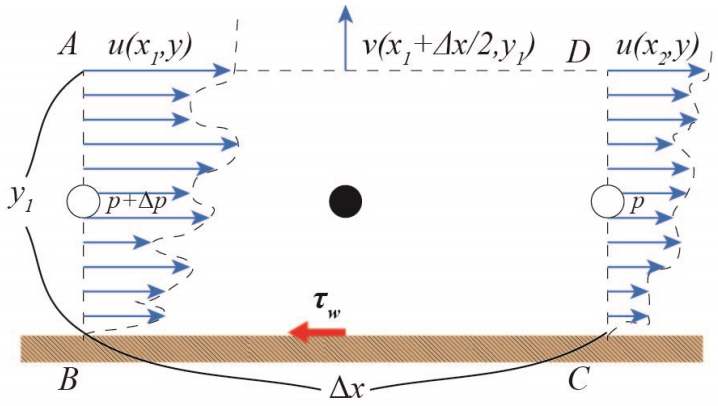

Figure 3.7 Mass and momentum conservations in wall adjacent cells.

First, the mass conservation can be considered in the square region ABCD which has the height y_1 and the length Δx. Assuming that the width of this region is Δz, the volume of this region is $V = \Delta x \Delta z \Delta y_1$ and the mass inside this region can be expressed as follows:

$$m = \rho \Delta x \Delta z y_1 \tag{3.22}$$

The mass flow rates q_1, q_2 and q_3 of these surfaces are expressed as:

$$AB: \rho \Delta z \int_0^{y_1} u(x_1, y) dy = q_1$$

$$AD: -\rho \Delta z \int_{x_1}^{x_1 + \Delta x/2} v(x, y_1) dx = -q_2 \tag{3.23}$$

$$CD: -\rho \Delta z \int_0^{y_1} u(x_2, y) dy = -q_3$$

These mass flow rates have been balanced by the mass conservation.

$$\frac{dm}{dt} = q_1 - q_2 - q_3 = 0 \tag{3.24}$$

Solving for q_2 and substituting the equations of q_1 and q_3 in eq.(3.24), q_2 can be expressed as follows:

$$q_2 = q_1 - q_3 = \rho\Delta z\left(\int_0^{y_1} u(x_1, y)dy - \int_0^{y_1} u(x_2, y)dy\right) \tag{3.25}$$

Second, the momentum conservation can be considered in this region. The fluid inside the region has momentum M_x, which is written as follows:

$$M_x = \rho\Delta z \int_0^{\Delta x}\left(\int_0^{y_1} u(x, y)dy\right)dx \tag{3.26}$$

The momentums $Q_1, Q_2,$ and Q_3 which flow into or out from the region per unit time on each surface are expressed as Follows:

$$\begin{aligned} AB &: \rho\Delta z \int_0^{y_1} u(x_1, y)^2 dy = Q_1 \\ AD &: -q_2 \int_{x_1}^{x_2} u(x, y_1)dx = -Q_2 \\ CD &: -\rho\Delta z \int_0^{y_1} u(x_2, y)^2 dy = -Q_3 \end{aligned} \tag{3.27}$$

Assuming that D is the force imposed on the wall from $x = x_1$ to $x = x_2$, the force imposed on the fluid in the region is $-D$. The time variant of the momentum can be expressed by the sum of the momentum per unit time and the forces as:

$$\begin{aligned} \frac{dM_x}{dt} = \mathrm{Q}_1 - \mathrm{Q}_2 - \mathrm{Q}_3 - D - \Delta\mathrm{p}\Delta\mathrm{z}\mathrm{y}_1 \\ + (\nu + \nu_{\mathrm{SGS}})\frac{\partial u}{\partial y}\Big|_{y=y_1}\Delta\mathrm{x}\Delta\mathrm{z} \end{aligned} \tag{3.28}$$

Hence, $D(L)$ can be obtained by the following equation:

$$D = \mathrm{Q}_1 - \mathrm{Q}_2 - \mathrm{Q}_3 - \Delta\mathrm{p}\Delta\mathrm{zy}_1 + (\nu + \nu_{\mathrm{SGS}})\left.\frac{\partial u}{\partial y}\right|_{y=y_1} \Delta\mathrm{x}\Delta\mathrm{z} \qquad (3.29)$$

As a result, the instantaneous wall shear stress can be defined by the following equation:

$$\begin{aligned}
\widetilde{\tau_w(x)} &= \frac{D}{\Delta x \Delta z} \\
&= \frac{1}{\Delta x \Delta z}\Bigg(Q_1 - Q_2 - Q_3 - \Delta p \Delta z y_1 \\
&\qquad + (\nu + \nu_{SGS})\left.\frac{\partial u}{\partial y}\right|_{y=y_1}\Bigg) \\
&= \frac{\rho}{\Delta x}\Bigg[\left(\int_0^{y_1} u(x_1, y)^2 - u(x_2, y)^2 dy\right) \\
&\qquad - \left(\int_0^{y_1} u\left(x_{1\frac{1}{\Delta x \Delta z}}, y\right) dy - \int_0^{y_1} u(x_2, y) dy\right)\Bigg] \\
&\qquad - \frac{\Delta p}{\Delta x} y_1 + (\nu + \nu_{SGS})\left.\frac{\partial u}{\partial y}\right|_{y=y_1}
\end{aligned} \qquad (3.30)$$

In this way, instantaneous wall shear stress can be derived and from the eqs. (3.21) and (3.22), the instantaneous y_v^+ can be also obtained.

3.7 Summary (the new SGS eddy viscosity modeling):

In this chapter, the new SGS modeling is proposed. Since the SGS eddy viscosity has a strong dependence on the grid size and changes at every iteration depending on different velocity field, a grid dependent and instantaneous new modeling is proposed for the new LES-AWF.

Grid dependent SGS eddy viscosity modeling is given by:

$$\bar{\alpha}(\beta,\gamma)$$

$$= \frac{C_S \sqrt[3]{\Delta x \Delta y \Delta z}}{y_p} \cdot 0.293 \sqrt{\Delta x^+ \Delta z^+}^{0.305} y_1^{+\,0.0956 \ln \sqrt{\Delta x^+ \Delta z^+} - 0.114} \tag{3.31}$$

$$\overline{y_v^+}\left(\sqrt{\Delta x^+ \Delta z^+}\right) = 0.182\sqrt{\Delta x^+ \Delta z^+} + 1.75 \tag{3.32}$$

And the instantaneous SGS eddy viscosity modeling is given as:

$$\alpha = \frac{|S|^+_1}{\overline{|S|}^+} \bar{\alpha} \tag{3.33}$$

$$y_v^+ = \sqrt{\frac{\overline{u_\tau}}{\widetilde{u_\tau}}}\, \overline{y_v^+} \tag{3.34}$$

CHAPTER 4: Results and Discussion

4.1 **Three-dimensional channel flow:**

4.1.1 **Computational geometry:**

The computational geometry and coordinate system are shown in Fig. 4.1. . This study adopted a non-uniform structured mesh in the y direction and a uniform structured mesh in the other directions (x and z). The number of grid points is shown in Table 4.1. As shown in Table 4.1, two different friction Reynolds numbers are employed; 395 and 790. The first grid point is set at within $y_1^+ = 1$ from the wall for the cases of the Wall-resolved LES (without AWF) in order to hold the accuracy. On the other hand, the distance between first grid point and the wall for LES-AWF cases are in the range of $y_1^+ = 10$ to 50. The grid dependency was evaluated by using the mean velocity profile in the case of $\mathrm{Re}_\tau = 790$. The result is shown in Fig. 4.3.

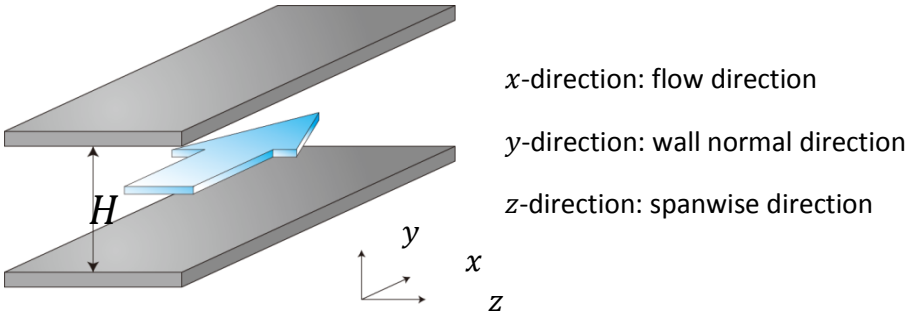

Figure 4.1: Three-dimensional channel.

All cases used for both of Wall-resolved LES and LES-AWF are distinguished by the three characters as shown in Tables 4.1 and 4.2. The first character L and H

represents the lower friction Reynolds number 360 and the higher friction Reynolds number 790, respectively. The second character, that is the number from 1 to 3, denotes the difference of the normalized wall distance between the wall and the first grid point. As the number increases, y_1^+ will increase correspondingly. The number 1 denotes the minimum value $y_1^+ = 10$ and the number 10 the maximum value 50. The change of y_1^+ according to the case number is described in Fig. 4.2. The last character, by the symbol from A to E, indicates the difference of grid size in wall tangential directions (x and z). The character A is the case where the minimum normalized wall tangential grid size $\sqrt{\Delta x^+ \Delta z^+}$ is applied, and E is the case where the maximum normalized wall tangential grid size $\sqrt{\Delta x^+ \Delta z^+}$ is employed. The $\sqrt{\Delta x^+ \Delta z^+}$ variation is illustrated in Fig. 4.2.

Table 4.1: Computational grid for LES-AWF.

Re_τ	Case No.	Δx^+	Δz^+	$N_X \times N_y \times N_z$	$\sqrt{\Delta x^+ \Delta z^+}$	y_1^+
390	L-1-A	20	5	$15 \times 20 \times 15$	10	10
	L-2-A					30
	L-1-B	40	10	$30 \times 20 \times 30$	20	10
	L-2-B					30
	L-3-B					50
	L-1-C	80	20	$60 \times 20 \times 60$	40	10
	L-2-C					40
	L-3-C					50
790	H-1-A	20	5	$30 \times 22 \times 30$	10	10
	H-2-A					30
	H-1-B	40	10	$60 \times 22 \times 60$	20	10
	H-2-B					30
	H-3-B					50
	H-1-C	80	20	$120 \times 20 \times 120$	40	10
	H-2-C					40
	H-3-C					50

Table 4.2: Computational grid for Wall-resolved LES.

Re_τ	Case No.	Δx^+	Δz^+	$N_X \times N_y \times N_z$	$\sqrt{\Delta x^+ \Delta z^+}$	y_1^+
390	L-1-A	20	5	$15 \times 50 \times 15$	10	0.5
	L-2-A					
	L-1-B	40	10	$30 \times 50 \times 30$	20	
	L-2-B					
	L-3-B					
	L-1-C	80	20	$60 \times 50 \times 60$	40	
	L-2-C					
	L-3-C					
790	H-1-A	20	5	$30 \times 60 \times 30$	10	
	H-2-A					
	H-1-B	40	10	$60 \times 60 \times 60$	20	
	H-2-B					
	H-3-B					
	H-1-C	80	20	$120 \times 60 \times 120$	40	
	H-2-C					
	H-3-C					

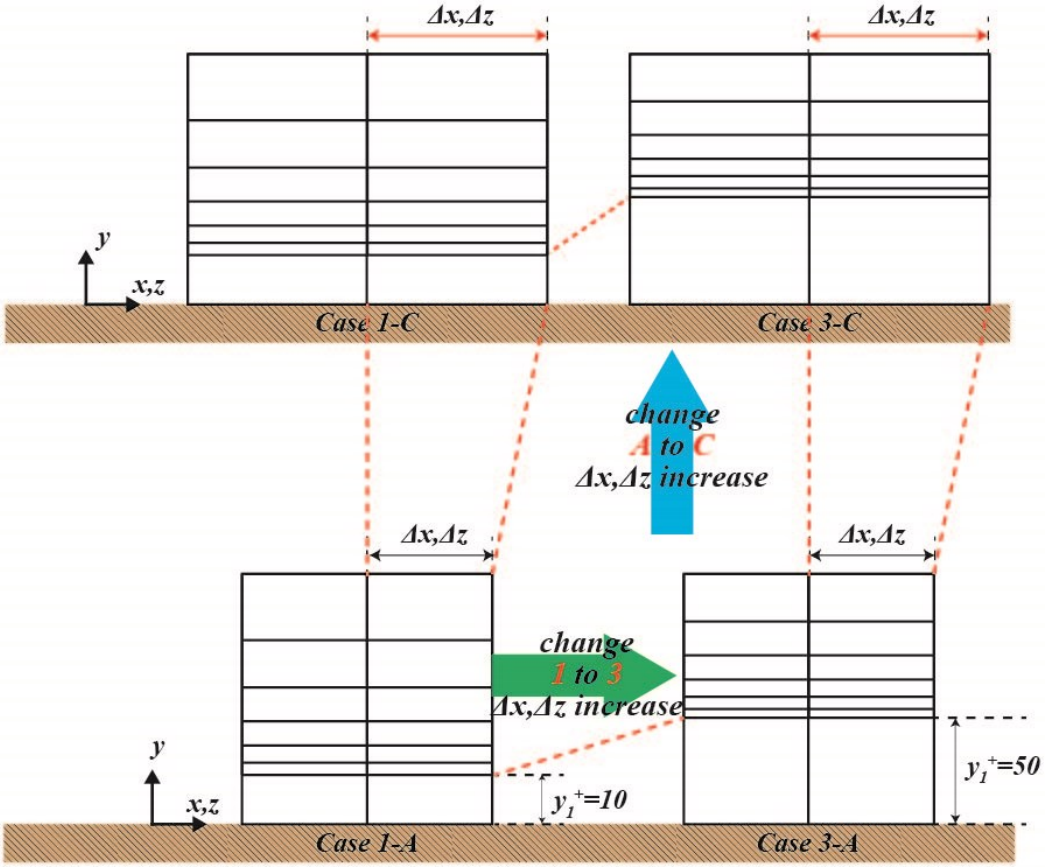

Figure 4.2: Different grid sizes for LES-AWF.

Table 4.3: Computational grid for grid dependency test.

Re_τ	CFD method	$N_X \times N_y \times N_z$	Δx^+	Δz^+	$\Delta {y_{max}}^+$
360	DNS	$128 \times 129 \times 128$	17.7	5.9	4.4
	LES	$60 \times 50 \times 60$	20	5	17
790	DNS	$256 \times 193 \times 192$	10	6.5	6.5
	LES	$120 \times 60 \times 120$	20	5	40

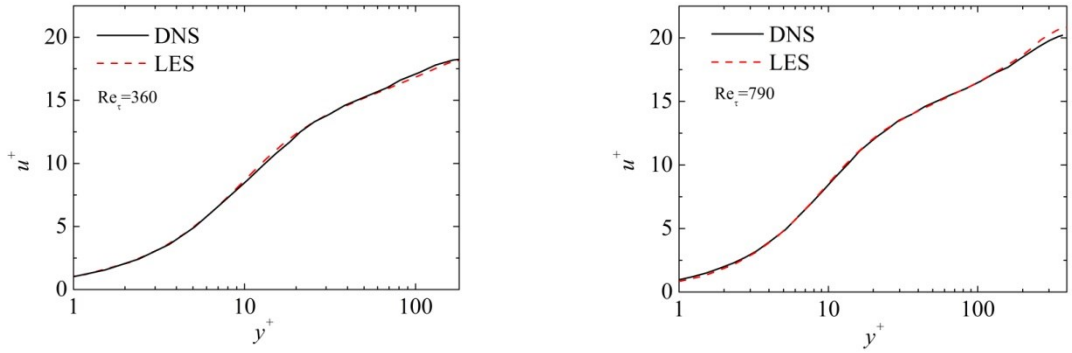

(a) $\mathrm{Re}_\tau = 360$ (b) $\mathrm{Re}_\tau = 790$

Figure 4.3: Grid dependency test

Case No.	Wall-resolved LES	LES-AWF
H-3-C	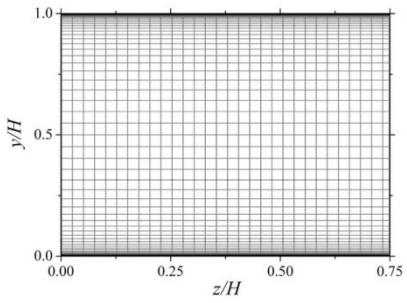	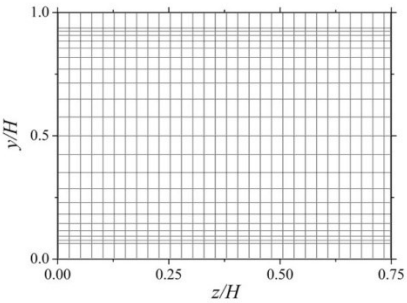

Figure 4.4: Computational grid for three-dimensional channel

Basically, there is a small difference between the DNS with a dense grid and the LES with a relatively less dense mesh as shown in Fig. 4.4. Hence, this study employed grid size $\Delta {y_{max}}^+$ shown in Table 4.3 for the Wall-resolved LES cases. As shown in Fig. 4.2, since the grid size in the wall tangential direction Δx^+ or Δz^+, and the first layer thickness y_1^+ are different between cases, the Wall-resolved LES cases fix these three

grid size parameters Δx^+, Δz^+ and y_1^+. However, ${\Delta y_{max}}^+$ can be fixed to be the same value to all cases. Therefore, the Wall-resolved LES defines ${\Delta y_{max}}^+$ as 28, which is revealed to be small enough to obtain as an accurate velocity profile as the DNS as depicted in Fig. 4.3. In summary, the case of the Wall-resolved LES defines a grid size in the wall normal direction as $\Delta y^+ = 0.8{\sim}17$ for a lower friction Reynolds number $\mathrm{Re}_\tau = 360$ and $\Delta y^+ = 0.8{\sim}40$ for a higher friction Reynolds number.

4.1.2 **Mean velocity:**

4.1.2.1 **The case of $\mathbf{Re_\tau = 790}$:**

Figure 4.5 shows all the cases of the mean velocity profile in the wall normal direction y. The non-dimensional distance y^+ is the wall distance normalized by friction velocity u_τ. The Static LES-AWF, which adopts the constant parameters α and y_v^+, is shown with a black dashed lines, while the Dynamic LES-AWF, which employs the functional parameters α and y_v^+, is shown with red solid lines. In addition, the symbols illustrate the computed results from the Wall-resolved LES without AWF. Since these results of the LES without AWF are obtained by arranging a denser mesh in the near wall region instead of employing the AWF, these results should be the most reliable results among these three lines. As seen in Fig. 4.5, in most cases, the computations with the and Dynamic LES-AWF show better agreement with the Wall-resolved LES computations than employing the Static LES-AWF. Particularly, the cases (d) H2A, (e) H2B, (f) H2C and (h) H3C show significant improvements. It can be said that the instantaneous parameters enhanced the accuracy in those cases.

Dynamic LES-AWF is not so strongly affected by the grid resolution in the near wall region as the Static LES-AWF. Hence, it is revealed that the grid dependent modeling for these coefficients contribute to preventing the accuracy from being deteriorated by coarse meshes. Unlike the Static LES-AWF, the Dynamic LES-AWF performs better with various grid sizes. This is because the functional α and y_v^+ can adjust their values accordingly to the different grid resolution in near wall region, while constant α and y_v^+ cannot. This diffrence of these two LES-AWF's performances cause this improvement.

Figures 4.5 (a), (b) and (c) show a relatively smaller difference between the Static LES-AWF and the Dynamic LES-AWF. This means that the effect of the new modeling for ν_{SGS} is less remarkable in the cases of (a) H1A, (b) H1B and (c) H1C. Focusing on a point in common between both LES-AWFs, small improvement of the mean velocity flow prediction can be explained. These three cases all have the smallest y_1^+. These are shown in Figs. 4.5 (a), (b) and (c).

As mentioned in section 2.14, the boundary condition on the wall is expressed as this:

$$\frac{\tau_w}{\rho} = \nu \left.\frac{\partial \langle u \rangle}{\partial y}\right|_{y=0} = \nu \frac{u_\tau}{\nu} \left.\frac{\partial \langle u \rangle}{\partial y^+}\right|_{y^+=0} = \frac{u_\tau A_U}{\nu} \tag{4.1}$$

The constant A_U is defined as this from eqs.(2.63) and (2.68):

$$A_U = \frac{\nu \langle u_n \rangle - \frac{1}{2} C_U {y_n}^{+^2}}{{y_n}^{+^2}} \quad (y_1^+ < y_v^+) \tag{4.2}$$

$$A_U{}' = \frac{\alpha\nu\langle u_n\rangle - C_U({y_n}^+ - {y_v}^+) + \frac{C_U(1-\alpha{y_v}^+)}{\alpha}\ln Y^+ - \frac{\alpha}{2}C_U{{y_v}^+}^2}{\alpha{y_v}^+ + \ln Y^+} \quad (4.3)$$

$$(y_1^+ < y_v^+)$$

These three cases has the smallest $y_1^+ = 10$ but the first prid point for the mean velocity u is placed around $y^+ = 5$ because of the shifted staggered placement for u velocity. Hence, it is more likely that eq.(4.2) is utilized for deriving the wall boundary condition. However, eq.(4.2) does not include two new model functions α and y_v^+, while eq.(4.3) includes. Therefore, it is difficult to correlate directly the wall boundary condition and the new two functional parameters α and y_v^+. As a result, the improvement by the new functional parameters α and y_v^+ is not significant. On the contrary, since other cases set the first grid point outside the viscous sublayer, eq.(4.3) is applied for determining the constant A_U for the boundary condition (eq.(4.2)). Hence, the difference between Static LES-AWF and the Dynamic LES-AWF becomes obvious. Functional α and y_v^+ constants directly affect the boundary condition by eq.(4.3). Thus, the improvement in the cases except (a) H1A, (b) H1B and (c) H1C is prominent.

In Figs.4.5 (d), (e), (f) and (h), the Static LES-AWF and Dynamic LES-AWF showed better correspondence with the Wall-resolved LES. This improvement is the contribution of the new modeling of α and y_v^+. The modeling is mostly based on the GS strain tensor $|\bar{S}|$. Since $|\bar{S}|$ is a GS flow parameter, $|\bar{S}|$ is still relatively more reliable in a coarse mesh than the SGS flow parameters. The SGS flow parameters depend on the performance of SGS models, while GS flow parameters including $|\bar{S}|$ is directly resolved

by mesh, although mesh is coarse. Therefore, α and y_v^+ adjust their optimal value in accordance with grid size and instantaneous velocity field, resulting in the enhancement of the accuracy of wall boundary condition from eq.(4.1).

Figure 4.5 (g) clearly presents a discrepancy between the Static LES-AWF and the Dynamic LES-AWF and the Wall-resolved LES. The reason why the case H3A is missing is that the numerical instability happened because of the high aspect ratio of the grid. The grid size Δy is 5 times larger than grid size $\sqrt{\Delta x^+ \Delta z^+}$. The numerical instability does not happen in the case of (g) H3B but the wall normal grid size y_1^+ is still 2.5 times larger than $\sqrt{\Delta x^+ \Delta z^+}$. The case (c) H1C does not have the numerical instability but the wall tangential grid size is 4 times larger than the wall normal grid size y_1^+. Therefore, the Static LES-AWF and the Dynamic LES-AWF has inconsistency with Wall-resolved LES in both of two cases (c) H1C and (g) H3B.

These are shown in Fig. 4.5 (c) and (g).

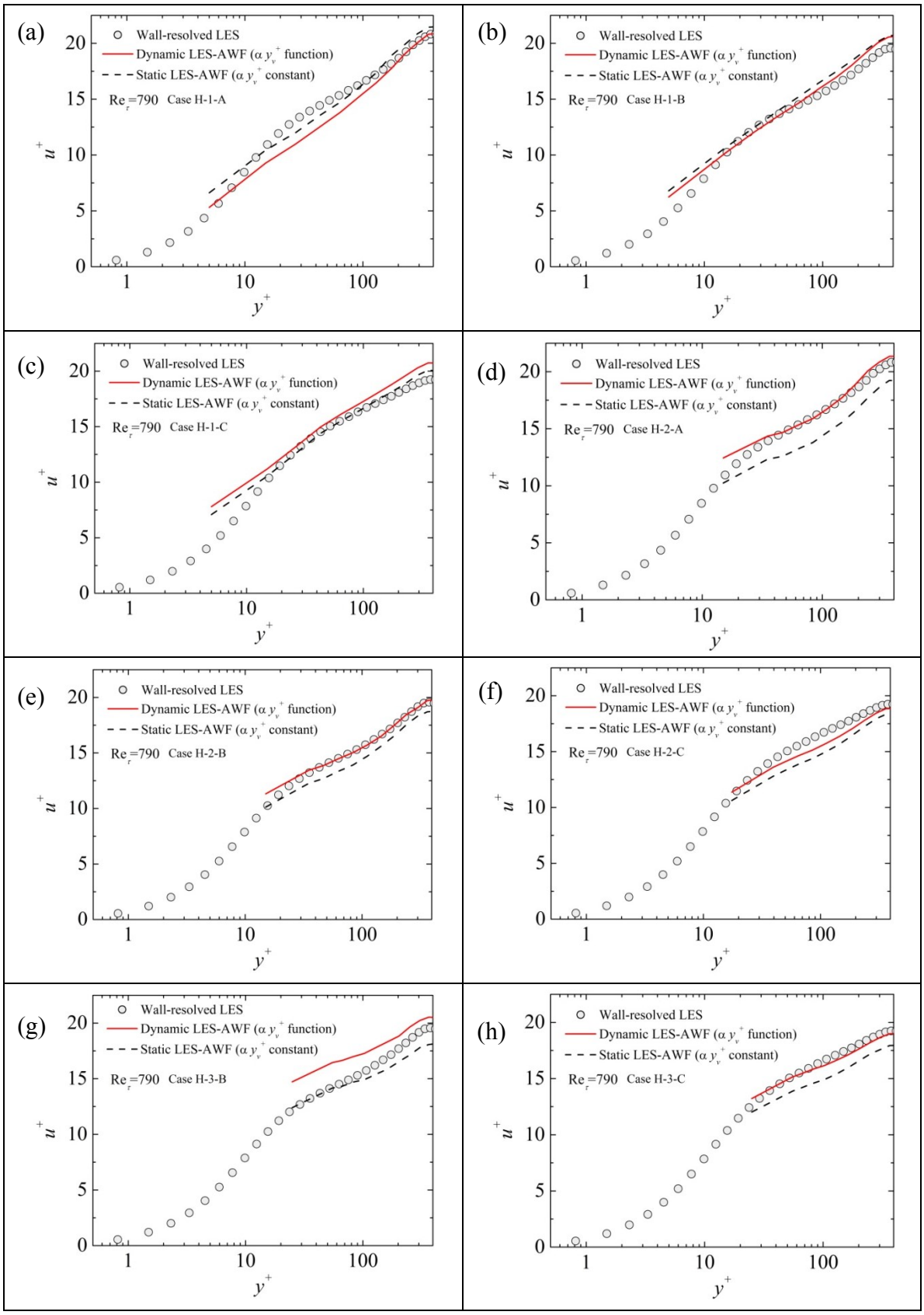

Figure 4.5: Mean velocity profile ($\mathrm{Re}_\tau = 790$)

4.1.2.2 **The case of $\mathbf{Re_\tau = 360}$:**

Figure 4.8 illustrates the mean velocity profiles in the wall normal direction for cases of $\mathrm{Re}_\tau = 360$. The wall distance y and the mean velocity u are normalized by the friction velocity u_τ in the same way as the case of $\mathrm{Re}_\tau = 790$ discussed in subsection 4.1.2.1. The results shown by red solid lines are obtained by the Dynamic LES-AWF, while the results shown by black dot lines are obtained by the Static LES-AWF. The symbols illustrate the results from the computations by the Wall-resolved LES, which employed denser mesh in the near wall region instead of using AWF.

The cases (d) L2A, (e) L2B and (g) L3B show better agreements with Wall-resolved LES results. This can be considered as the contribution of the new modeling for the two parameters α and y_v^+. Whereas these parameters are not able to be changed depending on the grid size in the wall vicinity in the case of the Static LES-AWF, they are able to be altered to the optimal values for the different grid sizes in the cases where the Dynamic LES-AWF is applicable. From the results of the cases of (d) L2A, (e) L2B and (g) L3B, it can be said that the new modeling performs well for optimizing these parameters.

The cases of (a) L1A, (b) L1B and (c) L1C include small differences between the two different LES-AWFs. It appears that, since the first grid point is closer to the wall compared with the other cases, the effect of AWF becomes less remarkable. The grid scale also becomes smaller as the first grid point approaches the wall. Hence, GS components are more predominant over SGS components, which makes the new the modeling of SGS eddy viscosity ineffective. This is explained in the following way.

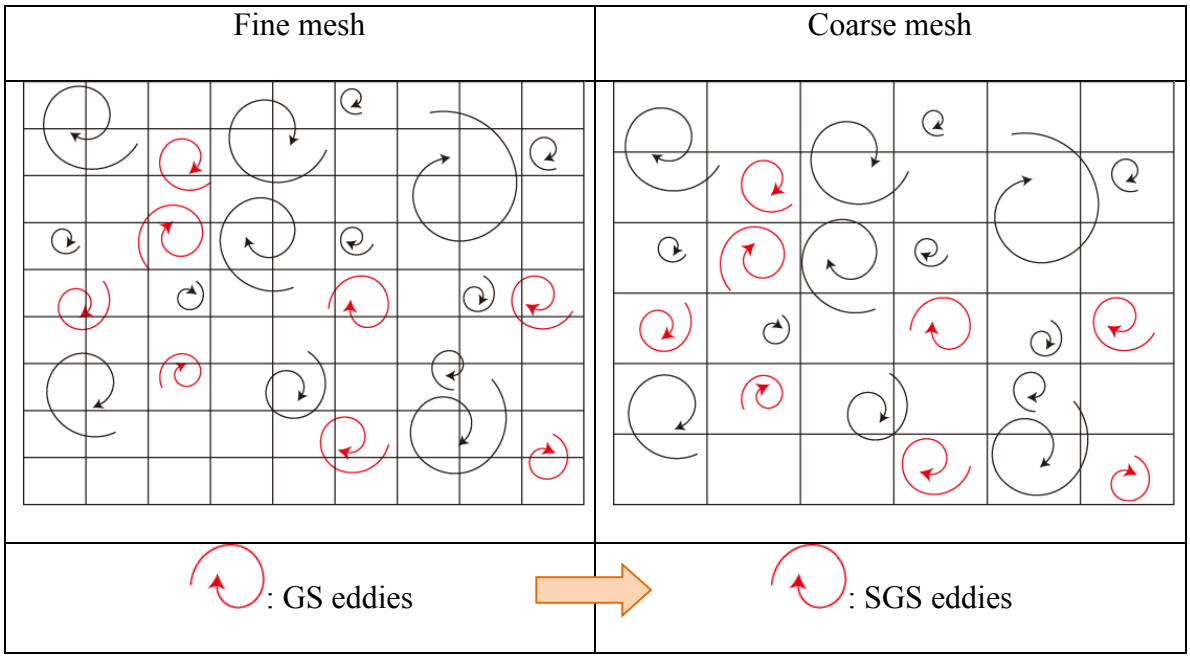

Figure 4.6: Grid dependency of LES.

Fig. 4.6 describes why fine mesh makes GS flow parameters predominant over SGS flow parameters. As seen in Fig. 4.6, red eddies are large enough to be resolved by fine mesh but they are not in coarse mesh. In other words, red eddies are GS eddies in fine mesh, while they are SGS eddies in coarse mesh. Hence, fine mesh has more wide range of eddies than coarse mesh which can be resolved by mesh, which makes GS flow parameters have more controls turbulence field.

This fact that GS flow parameters can be predominant in fine mesh can be explained by the definition of SGS eddy viscosity ν_{SGS}. From eq.(2.50), SGS eddy viscosity ν_{SGS} is defined as this:

$$\nu_{SGS} = (C_S\Delta)^2\left|S_{ij}\right| \tag{4.4}$$

As seen in eq.(4.4), most of the SGS eddy viscosity model such as Smagorinsky model [40] employs grid size Δ as the length scale for ν_{SGS}. When the fine mesh is

adopted, the grid size Δ bocomes smaller. Hence, ν_{SGS} also decreases by the effect of the length scale Δ. Therefore, GS flow parameters relatively has stroger effects over SGS flow parameters. In this way, the new modeling for SGS eddy viscosity ν_{SGS} is made to be less effective.

The other cases with (e) L2C and (f) L3C underestimate the mean velocity in both of the two LES-AWF cases. It is assumed that this is caused by the very coarse mesh in the wall tangential directions. As shown in Table 4.1, these cases set grid width Δx and Δz as 80 and 20, respectively. Hence, even the Wall-resolved LES case predicted mean velocity profile less accurately than the other cases such as (a) L1A. The mean velocity profiles of the Wall-resolved LES case are compared in Fig. 4.7. As it can be seen in Fig. 4.7, the mean velocity profile tends to be overestimated in core region when the grid sizes Δx and Δz become in the wall tangential direction larger. From these results, it can be said that the discrepancy in the cases of (e) L2C and (f) L3C is caused because the Wall-resolved LES case also overestimates the mean velocity profiles.

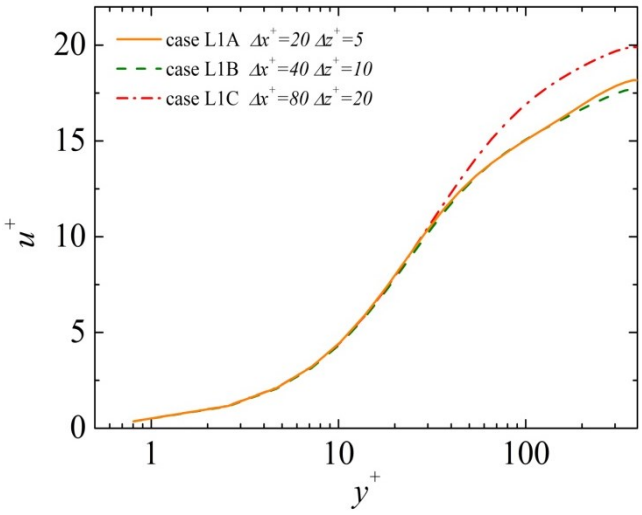

Figure 4.7: wall tangential grid size effect on Wall-resolved LES

However, although there are some cases where the enhancement of the the LES-AWF performance is not obtained, it proved that the grid dependence and dynamic models of the SGS eddy viscosity improves the LES-AWF accuracy.

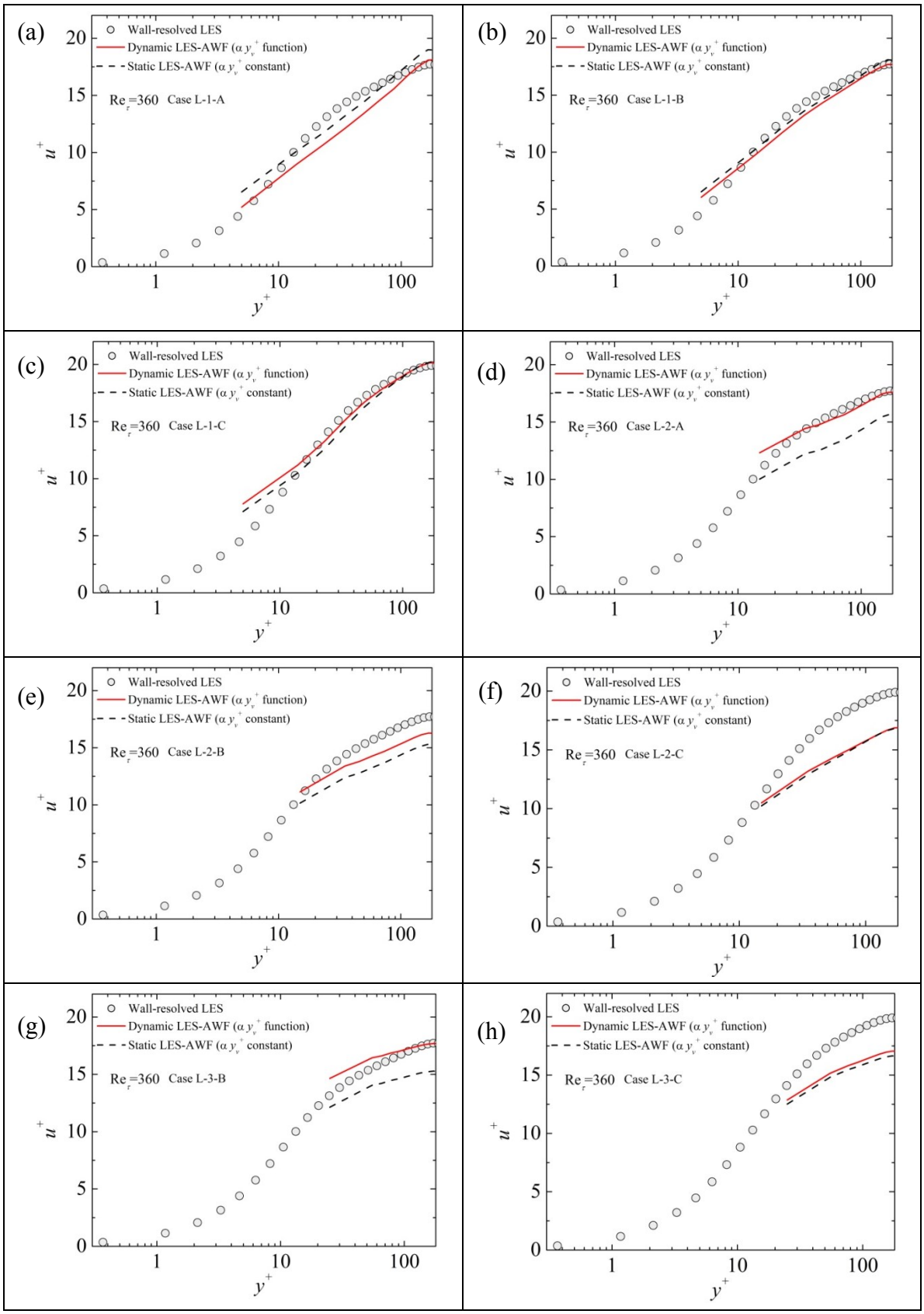

Figure 4.8: Mean velocity profile ($\mathrm{Re}_\tau = 360$).

4.1.3 **Reynolds stresses:**

4.1.3.1 **The case of $\mathbf{Re_\tau = 790}$:**

Figs 4.10, 4.11 and 4.12 illustrate the Reynolds normal stresses $\sqrt{\overline{uu}}^{'+}$, $\sqrt{\overline{vv}}^{'+}$ and $\sqrt{\overline{ww}}^{'+}$, respectively. The wall distance and the Reynolds stresses are normalized by friction velocity. Of the normal components $\sqrt{\overline{uu}}^{'+}$, $\sqrt{\overline{vv}}^{'+}$ and $\sqrt{\overline{ww}}^{'+}$, the $\sqrt{\overline{uu}}^{'+}$ component of the Reynolds stresses shows the most remarkable improvements in some cases. The cases (b) H1B, (d) H2A, (e) H2B, (g) H3B and (h) H3C illustrate better agreement with the Dynamic LES-AWF than the Static LES-AWF. Especially, the results from the Dynamic LES-AWF have closer value to the results of the Wall-resolved LES at the first grid points. Since the first grid point values are strongly affected by LES-AWF, the new modeling of LES-AWF can be considered to contribute to this improvement. More specifically speaking, the definition of Reynolds stresses includes the SGS eddy viscosity (eq. (2.42)). Furthermore, the definition of the SGS eddy viscosity (eq. (2.50)) is determined by the grid width and the GS strain rate tensors, which are composed of the velocity gradients. Hence, the and Dynamic LES-AWF provides a more accurate velocity gradient at the first grid point than the Static LES-AWF, resulting in the improvement of the $\sqrt{\overline{uu}}^{'+}$ prediction.

On the other hand, the other Reynolds normal stresses $\sqrt{\overline{vv}}^{'+}$ and $\sqrt{\overline{ww}}^{'+}$ do not show large differences between the Static LES-AWF and the Dynamic LES-AWF. In the Figs. 4.11 (d) to (h) and Figs. 4.12 (d) to (h), the results show the overestimated levels in the Reynolds stresses at the first grid point, which is a peak at the first grid point. This

can be considered to be caused by the lack of anisotropy in near wall regions. This study employed the regular Smagorinsky model as the SGS model, which is an isotropic model. Normally, the flows are isotropic in near wall regions. The GS Reynolds stresses can detect an anisotropy phenomena by the computational mesh, while the SGS Reynolds stresses cannot. As long as an enough fine mesh is arranged in the near wall region, the SGS components will not be predominant. Hence, the lack of anisotropy for the SGS components of the Reynolds stresses is not so remarkable. However, in this study, a coarse mesh is adopted for the both of LES-AWFs. Of all cases, the first grid cell height for cases of B and C is much larger than that for case A; that is, case B or C have a coarser mesh in the near wall region. Therefore, this lack of anisotropy becomes predominant and a critical issue in these cases where coarser meshes are employed. These SGS components $\sqrt{\overline{vv}}^{\prime+}$ and $\sqrt{\overline{ww}}^{\prime+}$ should be smaller by the anisotropic SGS models. This would improve the results for the Reynolds stresses $\sqrt{\overline{vv}}^{\prime+}$ and $\sqrt{\overline{ww}}^{\prime+}$.

Equation (4.5) shows an anisotropic SGS model proposed by Abe [42] as an example of an anisotropic SGS eddy viscosity model.

$$\tau_{ij} = \langle \widetilde{u_i}\widetilde{u_j} \rangle = \frac{2}{3}\delta_{ij}k_{SGS} - 2\nu_{SGS}\left(\frac{\partial\langle u_i\rangle}{\partial x_j} + \frac{\partial\langle u_j\rangle}{\partial x_i}\right) + R'_{ij} \qquad (4.5)$$

As shown in eq.(4.5), the anisotropic term R'_{ij} is added into the definition. This anisotropic term R'_{ij} profile is shown in Fig.4.9. As shown in Fig. 4.9, only R'_{11} component is positive and other components R'_{22} and R'_{33} are negative. Hence, this term R'_{ij} performs for increasing $\sqrt{\overline{uu}}^{\prime+}$ and instead decreasing $\sqrt{\overline{vv}}^{\prime+}$ and $\sqrt{\overline{ww}}^{\prime+}$ especially in near wall region. Since Fig, 4.10 shows underestimated $\sqrt{\overline{uu}}^{\prime+}$ and on the contrary to this,

Figs. 4.11 and 4.12 described overestimated $\sqrt{vv}^{'+}$ and $\sqrt{ww}^{'+}$ in near wall region, introducing the term R'_{ij} would work for increasing underestimated $\sqrt{uu}^{'+}$ in Fig, 4.10, and on the contrary to this, decreasing overestimated $\sqrt{vv}^{'+}$ and $\sqrt{ww}^{'+}$ at the first grid point in Figs. 4.11 and 4.12.

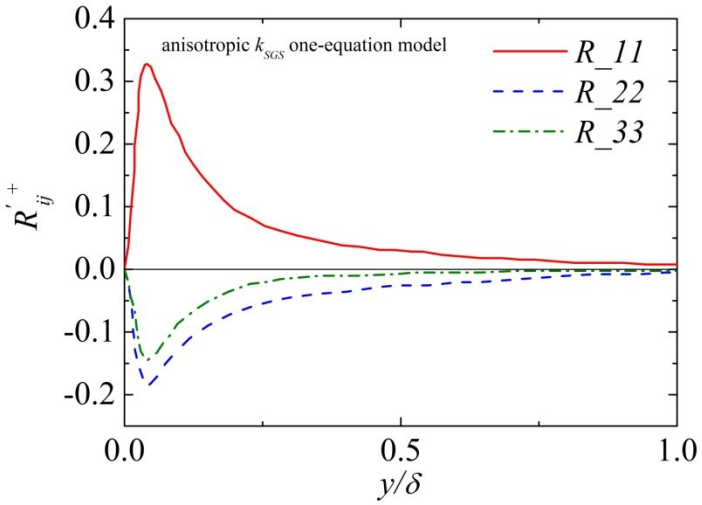

Figure 4.9: Anisotropic term R'_{ij} profile.

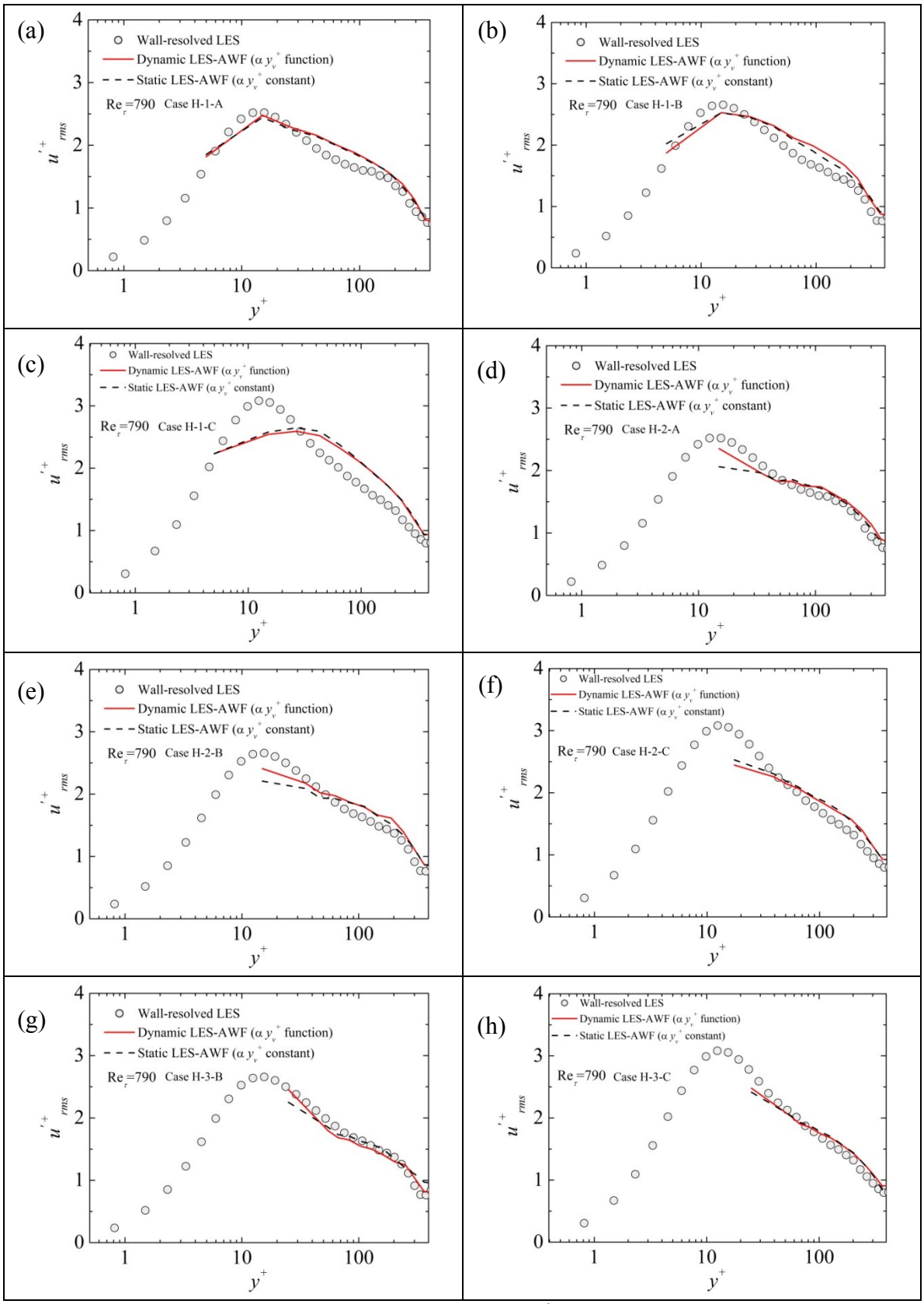

Figure 4.10: Reynolds stress $\sqrt{uu}'^+$ ($\mathrm{Re}_\tau = 790$)

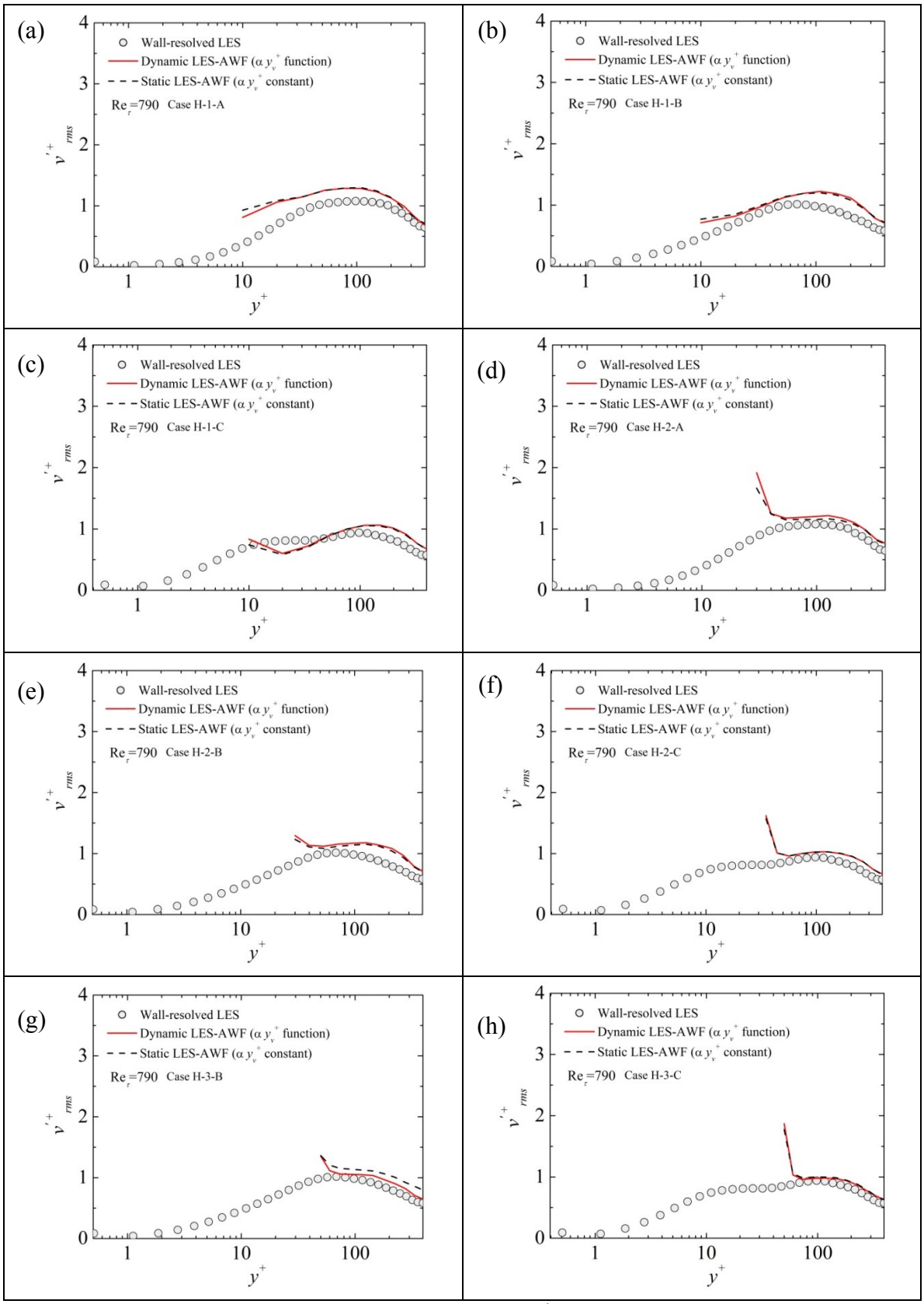

Figure 4.11: Reynolds stress $\sqrt{vv}'^+$ ($\mathrm{Re}_\tau = 790$)

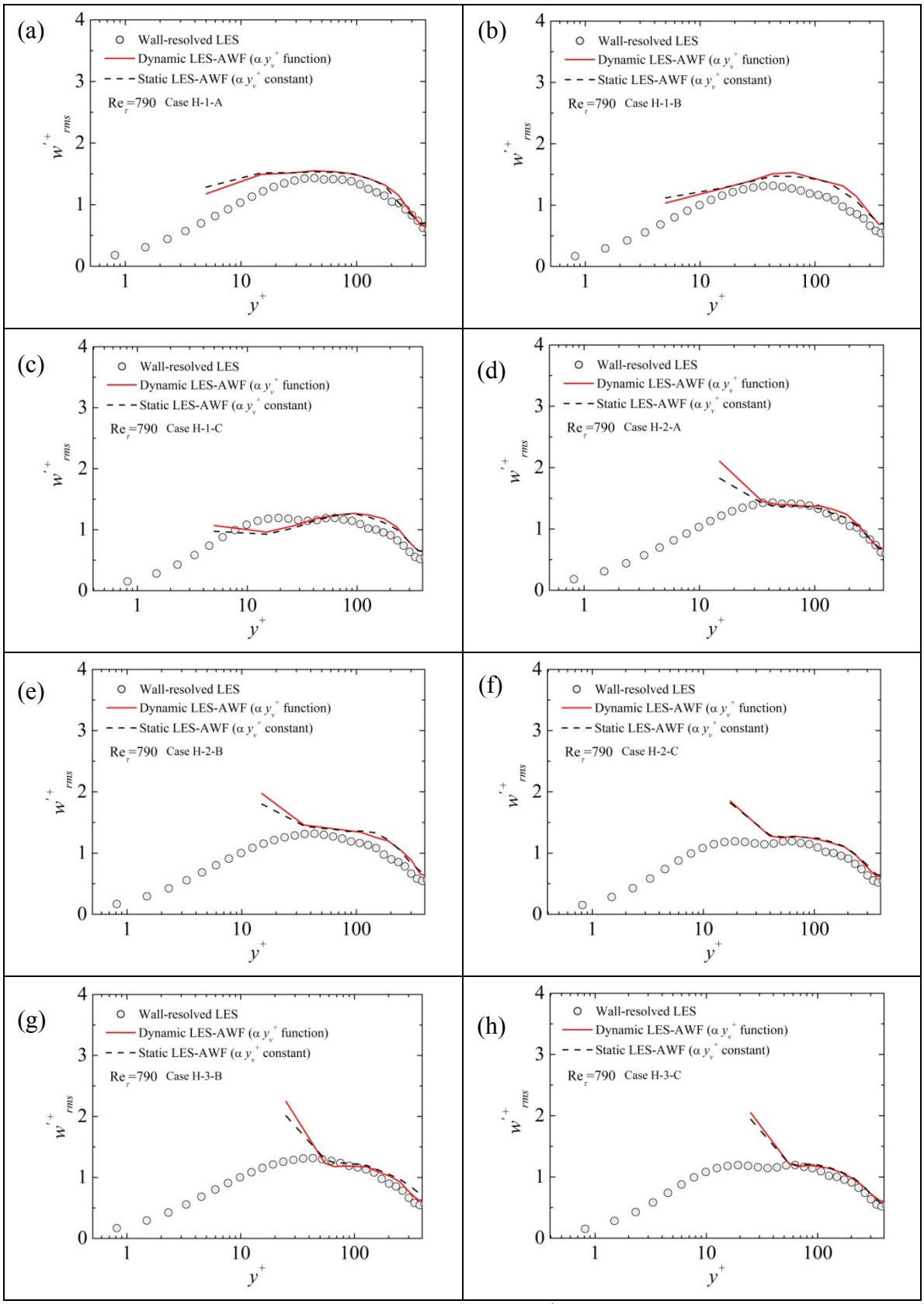

Figure 4.12: Reynolds stress $\sqrt{ww}'^+$ ($\mathrm{Re}_\tau = 790$)

4.1.3.2 **The case of $\mathbf{Re_\tau = 360}$:**

The profile in the wall normal direction of the Reynolds normal stress components $\sqrt{\overline{uu}}^{\prime+}$, $\sqrt{\overline{vv}}^{\prime+}$ and $\sqrt{\overline{ww}}^{\prime+}$ are described in Figs. 4.8, 4.9 and 4.10. These components and the wall distance are normalized by the friction velocity in the same way as the higher Reynolds number case.

As shown in Fig. 4.13, the performance of and constant Static LES-AWF becomes better in some cases such as (a) L1A, (d) L2A, (b) L1B and (g) L3B, although in some cases the accuracy is not sufficient. Particularly, the prediction at the first grid point shows better correspondence with the Wall-resolved LES results. It can be assumed that this is given by the effect of new modeling of the α and y_v^+ functions because the velocity gradient at the first grid point, which has a strong effect on the Reynolds stresses, is provided by the AWF. Furthermore, in most cases, the LES-AWF agrees well with the Wall-resolved LES results in core region.

The comparison of the Reynolds stress components between $\sqrt{\overline{vv}}^{\prime+}$ and $\sqrt{\overline{ww}}^{\prime+}$ the LES-AWF and the Wall-resolved LES case is described in Fig. 4.14 and 4.15. There are good agreements particularly in core region, although the results at the first grid point is predicted excessively. This can be caused by the lack of anisotropy of SGS turbulence model as mentioned in the previous section.

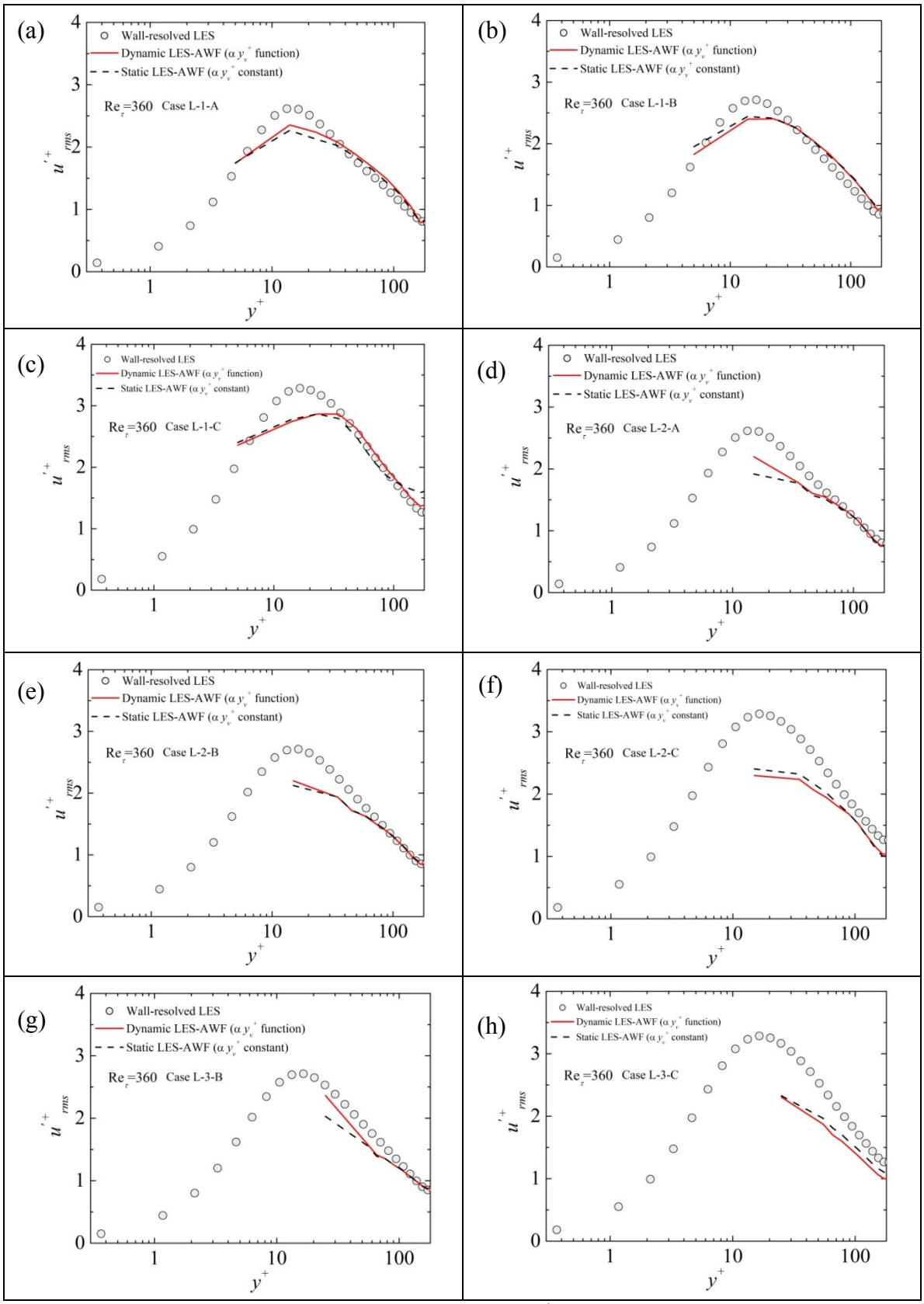

Figure 4.13: Reynolds stress $\sqrt{uu}^{'+}$ ($\mathrm{Re}_\tau = 360$)

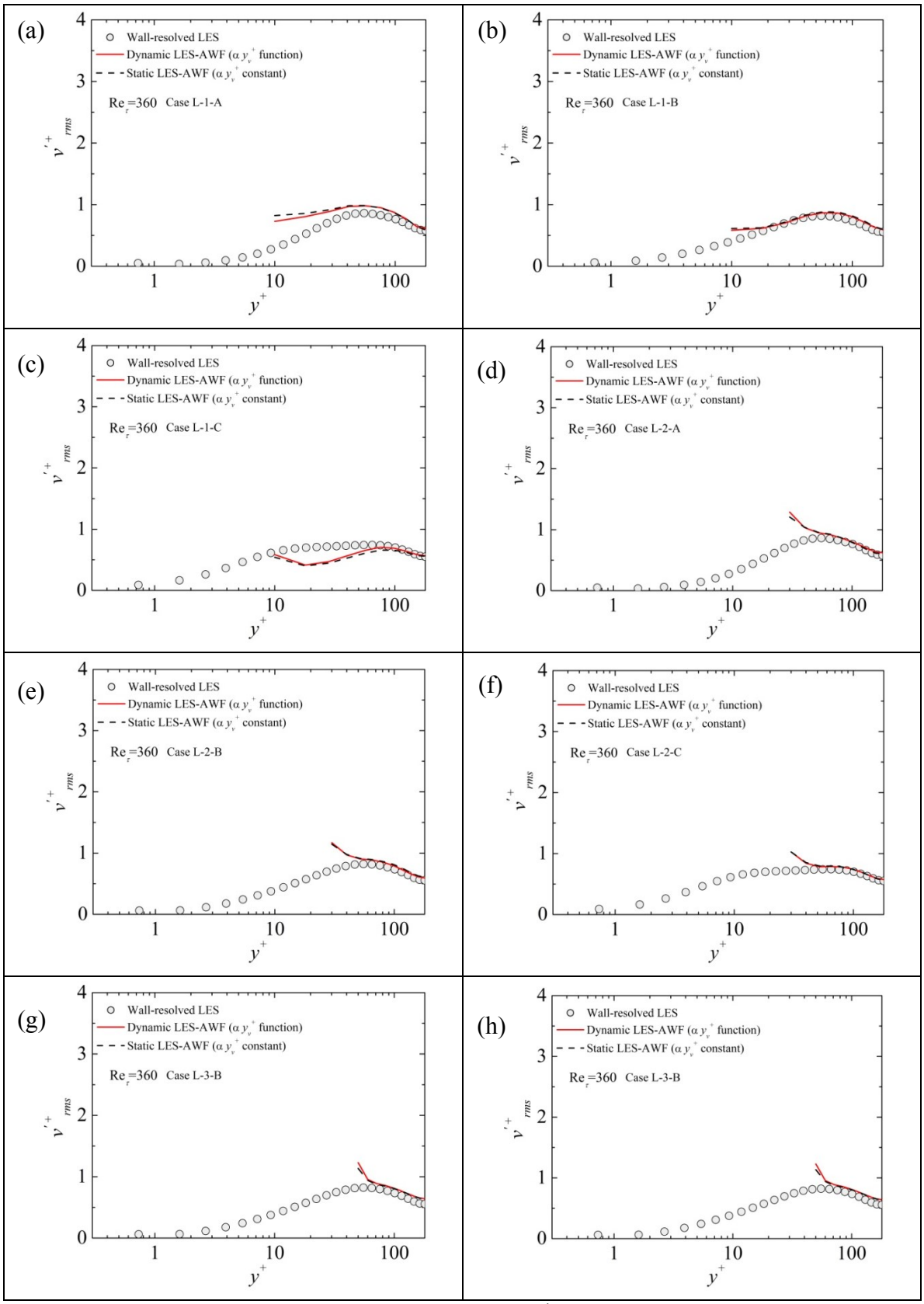

Figure 4.14: Reynolds stress $\sqrt{vv}^{'+}$ ($\mathrm{Re}_\tau = 360$)

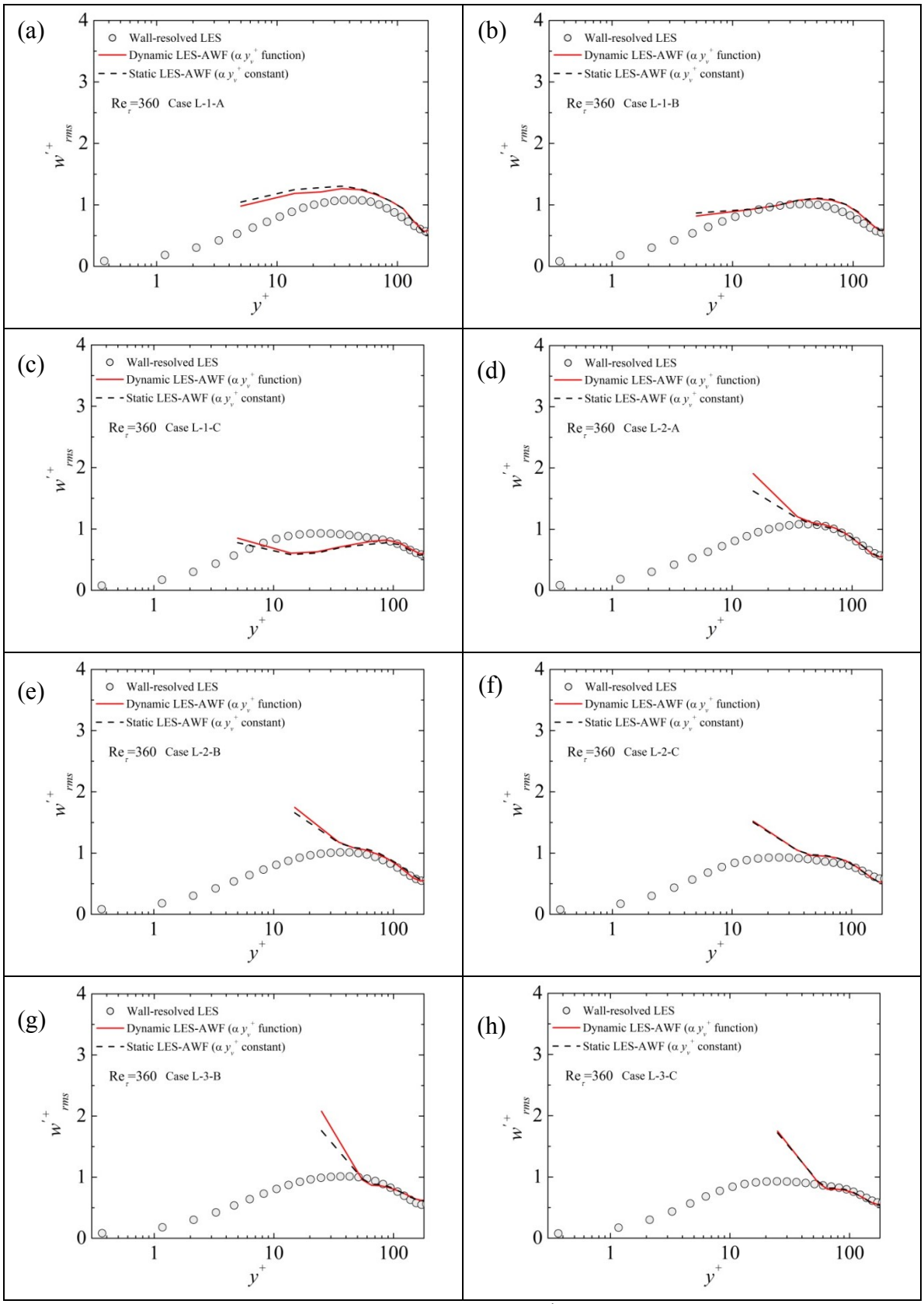

Figure 4.15: Reynolds stress $\sqrt{\overline{ww}}'^+$ ($\mathrm{Re}_\tau = 360$)

4.1.4 **Reynolds shear stresses:**

4.1.4.1 **The case of $Re_\tau = 790$:**

Fig. 4.16 illustrates the Reynolds shear stress uv'^{+} profiles. The wall distance and the Reynolds shear stress are normalized by friction velocity u_τ. Basically, there are not any large differences between the Dynamic and the Static LES-AWFs. However, the case (d) H2A and (g) H3B showed improvements to some extent, although in most cases both the LES-AWF models overestimate the Reynolds shear stress. In the case of H3B, the Dynamic LES-AWF corresponds better with the Wall-resolved LES results in core region. On the other hand, in the case of (d) H2A, the Reynolds shear stress prediction at the first grid point becomes more precise by the Dynamic LES-AWF.

Whereas the cases of (a) H1A and (d) H2A show relatively good agreements, the cases with (c) H1C, (e) H2C and (h) H3C show highly overestimated Reynolds shear stress. From this point of view, it can be said that the Reynolds shear stress prediction by the LES-AWF tends to be less accurate with coarser mesh. It is revealed that, especially, the coarser mesh than that of case (d) H2C is hard to predict the Reynolds shear stress at the first grid point precisely.

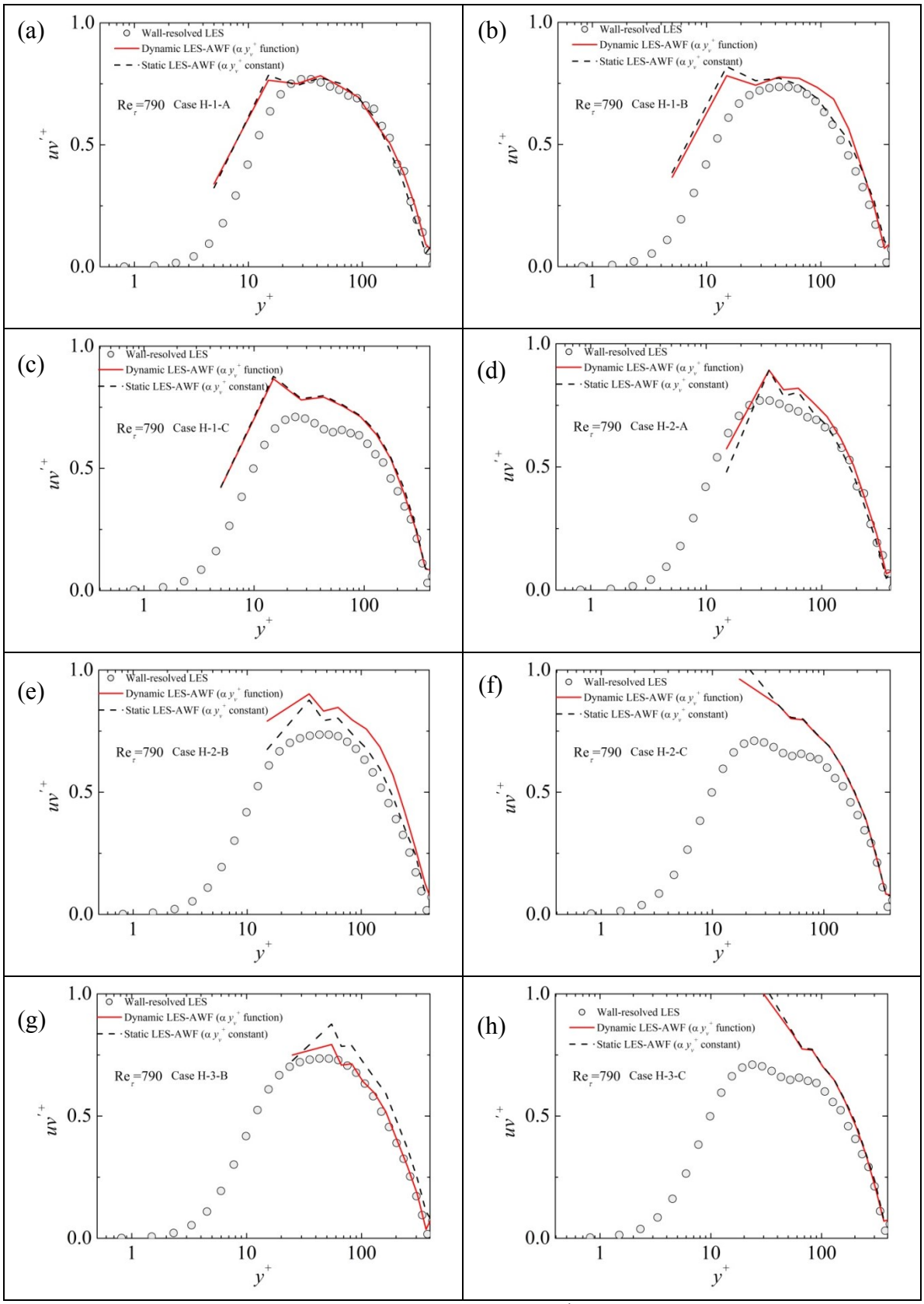

Figure 4.16: Reynolds shear stress uv'^{+} ($\mathrm{Re}_{\tau} = 790$)

4.1.4.1 **The case of $Re_\tau = 360$:**

Fig. 4.17 describes Reynolds shear stress uv'^{+} profile in the wall normal direction. The Reynolds shear stress uv'^{+} and the wall distance y are normalized by friction velosity u_τ. The case of (h) L3C illustrates good correspondence with the Wall-resolved LES results. Since the coarsest mesh is applied to this case, this improvement is encouraging. The Dynamic modeling performs well with a coarse mesh and provides more accurate results.

In addition, better agreements at the first grid point can be seen in cases of (d) L2Aand (f) L2C. This can be contributed to the modification of SGS eddy viscosity modeling for LES-AWF.

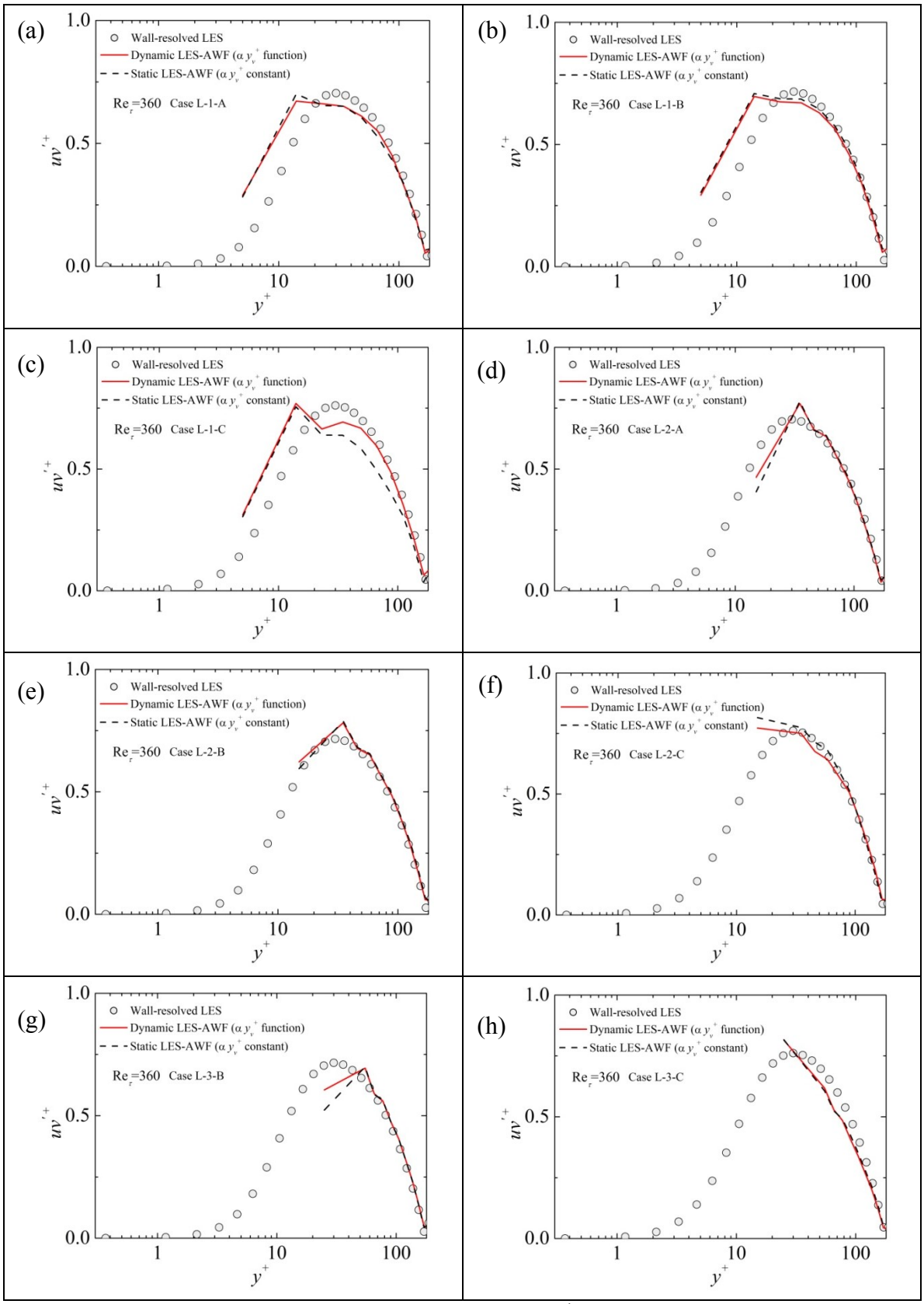

Figure 4.17: Reynolds shear stress uv'^{+} ($\mathrm{Re}_\tau = 360$)

4.2 **Rectangular duct flow:**

4.2.1 **Computational geometry:**

Rectangular duct flow is also employed as a simple geometry for validating the Dynamic LES-AWF's performance. The computational geometry and coordinate system is described in Fig. 4.18. This study utilizes non-uniform structured mesh in height and span wise direction, while uniform structure mesh in flow direction. As shown in Fig. 4.18, computational domain size is $3H(x) \times H(y) \times H(z)$, where H is height and width of the rectangular duct. The friction Reynolds number Re_τ is set to 790. This friction Reynolds number is defined by duct height H and mean friction velocity u_τ. No-slip boundary condition is applied to every wall and periodic boundary condition is employed in flow direction. In this study, in order to validate the LES-AWF' performance, three different simulation results are compared. They are wall-resolved LES, which arranges enough dense mesh in near wall region without using any wall functions, the Static LES-AWF and the Dynamic LES-AWF. Wall-resolved LES sets the first layer thickness to less than 1 ($y_1^+ < 1$), while LES-AWF set it to 30 ($y_1^+ = 30$). This is because this first layer thickness showed remarkable improvement of the Dynamic LES-AWF in the three-dimensional flow case motioned in the previous section. Hence, in order to define the same grid size as the L2C case for the three-dimensional flow case (see Table 4.4), the grid size in x direction is determined as 40.

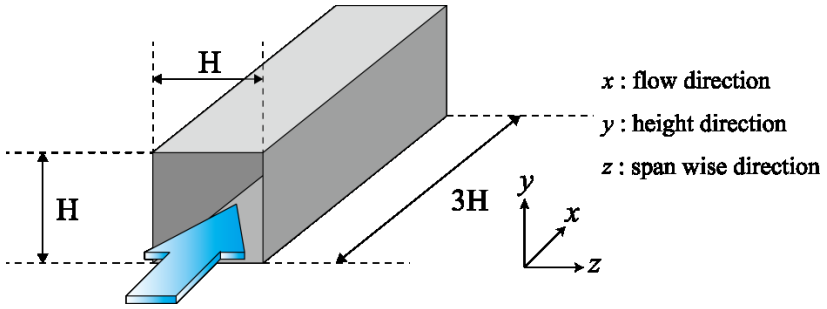

Figure 4.18: rectangular duct

Table 4.4: Grid resolution for rectangular duct flow.

Re_τ	Case	Δx^+	y_1^+	z_1^+	$N_x \times N_y \times N_z$
790	Wall-resolved LES	40	0.5	0.5	$60 \times 60 \times 60$
	Dynamic LES-AWF	40	30	30	$60 \times 40 \times 40$
	Static LES-AWF				

Table 4.5: Grid resolution for grid dependency test.

Case	Re_τ	$N_x \times N_y \times N_z$
grid 1	790	$60 \times 90 \times 90$
grid 2		$60 \times 60 \times 60$

Table:4.6: Grid resolution for model validation

Case	Re_τ	$N_x \times N_y \times N_z$
DNS [43]	600	$100 \times 100 \times 96$
LES present		$60 \times 60 \times 60$

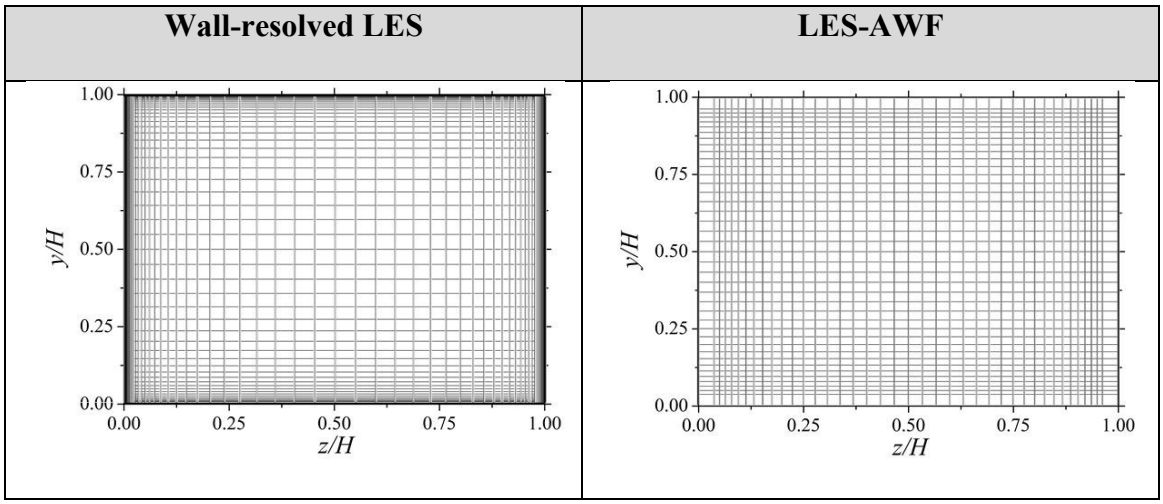

Figure 4.19: Computational grid for the rectangular duct.

Model validation is performed so that the turbulence model adopted for this simulation (Smagorinsky model) can be validated. The grid resolution and friction Reynolds number is shown in Table 4.6. Huser [43] et al. performed DNS in straight square duct and their result is compared the result of the present LES. Fig. 4.20 illustrates the mean velocity profile at the wall normal bisector. As can be seen in Fig. 4.20, there is low difference between two different simulations. Hence, it is revealed that the turbulence model for this simulation is able to perform accurately for this rectangular duct.

In addition, the grid dependency test is also conducted in order to clarify the required grid resolution for this geometry. The grid 2 is 1.5 times denser in y and z direction than the grid 1. The mean velocity comparison between these two different meshes is shown in Fig. 4.21.

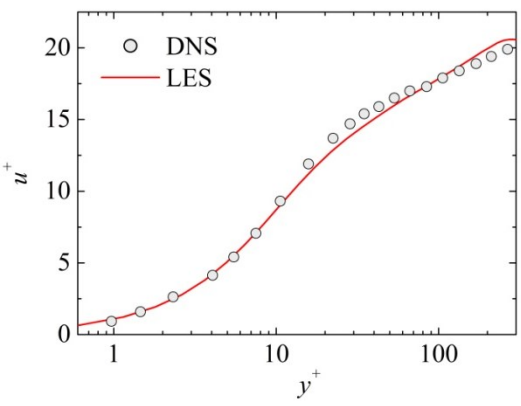

Figure 4.20: Model Validation.

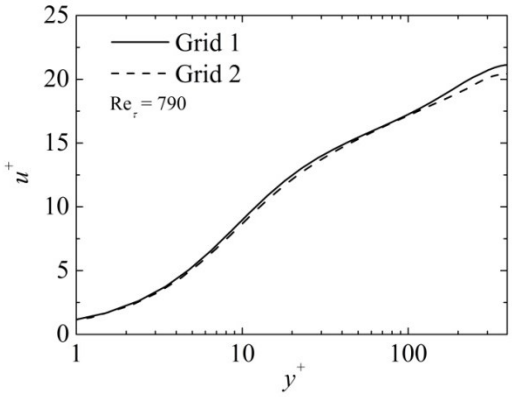

Figure 4.21: Grid dependency test.

4.2.2 **The definition of the vertical lines:**

This study employed five vertical lines for plotting data. Fig. 4.22 shows these lines. Since, the geometry is symmetric in y and z direction, the left bottom quarter section of the vertical cross section is only used for the comparison of results. In Fig. 4.21, δ denotes half duct height or width. The normalized distances from the side wall and these five lines are 0.1, 0.3, 0.5, 0.8 and 1.0, respectively. The normalized wall distance is defined as z/δ.

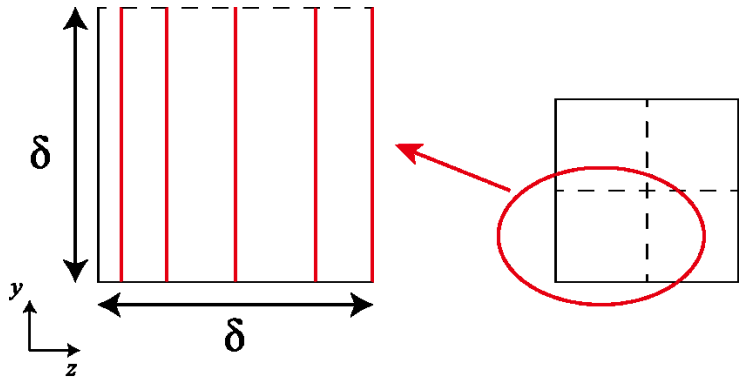

Figure 4.22: Five vertical lines on cross section.

4.2.3 **Mean velocity profile:**

Fig. 4.23 illustrates mean velocity profile on the fine vertical lines defined in Fig. 4.22. The mean velocity u is normalized the maximum mean velocity u_0 and the distance from the bottom wall y is normalized by half duct height δ. As seen in Fig. 4.23, both of the Dynamic and the Static LES-AWF agree well with the wall resolved LES result, although the mesh employed for LES-AWF is coarser than wall resolved LES. Hence, LES-AWF can also perform well in around corner of the rectangular duct where there are large effects from the side and bottom wall. However, there is not a large difference between the Dynamic and the Static LES-AWF in this geometry.

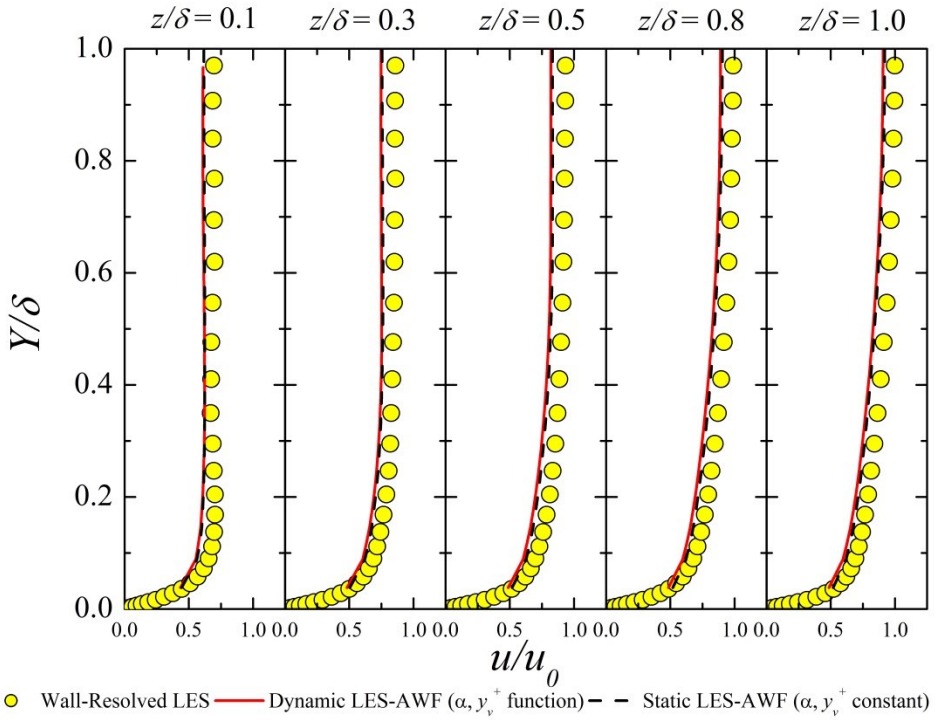

Figure 4.23: Mean velocity profile u in the rectangular duct.

4.2.4 **Secondary flow:**

Fig. 4.24 describes the secondary flow v and w profiles in the rectangular duct. The velocity v and w and wall distance y are normalized in the same way. The velocity v and w profile employed the same five vertical lines.

Basically, Fig. 4.24 does not show a large difference between two LES-AWFs, but in the corner of the line $z/\delta = 0.1$, the Dynamic LES-AWF's result is slightly closer to the wall-resolved LES result. Since this region is quite close (y^+ or z^+ are almost equal to 80) to the side wall and bottom wall, the velocity profile has a large wall effect and this region is hard to predict velocity profile precisely. However, this result reveals that the new modeling of SGS eddy viscosity for LES-AWF contributes to this improvement.

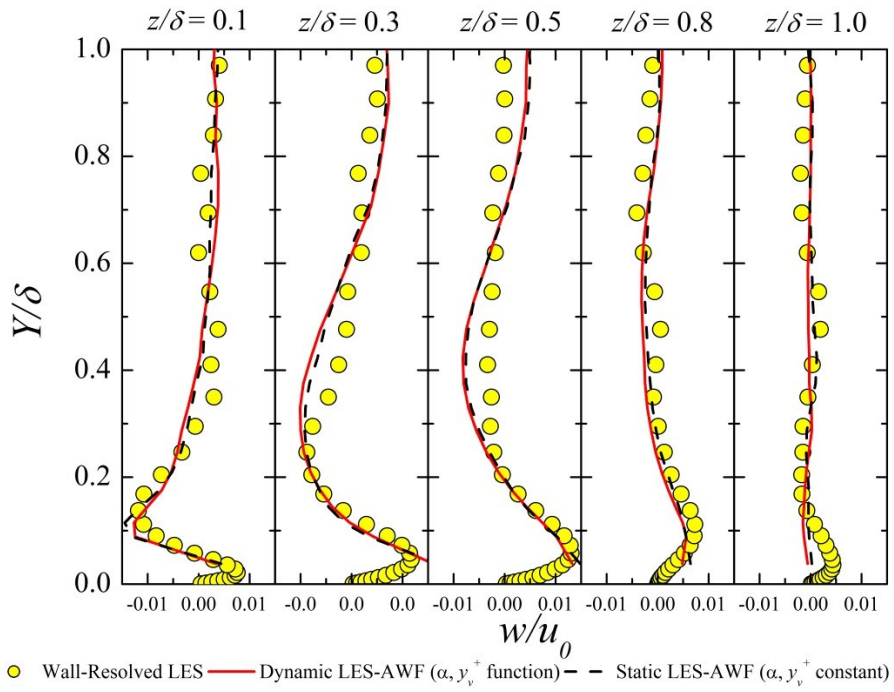

Figure 4.24: Secondary flow w profile in the rectangular duct.

There is not a large difference between two different LES-AWFs in Fig. 4.25 either. However, in the core region of the line $z/\delta = 0.1$, Dynamic LES-AWF showed slightly better correspondence with wall-resolved LES result. This line is the closest line to the side wall of these five lines, this improvement can be considered to be the contribution of the Dynamic LES-AWF. On the other hand, in the corner of the line $z/\delta = 0.1$, there is a discrepancy between wall-resolved LES and LES-AWFs. This is caused by the assumption of AWF that $v \sim 0$ in near wall region. Hence, AWF does not include the wall normal component of the convection term. Since the line $z/\delta = 0.1$ is close to the bottom wall as well as the side wall, this line tends to have relatively large wall effects from both of the bottom and side wall.

However, LES-AWFs agree well with wall-resolved LES in core region at each vertical line. This fact is quite meaningful because LES-AWF provides sufficiently accurate velocity profile in core region, although the number of grid points is 60 % fewer than that of wall-resolved LES.

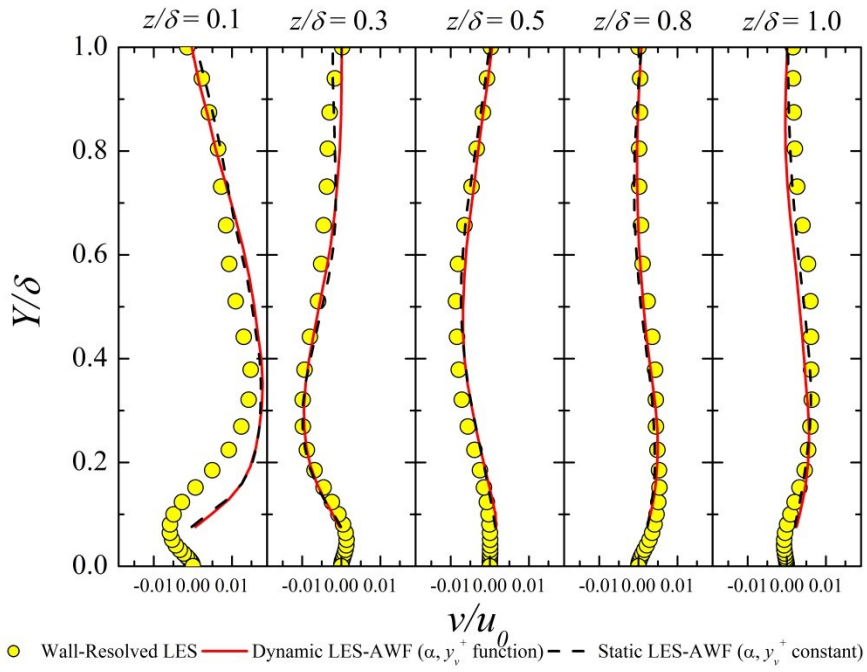

Figure 4.25: Secondary flow v profile in the rectangular duct.

4.2.4 **Reynolds stress:**

Figs. 4.26, 4.27 and 4.28 describe the Reynolds stress profile at the five vertical lines. Reynolds stress uu', vv' and ww' and wall distance from the bottom wall are normalized by maximum mean velocity u_0 and half duct width δ, respectively.

LES-AWFs show a good agreement with the wall resolved LES-AWF for Reynolds stress uu', although there are no significant differences between the Static LES-AWF and the Dynamic LES-AWF.

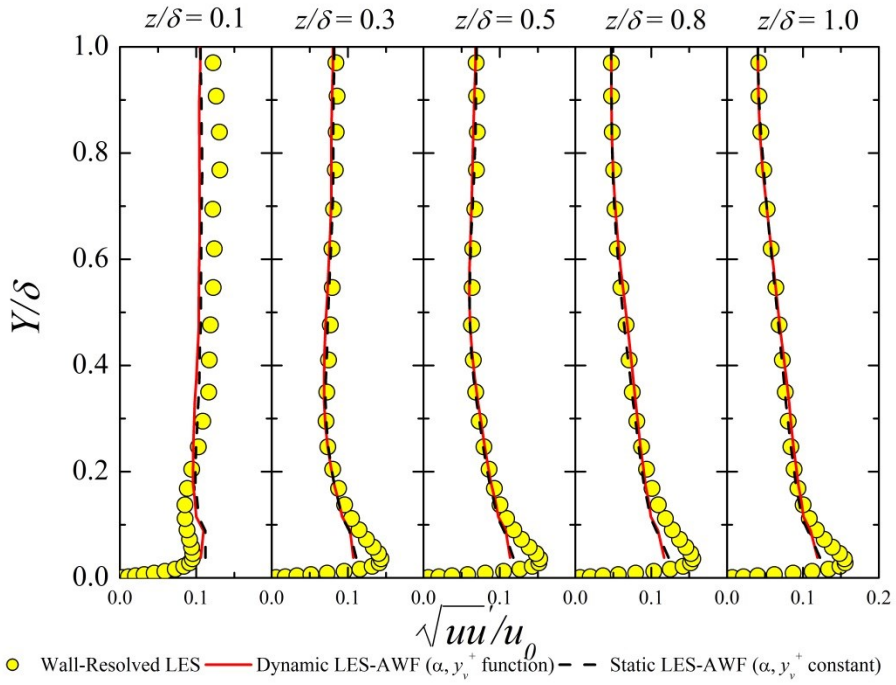

Figure 4.26: Reynolds stress uu' in the rectangular duct.

There are inconsistencies at first grid point between LES-AWFs and wall-resolved LES for Reynolds stress vv' and ww'. This is caused by the over prediction of SGS Reynolds stress. As mentioned in section 4.1.3, this over prediction can be considered to be the effect of the lack of anisotropy. Since Smagorinsky model employed in this study is an isotropic SGS eddy viscosity model, this model cannot express anisotropy of SGS Reynolds stress components by reducing a certain amount of the SGS Reynolds stress components vv'_{SGS} and ww'_{SGS} and add that amount to the other component uu'_{SGS}. Therefore, vv'_{SGS} and ww'_{SGS} is overestimated in near wall region and contrary to this, uu'_{SGS} is overestimated.

However, LES-AWFs showed good correspondence to wall-resolved LES in core region.

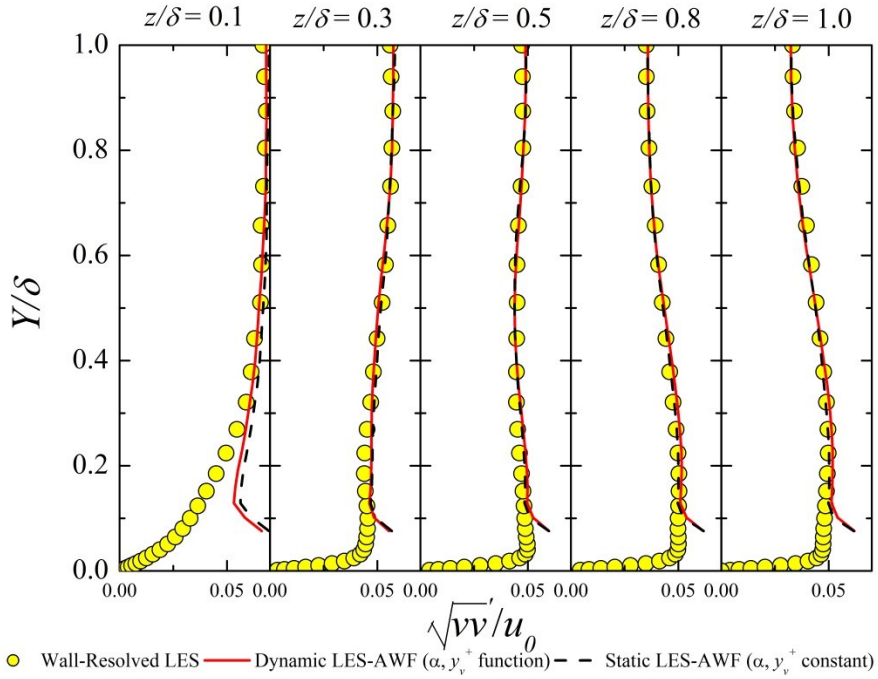

Figure 4.27: Reynolds stress vv' in the rectangular duct.

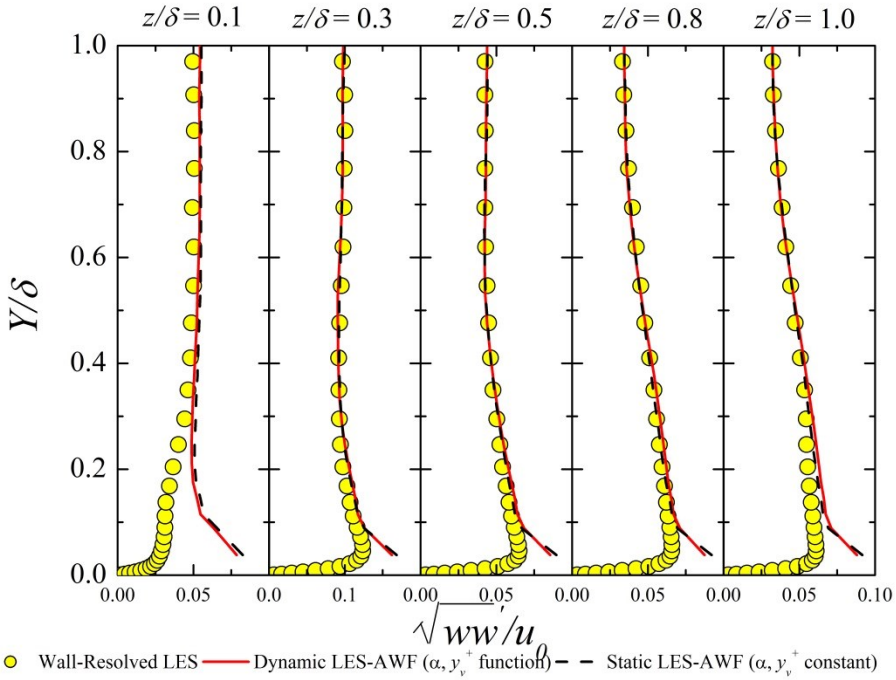

Figure 4.28: Reynolds stress ww' in the rectangular duct.

4.2.5 **Reynolds shear stress:**

Fig. 4.29 illustrates Reynolds shear stress uv' profile at five vertical lines $z/\delta = 0.1$ to 1.0. uv' is normalized by mean friction velocity $u_{\tau\, mean}$ and wall distance from the bottom wall is normalized by half duct width δ.

There is a good correspondence between LES-AWFs and wall-resolved LES as a whole, although the line $z/\delta = 0.1$ includes a discrepancy caused by the side wall effect as well as bottom wall effect. Especially, the lines $z/\delta = 0.3$ and 0.8 describes the good agreement.

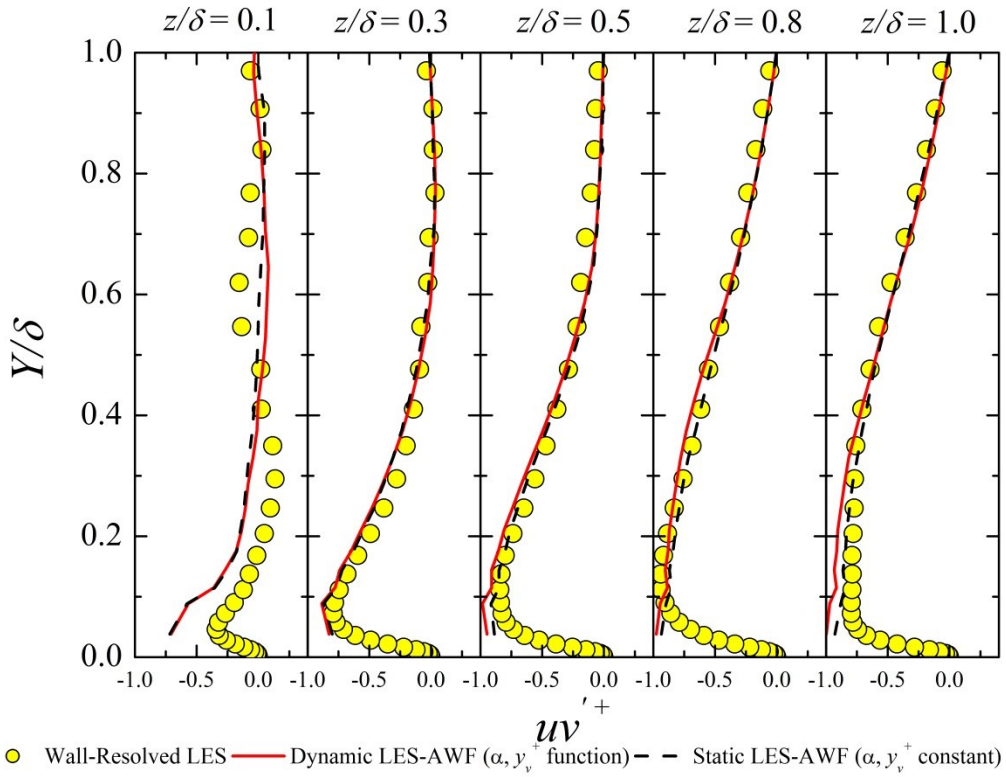

Figure 4.29: Reynolds shear stress uv' in the rectangular duct.

4.2.6 **Summary (rectangular duct):**

The Dynamic LES-AWF performance is examined in the rectangular duct. Basically, there are not significant difference between the Static LES-AWF and the Dynamic LES-AWF. However, the Dynamic LES-AWF slightly improved the accuracy about secondary flow v prediction near side wall region and w prediction near corner region. In addition, it also enhanced the performance of Reynolds stress component vv' to some extent near corner region.

CHAPTER 5: CONCLUSION

I. AWF can employ three times coarser mesh than a Wall-resolved LES in the wall normal direction of a three-dimensional channel flow.

II. Investigating the strain rate tensor profile in the near wall region, the modeling of SGS eddy viscosity can be expressed as a grid dependent and dynamic function. Hence the two parameters α and y_v^+ for the modeling ν_{SGS} can adjust to the optimal values depending on different grid sizes and velocity fields.

III. The Dynamic LES-AWF predicts the mean velocity profile more precisely than the Static LES-AWF especially when the first grid point is set far from the wall approximately by 5 %.

IV. Finer mesh in near wall region enhances the accuracy of the Dynamic LES-AWF.

V. Computations using the Dynamic LES-AWF showed slightly better agreement for the secondary flow around comer region in rectangular duct because the new modeling of α and y_v^+ adjusted to the optimal values by the grid dependent and dynamic functions for these two parameters.

VI. The Dynamic LES-AWF also contributes in improving the prediction of the Reynolds stresses. Particularly, the component of the Reynolds normal stresses in a stream wise direction is improved remarkably. However, other components of the Reynolds normal stresses still need more study to be improved.

VII. It is observed that the new ν_{SGS} modeling can adjust to optimal values and improve the prediction of the mean velocity and Reynolds normal stresses in a stream wise direction.

REFERENCES

[1]: Craft, T.J., Suga, K., Iacovides, H., 2005, A Generalized Analytical Wall-Function for Turbulence, Transactions of the Japan Society of Mechanical Engineers, 71, 711 B

[2]: Launder, B.E., Spalding, D.B., 1974, The numerical Computation of Turbulent Flows, Computer Methods in Applied Mechanics and Engineering 3, pp.269-289

[3]: Gharbi, N.El, Absi, R., Benzaoui, A., Amara, E.H., 2009, Effect of near-wall treatments on airflow simulations, Proceedings of 2009 International Conference on Computational Methods for Engineering and Environment. 185-189

[4]: Smith, B.L., 2009, Adaptation of the law of the wall boundary treatment to include volumetric heating effects, Applied Mathematical Modelling 33, 1306-1322

[5]: Benarafa, Y., Cioni, O., Ducros, F., Sagaut, P., 2006, RANS/LES coupling for unsteady turbulent flow simulation at high Reynolds number on coarse meshes, Computer methods in applied mechanics and engineering 195, 2939-2960

[6]: Suga, K., Craft, T.J., Iacovides, H., 2006, An analytical wall-function for turbulent flows and heat transfer over rough walls, International Journal of Heat and Fluid Flow, 27, 852-866

[7]: Suga, K., 2007, Computation of high Prandtl number turbulent thermal fields by the analytical wall-function, Internal Journal of Heat and Mass Transfer 50, 4967-4974

[8]: Suga, K., Nishiguchi, S., 2009, Computation of turbulent flows over porous/fluid interfaces, Fluid Dynamics Research 41

[9]: Suga, K., Kubo, M., 2010, Modelling turbulent high Schmidt number mass transfer across underformable gas-liquid interfaces, International Journal of Heat and Mass Transfer

[10]: Suga, K., Ishibashi, Y., Kuwata, Y., 2013, An analytical wall-function for recirculating and impinging turbulent transfer, International Journal of Heat and Fluid Flow, 41, 45-54

[11]: Suga, K., Tanaka, T., 1992, Wall Stress Model for LES by the MRT Lattice Boltzmann Method, Master Thesis, Osaka Prefecture University, Osaka, Japan

[12]: Amano, R., Arakawa, H., Suga, K., 2014, Turbulent heat transfer in a two-pass cooling channel by several wall turbulence models 77, 406-416

[13]: Gerasimov, A.V., 2003, Development and application of an analytical wall-function strategy for modelling forced, mixed and natural convection flows. Ph.D. Thesis, University of Manchester, Manchester, UK.

[14]: Breuer, M., Kniazev, B., Abel, M., 2007, Development of wall models for LES of separated flows using statistical evaluations, Computer and Fluids 36, 817-837

[15]: Werner, H., Wengle, H., 1993, Large-eddy simulation of turbulent flow over and around

a cube in a plate channel, Turbulent Shear Flows 8, 155-168

[16]: Kawai, S., Asada, K., 2013, Wall-modeled large-eddy simulation of high Reynolds number flow around an airfoil near stall condition, Computer and Fluids, 85, 105-113

[17]: Monfort, D., Benhamadouche, S., Sagaut, P., 2010, Meshless approach for wall treatment in Large-Eddy Simulation, Comput. Methods Appl. Mech. Engrg. 199, 881-889

[18]: Templeton, J.A., Moin, P., and Wang, M., 2006, Wall models for large-eddy simulation based on optimal control theory, Flow Physics and Computation Division Department of Mechanical Engineering, Stanford University

[19]: Cabot, W., Moin, P., 1999, Approximate Wall Boundary Condition in the Large-Eddy Simulation of High Reynolds Number Flow, Flow, Turbulence and Combustion 63, 269-291

[20]: Utyuzhnikov, S.V., 2005, Some new approaches to building and implementation of wall-functions for modeling of near-wall turbulent flows, Computers and Fluids 34, 771-784

[21]: Larsson, J., Kawai, S., 2010, Wall-modeling in large eddy simulation: length scales, grid resolution and accuracy, Center for Turbulent Research Annual Research Briefs, 39-46

[22]: Gungor, A.G., Menon, S., 2010, A new two-scale for large eddy simulation of wall-bounded flows, Progress in Aerospace Sciences 46, 28-45

[23]: Cabot, W., 1997, Wall models in large eddy simulation of separated flow, Center for Turbulent Research Annual Research Briefs, 97-106

[24]: Piomelli, U., Balas, W., 2002, Wall-Layer Models for Large-Eddy Simulation, Annu.Rev.Fluid Mech.34, 349-374

[25]: Wang, M., Moin, P., 2002, Dynamic wall modeling for large-eddy simulation of complex turbulent flows, Physics of Fluids 14, 7, 2043-2051

[26]: Kalitzin, G., Medic, G., 2008, Templeton, J.A. Wall modeling for LES of high Reynolds number channel flows: What turbulence information is retained?, Computers and Fluids 37, 809-815

[27]: Knopp, T., Zhang, X., Kessler, R., Lube, G., 2010, Enhancement of an industrial finite-volume code for large-eddy-type simulation of incompressible high Reynolds number flow using near-wall modeling, Computer Methods in Applied Mechanics and Engineering 199, 890-902

[28]: Wang, M., 1999, LES with wall models for trailing-edge aeroacoustics, Center for Turbulent Research Annual Research Briefs, 355-364

[29]: Deardorff, JW., 1970, A numerical study of three-dimensional turbulent channel flow at large Reynolds numbers, Journal of Fluid Mechanics 41,453-480

[30]: Shumann, U., 1975, Subgrid-scale model for finite difference simulation of turbulent

flows in plane channels and annuli, Journal of Computational Physics 18, 376-404

[31]: Piomelli, U., Moin, P., Ferziger, JH., Kim, J., 1989, New approximate boundary conditions for large-eddy simulations of wall-bounded flows, Physics of Fluids A1, 1061-1068

[32]: Balaras, E., Benocci, C., 1994, Subgrid-scale models in finite-difference simulations of complex wall bounded flows, AGARD CP 551, 2.1-2.5

[33]: Balaras, E., Benocci C., Piomelli, U., 1996, Two-layer approximate boundary conditions for large-eddy simulations, AIAA Journal 34,1111-1119

[34]: Suga, K., Kiriishi, T., 2011, Simulation of turbulent duct flows by the MRT-LBM-LES, Master Thesis, Osaka Prefecture University, Osaka, Japan

[35]: Nicoud, F., Ducros, F., 1999, Subgrid-Scale Stress Modelling Based on the Square of the Velocity Gradient Tensor, Flow, Turbulence and Combustion 62, 183-200

[36]: Kajishima, T.,2003, Numerical Simulation of Turbulence Flows, YOKENDO Ltd. (ISBN: 4-8425-9910-6)

[37]: Rhie C.M., Chow, W.L., A Numerical Study of the Turbulent Flow Past an Isolated Airfoil With Trailing Edge Separation, AIAA Journal 21, 1525-1532

[38]: Harlow, F.H., Welch, J.E., 1965, Numerical calculation of Time-Dependent Viscous Imcompressible Flow of Fluid with Free Surface, Physics of Fluids 8, 2182

[39]: Amsden, A.A., Harlow, F.H., 1970, A simplified MAC technique for incompressible fluid flow calculations, Journal of Computational Physics 6, 322-325

[40]: Smagorinsky, J., 1963, General circulation experiments with the primitive equations, Mon. Wealth. Rev., 91 ,3, 99-164

[41]: Lilly, D.K., 1967, The representation of small-scale turbulence in numerical simulation expriments, IBM Form No.320-1951, 195-210

[42]: Abe, K., 2013, An improved anisotropy-resolving subgrid-scale model with the aid of a scale-similarity modeling concept, Internal Journal of Heat and Fluid Flow 39, 42-52

[43]: Huser, A., Biringen, S., 1993, Direct numerical simulation of turbulent flow in a square duct, Cambridge University Press 257, 65-95